To the Graduate Council:

I am submitting a doctoral dissertation written by Thomas S. Helms entitled "Metamorphism of Early Proterozoic Schists of the Southern Black Hills, South Dakota." I have examined the final copy of this dissertation for form and content and recommend that it be accepted in partial fulfilment of the requirements for the Ph. D. degree, with a major in Geology.

Theodore C. Labotka, Major Professor

We have read this dissertation and recommend it acceptance:

Harry Y. McSween

Lawrence A. Taylor

Jeffrey D. Kovac

Accepted for the Council:

Vice Provost and Dean of The Graduate School

METAMORPHISM OF EARLY PROTEROZOIC SCHISTS OF THE SOUTHERN BLACK HILLS, SOUTH DAKOTA

A Dissertation

Presented for the Doctor of Philosophy

Degree

The University of Tennessee, Knoxville

Thomas Seaman Helms

August 1991

To my wife and amigo

Lucy

ACKNOWLEGEMENTS

I would like to thank the members of my committee, Dr. Harry Y. McSween, Dr. Lawrence A. Taylor, and Dr. Jeffrey D. Kovac for their helpful reviews and of this dissertation. Special thanks go to my major professor Dr. Theodore C. Labotka for suggesting the metamorphic terrain exposed in the Black Hills as a doctoral research topic. I would also like to thank Dr. Labotka for his many years of insightful discussions about the processes of metamorphism and for financial support along the way. Immeasurable thanks go to Lucy Tinsley Helms (wife and pal) for keeping the operation a float for the past few years and for generally tolerating the life a graduate student with me. Many thanks also go to my parents Ruth and Crampton Helms for helping me over the spiritual and financial "rough" spots these many years (and for ample Meyers and OJ in "Moetown").

ABSTRACT

The Late Archean to Early Proterozoic terrain exposed in the Black Hills of South Dakota, records a history of deformation, metamorphism, and igneous activity extending from ~2.5 to 1.7 Ga. Metamorphism began during crustal thickening; however, maximum temperatures were attained after crustal thickening during a regional low-pressure, high-temperature event coinciding with the emplacement of the Harney Peak granite at 1.7 Ga. Metamorphic grade increased over a distance of 10 to 15 km from garnet grade in the northern portion of the terrain, to sillimanite + K-feldspar grade in the southern portion. Isograds mapped in the terrain include the first appearance of staurolite + biotite, andalusite + biotite, sillimanite, sillimanite + biotite + garnet, and sillimanite + K-feldspar. In the extreme western exposure of the terrain, kyanite + biotite occurs instead of andalusite + biotite. Geobarometry indicates that metamorphic pressures were between 2.0 and 4.4 kbar. Geothermometry indicates that temperature increased from 469-500 °C in the garnet zone to 528-555 °C in the sillimanite zone on the northern flank of the Harney Peak granite. Higher temperatures are recorded along the southern flank of the granite in the sillimanite + biotite + garnet zone (585 °C) and in the sillimanite + K-feldspar zone (≤ 662 °C). The distributions of isograds, isotherms, and major fold axes indicate that the Harney Peak granite was at the locus of a regional thermal high and that doming during granite emplacement locally deformed preexisting isograds and fold axes.

Pressure-temperature paths based on compositionally zoned garnets from garnet-grade and staurolite-grade rocks indicate that prograde

metamorphism from 400 °C to 500 °C occurred under almost isobaric conditions (± 0.5 bars). PT paths based on compositionally zoned garnets also have a clockwise orientation. Because of volume diffusion and retrograde decomposition, prograde PT paths could not be determined from sillimanite and sillimanite + K-feldspar zone garnets; however, reaction textures in these rocks strongly suggest clockwise decompression and cooling paths. Homogenization of garnets at a temperature of ~565 °C indicates heating and cooling occurred at a minimum of ~4 x 10^7 years.

Low-pressure, high-temperature metamorphism in the Black Hills followed crustal thickening associated with continental collision and the suturing of the Archean aged Superior and Wyoming provinces. One- and two-dimensional numerical models were constructed to examine the thermal consequences of rapid homogeneous crustal thickening and slow uplift. The uplift rate (0.014 mm/year) was estimated from the amount of uplift determined from geobarometry (14 to 16 km) and the time interval between peak metamorphism at 1.7 Ga and the age of the Cambrian (~0.6 Ga) lithologies unconformably overlying the Proterozoic crystalline complex. This value requires that uplift was constant and continuous. At an uplift rate of 0.014 mm/year, low-pressure, high-temperature metamorphism occurs with a moderate mantle heat flux (33 mW/m^2) and a measured crustal radiogenic heat production rate of 3.3 $\mu W/m^3$. The mantle heat flux is consistent with present-day reduced heat flux measurements and the rate of radiogenic heat production is estimated from the concentration of U, Th, and K in major lithologic units from the Black Hills. Estimated PTt paths are consistent with nearly isobaric heating, clockwise decompression, and with a thermal perturbation that lasts on the order of 10^7 years.

TABLE OF CONTENTS

CHAPTER		PAGE
I.	INTRODUCTION	1
II.	PETROGENESIS OF EARLY PROTEROZOIC PELITIC SCHISTS OF THE SOUTHERN BLACK HILLS	4
	Introduction and Geologic Setting	5
	Analytical Techniques	10
	Microstructures and Textures	11
	Isograds and Metamorphic Zones	11
	Reaction Relations and the Facies Series	18
	Metamorphic Conditions	27
	Controls on Isograd Distribution	37
	Discussion and Conclusions	40
III.	PT-PATHS: EVIDENCE FROM ZONED GARNETS, MINERAL INCLUSIONS, AND REACTION TEXTURES	45
	Introduction	46
	Geologic Setting	47
	Analytical Methods	51
	Calculation of PT Paths	52
	Garnet Zoning	55
	The Compositional System and Mineral Components	58
	K_{Eq}-Equation Sets	61
	The Garnet and Staurolite + Chlorite + Biotite Zones	66

The Andalusite + Biotite Zone 75
Sillimanite and Sillimanite + Biotite + Garnet Zone 78
Discussion 80
Tectonic Significance 85
Conclusions 88

IV. THE THERMAL CONSEQUENCES OF HOMOGENEOUS CRUSTAL THICKENING AND SLOW UPLIFT: A MODEL FOR LOW-PRESSURE, HIGH-TEMPERATURE METAMORPHISM 90
Introduction 91
Crustal Thickening and Uplift in the Black Hills 99
Heat Sources and Heat Sinks 101
The Thermal Model 107
Crustal Thickening and Slow Uplift 110
Discussion and Conclusions 120

V. CONCLUSIONS 124

REFERENCES CITED 128

APPENDICES 143
A1. THE FINITE DIFFERENCE SOLUTION 144
A2. FORTRAN SOURCE CODE FOR A FINITE DIFFERENCE PROGRAM. 149
A3. ELECTRON MICROPROBE ANALYSES 166
A4. FLOPPY DISK CONTAINING MICROPROBE ANALYSES AND CATION NORMALIZATIONS (INSERT)

VITA 196

LIST OF TABLES

TABLE		PAGE
2.1.	Mineral assemblages occurring at sample locations in Figure 2.1.	8
2.2.	Mineral compositions used in mass-balance calculations . . .	24
2.3.	Least-squares mass-balance equations and residuals	25
2.4.	Mineral compositions used to estimate temperature, pressures, and a_{H_2O}	28
2.5.	Comparative results of geologic thermometry and barometry	29
2.6.	System of homogeneous differential equations necessary to describe the relationship between μ_{H_2O} and X_{Mg} in the assemblages biotite + staurolite + andalusite + muscovite + quartz and staurolite + chlorite + biotite + muscovite + quartz	39
3.1.	Abbreviations and compositions of mineral components . .	54
3.2.	Reaction sets for the garnet zone, staurolite zone, and andalusite zone assemblages	62
3.3.	Equilibrium constant equations used to solve for pressure and temperature at garnet-core compositions buffered by the garnet-zone assemblage	63
3.4.	Equilibrium constant equations used to solve for pressure and temperature at garnet-core compositions by the andalusite + biotite-zone assemblage	64
3.5.	T, P, and mineral compositions calculated at measured	

garnet rim and muscovite values, with the system of equations presented inTable 3.3 67

4.1. Heat production rates of selected lithologies from the Black Hills 103

4.2. Heats of reaction for some major low-grade dehydration reactions 105

A3.1. Garnet compositions 168

A3.2. Muscovite compositions 175

A3.3. Plagioclase compositions 179

A3.4. Staurolite compositions 183

A3.5 Chlorite compositions 186

A3.6 Biotite compositions 188

LIST OF FIGURES

FIGURE		PAGE
2.1.	Geologic map of the study area simplified from Dewitt and others (1986; 1989)	6
2.2.	Mineral compositions (mole fractions), projected from muscovite and quartz onto the AFM plane. Garnet and biotite compositions are plotted on the Fe-Mg-Mn plane	13
2.3.	Grossular component in garnet plotted relative to anorthite component in coexisting plagioclase	19
2.4.	Idealized AFM facies series based on projections in Figure 2.2	20
2.5.	Metamorphic temperatures and pressures plotted on a simplified geologic map of the study area	31
2.6.	P-T conditions based on garnet-biotite thermometry and garnet-plagioclase (GSAP) geobarometry	33
2.7.	$X^{Fe}_{Mineral}$-μ_{H_2O} diagram calculated from the set of Gibbs-Duham relationships between coexisting Fe-Mg silicates	41
3.1.	Geologic map of the Black Hills showing the distribution of isograds, isotherms and simplified geology (after Dewitt et al., 1988)	48
3.2.	Representative compositional zoning profiles of garnets from (A) the garnet zone, (B) the staurolite + biotite + chlorite zone, (C) and (D) from the andalusite + biotite	

zone, and (E) the sillimanite zone 56

3.3. A) Frequency distribution of moles ^{VI}[Fe + Mg] in biotite. B) Frequency distribution of moles (Fe + Mg) in chlorite. C) Frequency distribution of moles ^{VI}Al in muscovite 60

3.4. PT paths calculated for garnet-core compositions for samples A) 23, B) 12 , C) 24, and D) 20 69

3.5. PT paths calculated with using the program GIBBS (Spear and Menard, 1989), P-T polygons calculated with K_{Eq} equations are also plotted for comparison 73

3.6. Andalusite Zone PT paths 76

3.7. Isopleths of garnet and biotite compositions in the KFMASH assemblages garnet + biotite + sillimanite + muscovite + quartz and garnet + biotite + andalusite + muscovite + quartz 81

4.1. Map of the Harney Peak area including the distribution of isograds, isotherms and simplified geology (after Dewitt et al., 1988) 93

4.2. A) Representative PT path estimated from a reaction zoned garnet collected in the Thompson Draw synform (sample 24, Figure 1). B) Qualitative PT path based on reaction textures in sillimanite-grade schists (Helms and Labotka, 1991b) 96

4.3. Temperature to depth diagram showing the geotherm before crustal thickening, after instantaneous

homogeneous thickening, and 100 million years after thickening and no erosion 108

4.4. Decompression paths estimated for a section of crust initially at a depth of 14 km subsequent to homogeneous doubling of the crust initially 35 km thick 112

4.5. Decompression paths estimated for sections of crust initially at depths of 14, 19, and 24 km, after homogeneous doubling of a section of crust initially 35 km thick 114

4.6. Thermal profiles adjacent to a pluton 117

A1.1. A graphical comparison of the analytical solution of the two-dimensional time-dependent heat equation with the numerical approximation calculated with the program in Appendix A2 147

A1.2. Test for convergence using smaller grid sizes with the finite difference program presented in Appendix A2 148

CHAPTER I

INTRODUCTION

Late Archean and Early Proterozoic schists exposed in the Black Hills Uplift of South Dakota, were regionally metamorphosed at low-pressure, high-temperature conditions. Metamorphism was dominantly characterized by an andalusite-sillimanite facies type, however, kyanite is stable in the extreme western portion of the Precambrian terrain. Metamorphism culminated with the intrusion of the peraluminous, S-type Harney Peak granite at 1.71 Ga. Isograds and isotherms trend westward, whereas major fold axes trend north. Emplacement of the Harney Peak granite deformed both fold axes and isograds.

The tectonic and thermal processes that result in regional low-pressure, high-temperature metamorphism and associated crustal anatexis remain uncertain and controversial. Tectonothermal models proposed to explain regional low-pressure, high-temperature metamorphism include advection of heat by magma derived from the lower crust or mantle (e.g. Lux et al., 1986; Barton and Hanson, 1989), an increased temperature at the base of the crust resulting from lithospheric thinning in extensional tectonic regimes (e.g. Wickham and Oxburgh, 1988; Grambling, 1988; Thompson, 1989), or to an increased heat flux at the base of the crust or lithosphere (Bird, 1978; Labotka and Albee, 1988; Loovsfeld, 1988; Loovsfeld and Ethridge, 1990).

The purpose of this study is to place petrologic constraints on the development of the low-pressure, high-temperature metamorphic terrain exposed in the Black Hills. Chapter II characterizes and presents the sequence of prograde low-variance reactions and the positions of the reaction isograds. Chapter II also presents final temperatures and pressures of metamorphism recorded by mineralogic thermometers and barometers.

Determination of pressure-temperature-time (PTt) paths provides the essential clue necessary for the determination of the causes of regional low-pressure, high-temperature metamorphism. Although there has been great progress in the past decade in determining metamorphic PT paths (e.g. Tracy et al., 1976; Selverstone and Spear, 1983; Selverstone et al., 1984; Spear and Rumble, 1986; Chamberlain, 1986; St-Onge, 1987), the value of Δt along the PT path is commonly unknown. Chapter III presents metamorphic PT paths inferred from reaction zoned garnets, mineral inclusions, and reaction textures. The magnitude of time that amphibolite facies conditions were maintained was also approximated from garnets that are inferred to have been homogenized by volume diffusion.

Several tectonothermal models have been proposed to explain regional low-pressure, high-temperature metamorphism, however, no single model is entirely consistent with petrologic and geologic observations presented in chapters II and III. Chapter IV presents tectonic and thermal numerical models that include the effects of rapid homogeneous crustal thickening, uplift and erosion, partial melting of the crust with subsequent advection, and radiogenic self-heating. The model is consistent with near-isobaric heating and clockwise decompression and also maintains amphibolite-facies conditions for the same approximate amount of time inferred from homogenized garnets.

CHAPTER II

PETROGENESIS OF EARLY PROTEROZOIC PELITIC SCHISTS OF THE SOUTHERN BLACK HILLS

INTRODUCTION AND GEOLOGIC SETTING

Archean and Proterozoic rocks exposed in the Black Hills Uplift (Figure 2.1) comprise a supracrustal sequence that records ~800 Ma of sedimentation, igneous intrusion, deformation, and metamorphism. Igneous activity included intrusion of the Bear Mountain granite into a metasedimentary sequence at 2.5 Ga (Gosselin and others, 1988) and the intrusion of the S-type Harney Peak granite at 1.7 Ga (Riley, 1970; Walker and others, 1986). The contact between Archean rocks and the base of the Proterozoic sequence is unconformable (Redden and Norton, 1975). Proterozoic rocks consist of metagreywacke, with lesser amounts of pelitic schist, iron-formation, quartzite, and mafic schist, and subordinate amounts of calcic schists.

Proterozoic and Archean lithologies were initially folded into an east- to northeast-trending set of isoclinal folds (F_1) that were overturned to the northwest and subsequently refolded into northwest-trending folds (F_2) (Redden and Norton, 1975; Dewitt and others, 1986). The second phase of folding produced the Thompson Draw and Lowden Mountain synforms, and refolded the Union Hill antiform. The dominant foliation developed during the formation of northwest-trending folds (Redden and Norton, 1975; Dewitt and others, 1986). In the south-central portion of the field area, doming associated with the intrusion of the Harney Peak granite deformed the original interference pattern and caused a late foliation that parallels the granite contact (Redden, 1963; 1968).

Pelitic schists in the study area dominantly record a low-pressure,

Figure 2.1 Geologic map of the study area simplified from Dewitt and others (1986; 1989). Sample locations are numbered where detailed chemical analyses have been collected. Mineral assemblages at numbered locations are listed in Table 2.1.

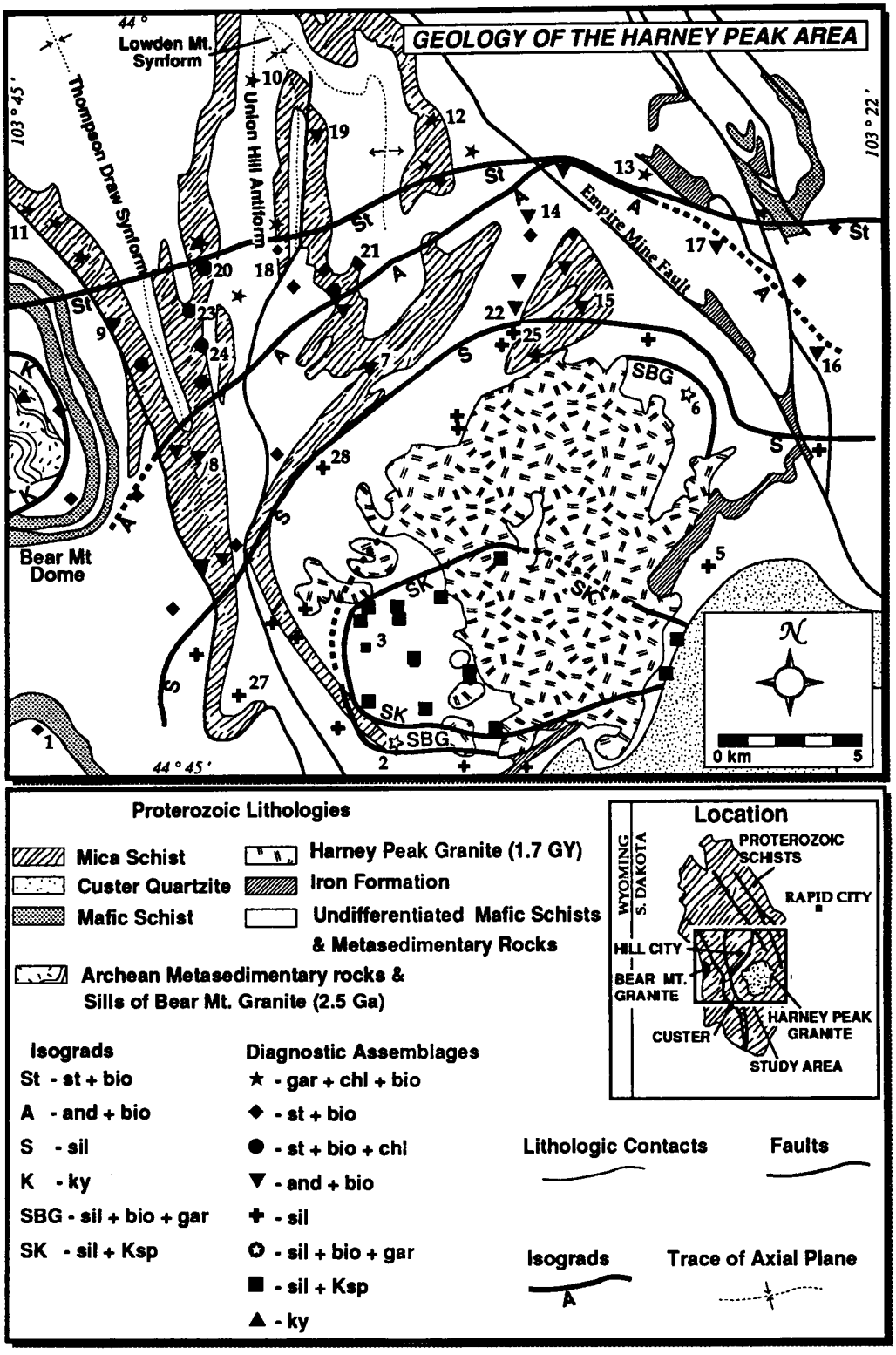

GEOLOGY OF THE HARNEY PEAK AREA
44°
103° 45'
103° 22'
44° 45'
Lowden Mt. Synform
Thompson Draw Synform
Union Hill Antiform
Empire Mine Fault
Bear Mt Dome
SBG
SK
St
A
S
K
0 km
5
Proterozoic Lithologies
Mica Schist
Custer Quartzite
Mafic Schist
Harney Peak Granite (1.7 GY)
Iron Formation
Undifferentiated Mafic Schists & Metasedimentary Rocks
Archean Metasedimentary rocks & Sills of Bear Mt. Granite (2.5 Ga)
Isograds
St - st + bio
A - and + bio
S - sil
K - ky
SBG - sil + bio + gar
SK - sil + Ksp
Diagnostic Assemblages
★ - gar + chl + bio
◆ - st + bio
● - st + bio + chl
▼ - and + bio
✚ - sil
✪ - sil + bio + gar
■ - sil + Ksp
▲ - ky
Lithologic Contacts
Faults
Isograds
Trace of Axial Plane
Location
WYOMING
S. DAKOTA
PROTEROZOIC SCHISTS
RAPID CITY
HILL CITY
BEAR MT. GRANITE
CUSTER
HARNEY PEAK GRANITE
STUDY AREA

Table 2.1. Mineral Assemblages occurring at sample locations in Figure 2.1

SAMPLE	ilm	gar	st	sil	ky	and	chl	cor	ksp	hem	mag
1	◆	◆	◆								
2	◆	◆	○	◆							
3		◆		◆					◆		
4				◆					◆		
5	◆	◆		◆							
6	◆	◆	○	◆		◆					
7	◆	◆	◆			◆	◆				
8		◆				◆	◆	◆		◆	
9	◆	◆	◆	◆		◆	◆			◆	◆
10	◆	◆					◆				
11	◆	◆					◆				
12	◆	◆					◆				
13	◆	◆					◆				
14	◆	◆				◆					
15	◆	◆				◆					
16	◆	◆	◆			◆					
17	◆	◆	◆			◆	◆				
18	◆	◆									
19	◆	◆				◆					
20	◆	◆	◆				◆				
21	◆	◆	◆				◆				
22a	◆	◆				◆					
22b	◆	◆	◆								
23	◆	◆	◆				◆				
24	◆	◆	◆				◆				
25a	◆	◆				◆					
25b	◆	◆		◆							
25c	◆	◆		◆		◆					
25d	◆	◆	◆	◆							
26	◆	◆									
27	◆	◆								◆	
28	◆	◆		◆							
29	◆	◆			◆						

Note: ◆ Mineral present; ○ Mineral present as inclusion only.Mineral abbreviations: ilm, ilmenite; gar, garnet; sil, sillimanite; st, staurolite; and, andalusite; cor cordierite; ksp, K-feldspar; hem, hematite; mag, magnetite; chl, chlorite.

high-temperature facies series (e.g. Redden, 1963;1968; Redden and Norton, 1975; Ratte and Wayland, 1969; and Ratte, 1986). North of the Harney Peak granite (Figure 2.1), prograde metamorphism of pelitic schists is characterized by the following sequence of zones: garnet , staurolite, andalusite + biotite, sillimanite, sillimanite + garnet + biotite. On the southern flank of the Harney Peak granite, sillimanite + K-feldspar-grade was reached. In the Thompson Draw synform, metamorphic grade increased southward from garnet-grade, to staurolite + biotite + chlorite grade, to Al_2SiO_5 + biotite grade. Andalusite is the dominant aluminum silicate; however, kyanite occurs in the Bear Mountain dome (Figure 2.1).

The Harney Peak granite (Figure 2.1) comprises thousands of coarse-grained to pegmatitic dikes and sills that dissect ubiquitous screens of metasedimentary rock (Redden and others, 1982). Utilizing data from Riley (1970), Walker and others (1986) recalculated a whole-rock Rb/Sr isochron age of 1.7 Ga for the granite. The Harney Peak granite appears to have been emplaced after F_2 folding and is largely unmetamorphosed. However, in the sillimanite + K-feldspar zone, several dikes and sills are deformed and metamorphosed, indicating that metamorphism and granite intrusion were partly synchronous. The amount of *in situ* partial melting that has occurred has not been determined; however, most of the granite appears to have intruded from depth (e.g. Duke and others, 1988).

The purpose of this chapter is to present the petrogenesis of pelitic schists exposed in the vicinity of the Harney Peak granite. Relative conditions of metamorphism are indicated by the sequence of metamorphic reactions in the AFM facies series. Temperature, pressure, and the fugacity of

water at the isograds, and throughout the terrain, are calculated with experimentally, thermodynamically, and empirically calibrated geothermometers and geobarometers. These data provide initial evidence for the thermal evolution of this regional low-pressure, high-temperature metamorphic terrain. The geometry of isograds, peak metamorphic temperatures, pressures, and fugacities of H_2O are used to determine the relationships among deformation, metamorphism, and the intrusion of the Harney Peak granite.

ANALYTICAL TECHNIQUES

Mineral analyses were collected on a Cameca SX50 electron microprobe using synthetic and natural standards and operating at an accelerating voltage of 15 kV. A beam current of 0.015 μA and beam diameter ~ 10 μm were used to analyze micas, feldspars, and cordierite. All other phases were analyzed with a beam current of 0.03 μA and a beam diameter of ~ 5 μm. All analyses were collected with a wavelength dispersive technique, utilizing ZAF corrections. Analytical precision on major elements (> 2 weight % oxide) is approximately ± 2.0 % relative, and precision on minor components is approximately ± 8.0 %.

Silicate minerals were normalized on the basis of the appropriate number of oxygens. Fe^{3+} was calculated for stoichiometric phases (i.e. no site-vacancies) if weight % totals were consistently low and cation totals were consistently high; ilmenite and hematite were the only phases that fit this criterion. Because biotite and muscovite have vacancies, Fe was assumed to be all Fe^{2+}.

MICROSTRUCTURES AND TEXTURES

Lithologic layering is the dominant planar fabric in the garnet and low-grade parts of the staurolite + biotite and andalusite + biotite zones. Chlorite and biotite are randomly oriented, and porphyroblasts of staurolite, andalusite, and garnet cut across lithologic layering. In fold noses, coarser-grained crystals of chlorite and biotite form a weak planar fabric oriented at an angle to layering. In higher-grade portions of the staurolite-biotite and andalusite-biotite zones and in the sillimanite zones, a well defined biotite-muscovite foliation developed. In the Thompson Draw synform and Union Hill antiform, staurolite, garnet, andalusite, and cordierite porphyroblasts postdate the axial planar foliation associated with F_2 folding. Quartz inclusion trails in crystals of andalusite, staurolite, and cordierite commonly preserve F_3 crenulations; however, in Mg-rich rocks andalusite porphyroblasts may be elongate parallel to lineations formed by the intersection of the axial planes of the crenulation and the earlier F_2 foliation. At distances of ~ 2-3 km from the Harney Peak granite, a late foliation resulted from regional doming associated with granite intrusion. Porphyroblasts in schists adjacent to the granite commonly grew with their long and intermediate axes in the plane of the late foliation.

ISOGRADS AND METAMORPHIC ZONES

Based on previous work (Redden, 1963; 1968; Redden and Norton, 1975; Ratte and Wayland, 1969; and Ratte, 1986) and petrologic data collected in this study, six isograds were mapped (Figure 2.1). These isograds include the first appearances of staurolite + biotite, andalusite + biotite, sillimanite,

sillimanite + biotite + (Fe,Mg)-garnet, and sillimanite + K-feldspar. The reaction governing the first appearance of cordierite + andalusite + biotite is noted, but, because the distribution of cordierite + andalusite is restricted, an isograd was not mapped.

Using the method of Thompson (1957), rim compositions of ferromagnesium silicates are projected on to the Al_2O_3-FeO-MgO (AFM) plane through the composition of end-member muscovite and quartz in Figure 2.2a-f. Garnet and biotite are also plotted on the FeO-MnO-MgO (FMM) plane adjacent to each AFM projection in Figure 2.2. Distribution of Fe and Mg between coexisting silicates follows the normal pattern of Fe-enrichment where garnet > staurolite > biotite ≥ chlorite > cordierite (e.g. Albee, 1965; Thompson, 1976; Labotka, 1981). A complete listing of compositional data is presented in Appendix A3.

Garnet-zone pelitic schists north of the staurolite isograd (Figure 2.1), contain the assemblage

garnet + chlorite + biotite + muscovite + plagioclase (An_{1-3}) +

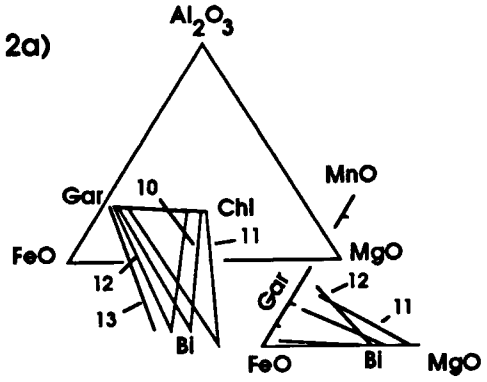
plagioclase (An_{20-23})+ quartz + ilmenite.

(Figure 2.2a). Subsets of the above assemblage lacking garnet and/or chlorite are common. Chlorite is not shown on the FMM plane; however, it has approximately the same Fe/Mg ratio as biotite and contains small amounts of MnO (<0.30 weight %). Garnets rims in this zone contain 2 to 27 mole % spessartine component. The presence of spessartine component in garnet allows the assemblage garnet + biotite + chlorite to coexist over a range of Fe/Mg ratios. Lower Fe/Mg ratios in coexisting garnet + chlorite + biotite are correlated with higher spessartine component in garnet.

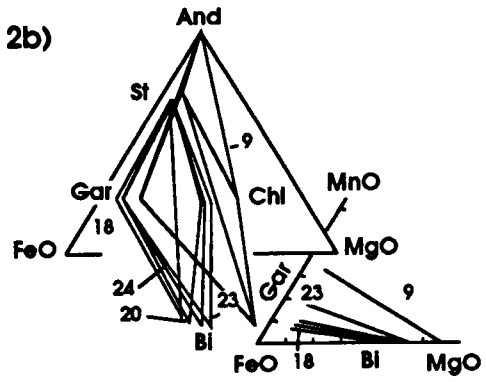
The garnet zone is bounded to the south by a staurolite + chlorite +

Figure 2.2. Mineral compositions (mole fractions), projected from muscovite and quartz onto the AFM plane. Garnet and biotite compositions are plotted on the Fe-Mg-Mn plane.

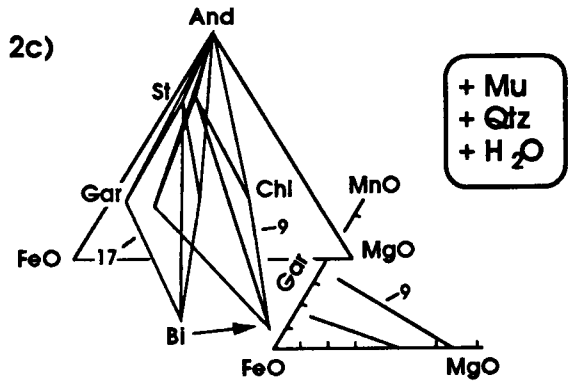
GARNET ZONE



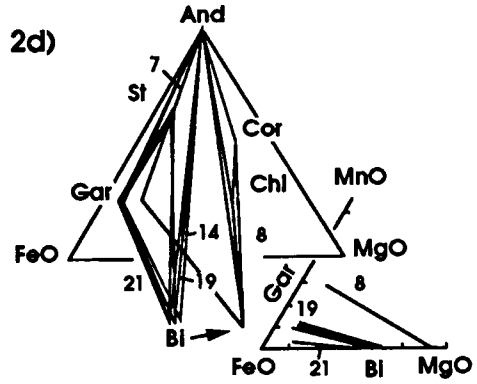
STAUROLITE ZONE



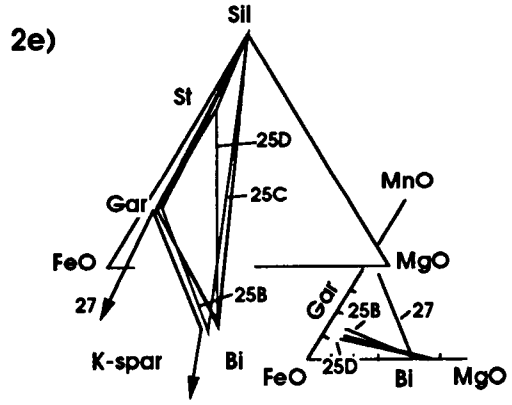
ANDALUSITE + BIOTITE ISOGRAD



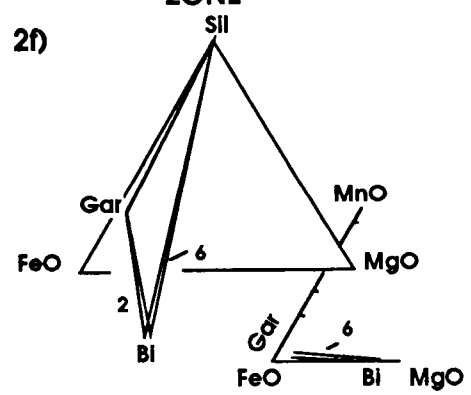
ANDALUSITE + BIOTITE ZONE



SILLIMANITE ZONE



SILLIMANITE + BIOTITE +GARNET ZONE



biotite zone. The mineral associations in the staurolite + chlorite + biotite zone (Figure 2.2b) include

staurolite + biotite + garnet + chlorite + muscovite +

plagioclase (An_{15-20}) + quartz + ilmenite

and

staurolite + biotite + garnet + muscovite + plagioclase (An_{11})

+ quartz + ilmenite.

Although tie lines between staurolite + biotite and chlorite + garnet cross on the AFM plane (Figure 2.2b), garnet in staurolite + chlorite + biotite-bearing assemblages is spessartine-rich (8.7-17.2 mole %) and does not really plot on the AFM plane. Garnet in chlorite-absent assemblages is lower in spessartine component (3.3-6.3 mole %).

The andalusite + biotite zone is characterized by the assemblages (Figures 2.2c and 2.2 d)

andalusite + staurolite + biotite + garnet + muscovite +

plagioclase (An_{15-23}) + quartz + ilmenite,

staurolite + biotite + garnet + muscovite + plagioclase (An_{11-27})

+ quartz + ilmenite,

staurolite + andalusite + biotite + chlorite + garnet + muscovite

+ plagioclase (An_{23}) + ilmenite + magnetite,

and

staurolite + andalusite + biotite + chlorite + garnet + muscovite

+ plagioclase (An_{15}) + ilmenite.

Garnet rims, in andalusite-bearing assemblages, contain 10-27 mole %

spessartine, whereas, garnet in Fe-rich andalusite-absent assemblages contains only 3-6 mole % spessartine (Figures 2c and 2d). Although tie lines cross on the AFM plane, Mn in garnet allows tie lines between Mg-rich compositions of biotite and staurolite to extend to Mn-rich compositions of garnet without crossing tie lines (see the FMM plane in Figure 2.2d).

Andalusite + chlorite + staurolite + biotite assemblages occur at the andalusite + biotite isograd. Sample 9 (Figure 2.2b and 2c) contains staurolite with $X_{Fe}^{St} = 0.80$, biotite with $X_{Fe}^{Bi} = 0.38$, and chlorite with $X_{Fe}^{Chl} = 0.32$. These values of X_{Fe} are extremely low relative to other andalusite + biotite + staurolite assemblages, which have values such as $X_{Fe}^{St} = 0.88$, $X_{Fe}^{Bi} = 0.58$, and $X_{Fe}^{Chl} = 0.62$. Tie lines between AFM phases in sample 9 cross tie lines of AFM phases from other andalusite + biotite assemblages (Figure 2.2c); however, there are no crossing tie lines between sample 9 and surrounding staurolite + chlorite + biotite-bearing assemblages (Figure 2.2b).

Mg-rich rocks in the Thompson Draw synform contain the assemblage

cordierite + andalusite + biotite + chlorite + muscovite

+ plagioclase (An_{21}) + quartz + hematite

at approximately the same metamorphic grade that staurolite + andalusite + biotite coexist. Chlorite, plotted on Figure 2.2d, has distinct grain boundaries and appears to be in textural equilibrium with cordierite and biotite. Commonly, cordierite occurs in andalusite-absent subsets of the above assemblages and has been partially or completely replaced by retrograde chlorite.

The sillimanite zone is characterized by the assemblage (Figure 2.2e)

sillimanite + staurolite + garnet + biotite + muscovite +

plagioclase (An_{11-21}) + quartz + ilmenite

and

sillimanite + biotite + garnet + muscovite + plagioclase(An_{11-18})
+ quartz + ilmenite

There is little difference between the compositions of phases from the sillimanite zone and those occurring in the andalusite-biotite zone. Although sillimanite almost always occurs as fibrolite, subordinate amounts of prismatic sillimanite are present close to the sillimanite isograd. Staurolite shows evidence of reaction at the sillimanite isograd.

In higher-grade sillimanite-bearing schists, staurolite is present only as inclusions in plagioclase (sample 2) or muscovite (sample 6). Mineral compositions in the assemblage

sillimanite + biotite + garnet + plagioclase (An_{18}) + muscovite + ilmenite,

are shown in Figure 2.2f. Although this assemblage also occurs at lower grades, garnet coexisting with biotite and Al_2SiO_5 does not plot near the AFM plane until staurolite has completely reacted away. The association sillimanite + biotite + garnet, with garnet containing ≤ 3 mole % spessartine, marks the garnet + biotite + sillimanite zone.

Gneisses on the southwestern flank of the Harney Peak granite contain the sillimanite + K-feldspar zone assemblages

sillimanite + biotite + garnet + muscovite + albite +
microcline (Or_{93}) + plagioclase (An_{20}) + quartz,

Garnet is rare in the sillimanite + K-feldspar zone and commonly occurs as small anhedral crystals. Muscovite is also commonly absent, although in

any particular outcrop, both muscovite-present and muscovite-absent assemblages occur. Alkali feldspar is subsolvus, consisting of albite (An_{0-2}) and microcline (Or_{90-93}). Microcline also contains fine (~1.0 μm) exsolution lamellae of albite (~An_{2-6}).

The abundance of minor components in minerals is not strongly related to metamorphic grade. The amount of grossular component in garnet rims is very low at all grades: 0.5-5.5 mole %. Grossular component is correlated with the An content of coexisting plagioclase (Figure 2.3), but the amount of Ca in garnet and plagioclase appears to be unrelated to metamorphic grade. However, as discussed in a later section, the ratio of Ca in plagioclase to Ca in garnet is dependent on both temperature and pressure.

REACTION RELATIONS AND THE FACIES SERIES

Assemblages shown in Figure 2.2 define a low-pressure facies series; however, a medium-pressure facies series is preserved in the vicinity of the Bear Mountain dome. An idealized graphical summary of the AFM facies series inferred for the Black Hills, is shown on a schematic psuedobinary T-X_{Mg} diagram (Figure 2.4). Figure 2.4 represents a section along the garnet + chlorite join on the AFM projections in Figure 2.2. The prograde sequence of AFM reactions for the terrain east of the Bear Mountain dome includes

garnet + chlorite + muscovite =

staurolite + biotite + H_2O (1),

staurolite + chlorite + muscovite =

biotite + andalusite + H_2O (2),

chlorite + muscovite =

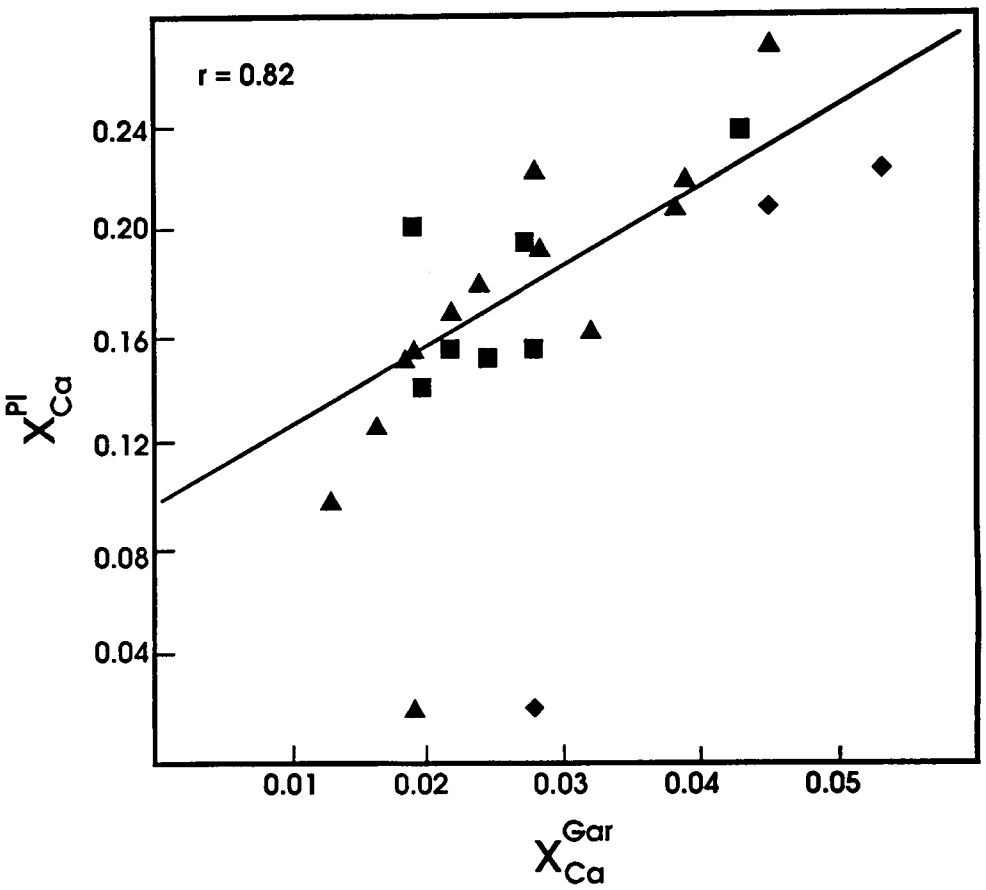
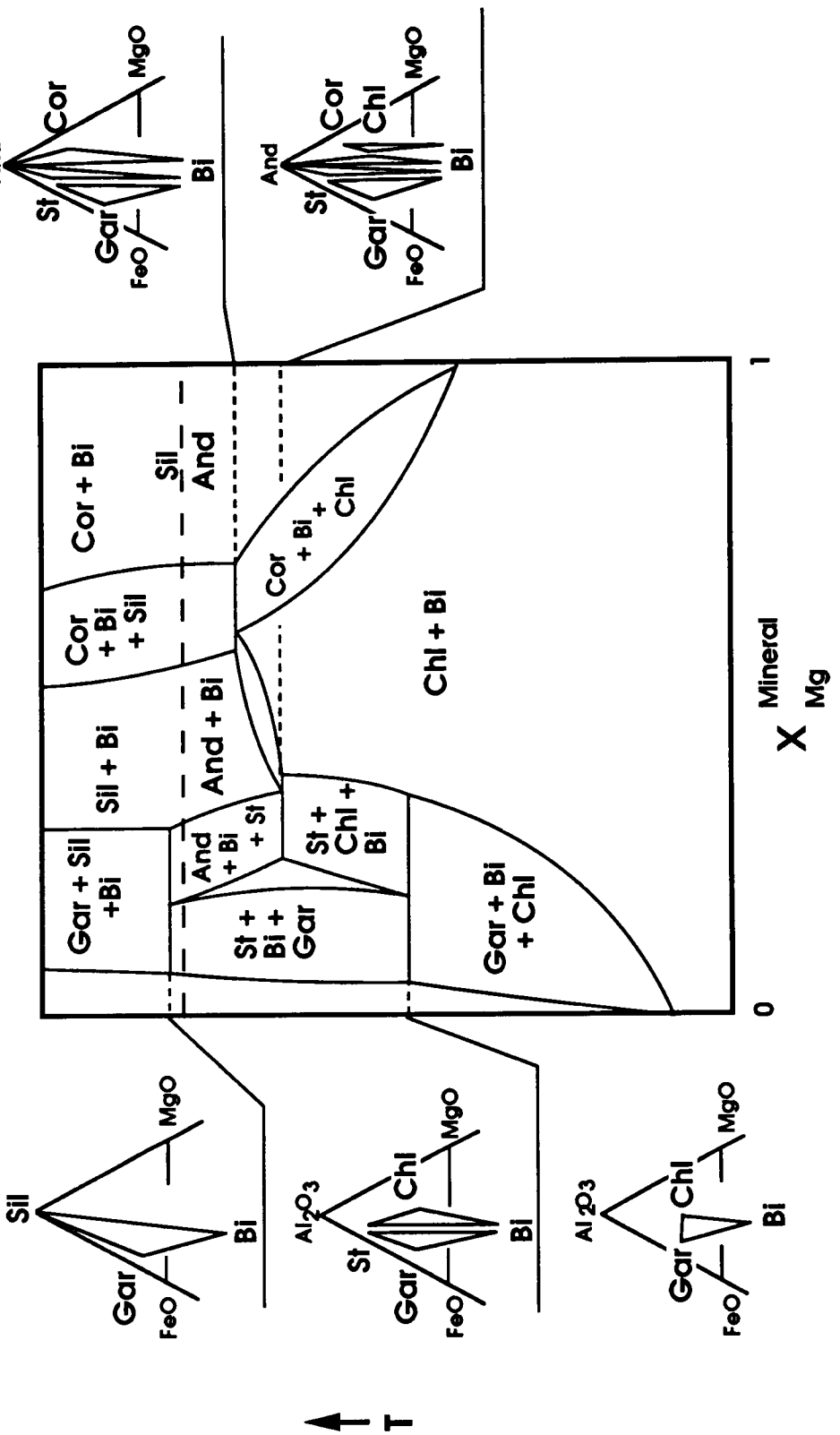


Figure 2.3. Grossular component in garnet plotted relative to anorthite component in coexisting plagioclase. Triangles represent andalusite + biotite and staurolite + biotite grade rocks, squares represent sillimanite grade rocks, and diamonds represent garnet grade rocks.

Figure 2.4. Idealized AFM facies series based on projections in Figure 2.2. The schematic psuedobinary T-X_{Mg} diagram is a section along the garnet-chlorite join in Figure 2.2a-f. The numbers used to label reactions are the same numbers used in the text.


Cor + Bi
Sil
And
Cor + Bi + Sil
Cor + Bi + Chl
Chl + Bi
Sil + Bi
And + Bi
Gar + Sil + Bi
And + Bi + St
St + Chl + Bi
St + Bi + Gar
Gar + Bi + Chl
0
1
X Mineral Mg
T
And
Cor
MgO
St
Bi
Gar
FeO
Chl
Sil
Al2O3

andalusite + biotite + cordierite + H_2O (3),

andalusite = sillimanite (4),

and

staurolite + muscovite =

garnet + biotite + sillimanite + H_2O. (5)

Each reaction is balanced by an appropriate amount of quartz. Reactions (1), (2), (4), and (5), respectively, correspond to the staurolite-biotite, andalusite-biotite, sillimanite, and garnet + biotite + sillimanite isograds. The facies type for the Bear Mountain area can be created by replacing andalusite with kyanite in the andalusite + biotite + staurolite divariant loop on Figure 2.4. In the Bear Mountain area, the prograde sequence of AFM reactions includes

garnet + chlorite + muscovite =

staurolite + biotite + H_2O, (1)

staurolite + chlorite + muscovite =

biotite + kyanite + H_2O. (6)

Reaction (1) and (6) correspond to the staurolite + biotite and kyanite isograds, respectively.

The AFM projection models reactions in the K_2O-FeO-MgO-Al_2O_3-SiO_2-H_2O system. Using measured mineral compositions from the study area, the stoichiometry of the net reaction occurring at each isograd can be modeled more accurately in the 10 component system SiO_2, Al_2O_3, TiO_2, FeO, MgO, MnO, CaO, K_2O, Na_2O, H_2O, using either a linear least-squares calculatation (Reid and others, 1973) or a linear programming technique (Pigage, 1976; Lang and Rice, 1985). Reactions can be modeled either using mineral compositions from samples on both sides of an isograd or by using

mineral compositions from samples that contain all the phases thought to be involved in the isograd reaction. Linear least-squares equations were balanced with measured oxide weight percentages; no attempt was made to estimate the amount of H_2O in hydrous phases. Averaged mineral compositions used in mass-balance calculations are listed in Table 2.2. The average garnet compositions listed in Table 2.2 are taken from rim analyses only.

Mass-balance equations written for the staurolite + biotite, andalusite + biotite, sillimanite + biotite + garnet, and sillimanite + K-feldspar isograds are listed in Table 2.3. The net-reaction at the staurolite + biotite isograd,

garnet + chlorite + muscovite + ilmenite =

staurolite + biotite + plagioclase + quartz + H_2O (1a),

was modeled with measured mineral compositions from sample 21 that contained all the phases present in reaction (1). Sample 21 was chosen because garnet contained almost no spessartine (~ 1 mole %). The reaction

staurolite + chlorite + muscovite + ilmenite =

andalusite + biotite + garnet + plagioclase + quartz + H_2O (2a)

was balanced with mineral compositions from sample 17, collected at the andalusite + biotite isograd. The staurolite-out reaction

staurolite + muscovite + plagioclase(1) + quartz =

sillimanite + biotite + garnet + plagioclase(2) + ilmenite + H_2O (5a)

was modeled with mineral compositions from staurolite-grade sample 1 and sillimanite + biotite + garnet-grade sample 2.

Residuals on (1a), (2a), and (5a) are < 0.1 weight % for the major components and typically < 1.0 weight % for minor components. The quality

TABLE 2.2 Mineral Compositions Used in Mass-Balance Calculations

	REACTION (1a)						REACTION (2a)					
	(4)	(5)	(9)	(3)	(6)	(5)	(3)	(5)	(3)	(6)	(2)	(10)
	Pl21	Gar21	Bi21	Chl21	St21	Mu21	Pl17	Bi17	Chl17	St17	Mu17	Gar17
SiO_2	65.87	36.31	34.64	24.04	27.33	46.86	63.85	35.05	23.33	27.17	46.44	36.67
Al_2O_3	21.67	21.36	20.75	21.75	53.58	36.05	22.74	19.26	22.78	54.03	36.86	20.78
TiO_2	---	---	1.37	0.04	0.48	0.28	---	1.48	0.11	0.21	0.27	0.02
FeO	---	38.58	20.64	28.09	14.66	1.16	0.01	22.13	28.48	13.76	0.83	34.05
MnO	---	1.53	8.45	12.56	1.33	0.57	---	8.42	11.80	1.12	0.38	1.66
MgO	---	1.50	0.09	0.13	0.43	---	---	0.09	0.21	0.33	---	6.45
CaO	2.67	0.66	---	0.08	---	---	3.56	---	0.00	---	---	0.93
Na_2O	10.30	---	0.36	---	---	1.49	9.81	0.18	---	---	1.65	---
K_2O	0.04	---	9.15	---	---	9.27	0.05	9.07	---	---	8.94	---

	REACTION (5a)						REACTION (6a)					
	(21)	(8)	(9)	(6)	(6)	(7)	(9)	(3)	(6)	(9)	(6)	(9)
	Gar2	Pl2	Bi2	St1	Mu1	Pl1	Bi3	Ab3	Pl2	Mu2	Ksp3	Pl3
SiO_2	36.46	64.31	33.99	27.62	46.49	61.84	35.18	68.44	64.31	45.78	64.50	62.92
Al_2O_3	21.01	22.41	19.54	53.32	35.44	24.26	18.98	19.89	22.41	36.40	18.41	23.41
TiO_2	0.02	---	1.91	0.62	0.41	---	2.70	---	---	0.48	---	---
FeO	39.30	0.11	24.85	14.40	1.03	0.12	19.73	0.09	0.11	1.12	0.05	0.10
MnO	1.06	---	0.03	0.16	---	---	0.20	---	---	---	---	---
MgO	1.76	0.06	6.26	1.53	0.69	---	8.50	---	0.06	0.35	---	---
CaO	0.89	3.32	---	---	---	5.70	---	0.31	3.32	---	0.01	4.42
Na_2O	---	9.74	0.22	---	1.04	8.36	0.08	11.54	9.74	1.19	0.74	9.04
K_2O	---	0.05	8.97	---	9.37	0.05	9.82	0.10	0.05	9.60	15.84	0.17

Note: The number in parenthesis above each mineral composition is the number of analyses used in the average. Garnet compositions are from rim analyses.

Table 2.3. Least-Squares Mass-Balance Equations and Residuals

STAUROLITE + BIOTITE ISOGRAD

(1a) 1.74 gar + 5.36 chl + 7.94 mu + 0.21 ilm =
8.07 bi + 2.38 and + 0.29 pl(an12) + 1.00 qtz + (H_2O)

ANDALUSITE + BIOTITE ISOGRAD

(2a) 1.41 chl + 0.48 st + 2.18 mu + 0.04 ilm =
2.15 bi + 2.38 and + 0.29 pl(an15) +0.09 gar +1.00 qtz + (H_2O)

SILLIMANITE + BIOTITE + GARNET ISOGRAD

(4a) 4.98 st + 0.96 mu + 0.46 pl(an_{23}) + 0.47 qtz =
4.08 sil + 1.00 bi + 1.18 gar + pl(an_{15}) + 0.03 ilm + (H_2O)

SILLIMANITE + K-FELDSPAR ISOGRAD

(6a) 1.80 mu + 4.36 pl(an_{15}) + 0.20 qtz =
0.68 sil + 1.00 Ksp(or_{93}) + 1.31 ab + 3.19 pl(an_{19}) + 0.11 bi + (H_2O)

	(1a)		(2a)		(5a)		(6a)	
	r	r/v	r	r/v	r	r/v	r	r/v
SiO_2	-0.01	0.01	-0.02	0.06	0.00	0.00	0.00	0.00
Al_2O_3	0.00	0.00	0.03	0.02	0.00	0.00	0.00	0.00
TiO_2	0.00	0.11	0.09	0.41	0.57	5.58	0.57	5.52
FeO	-0.01	0.00	-0.10	0.23	0.02	1.48	-0.06	0.25
MgO	0.03	0.02	0.21	0.36	0.02	1.10	-0.02	0.40
MnO	0.70	2.73	0.30	0.51	-0.20	3.43	0.05	0.76
CaO	-0.68	11.98	1.11	3.35	0.00	0.15	0.00	0.00
Na_2O	0.24	0.21	-0.36	12.47	0.00	0.00	0.00	0.00
K_2O	0.01	0.00	0.04	4.45	-0.02	0.07	-0.02	0.04
$\sqrt{\Sigma r^2}$	1.01		1.23		0.61		0.58	

Note: Mineral compositions used in the mass-balance equations are listed in Table 2.2. Mineral abbreviation: ab, albite; and, andalusite; an, anorthite; bi, biotite; chl, chlorite; gar, garnet; ilm, ilmenite; ksp, K-feldspar; mu. muscovite; pl, plagioclase; sil, sillimanite; st, staurolite; r is the residual (weight %) on each oxide. r/v is the residual on an oxide divided by the measured variation (1 standard deviation about the average) on that oxide. The variation v is weighted by the stoichiometric coefficients of the mass-balance equation. No attempt was made to estimate H_2O content in minerals; therefore, (H_2O) is qualitatively listed on the side of the equation interpreted to be prograde. Ilmenite, quartz, and aluminum silicate are $FeTiO_3$, SiO_2, and Al_2SiO_5, respectively.

of fit on each oxide is evaluated by calculating the ratio of the residual r to the weighted sum of the variation v measured on the oxide (Table 2.3). The observed variation (1σ about the average) on each oxide is weighted by the stoichiometric coefficients of the mass-balance equations in Table 2.3. A r/v ratio less than 1 indicates the residual is within the measured range of variation. A r/v ratio greater than 1 indicates a poor fit on a particular oxide.The least-squares calculation produces the minimum value of $\sqrt{\Sigma r^2}$; consequently, error is concentrated in minor components, and r/v ratios that exceed 1 are commonly confined to the minor components. Attempts to weight minor components to improve r/v ratios, simply resulted in major-component r/v values exceeding 1. The lack of fit for reactions (1a), (2a), and (5a) is a measure of the thermodynamic variance of the reactions at the isograds. For example, an invariant assemblage would have an equal number of phases and components and a perfect fit would be achieved if mineral compositions from the sample were used to balance a reaction. The residuals listed in Table 2.3 indicate that the reactions at the isograds are continuous. However, the value of $\sqrt{\Sigma r^2}$ is commonly < 1, indicating that the reactions have a low-thermodynamic variance.

On the southern flank of the Harney Peak granite muscovite is replaced in varying degrees by sillimanite and alkali feldspars. This reaction is observed in both the country rock and in adjacent sills and dikes of granite. Mineral compositions (Table 2.2) from sillimanite-grade sample 2 and sillimanite + K-feldspar sample 3 were used in a least-squares model for the sillimanite - K-feldspar isograd. The results indicate that the net reaction

muscovite + plagioclase (An_{15}) + quartz =

albite + K-feldspar + sillimanite + plagioclase (An_{19}) + biotite + H_2O (7),

occurred at the muscovite-out isograd. Stoichiometric coefficients are given in Table 2.3.

METAMORPHIC CONDITIONS

Temperatures have been estimated from the Fe-Mg-exchange equilibrium between garnet and biotite, based on the experimental Fe-Mg exchange data of Ferry and Spear (1978) and the activity-composition model of Ganguly and Saxena (1984; 1985). Although garnets are commonly zoned, garnet-rim compositions were used for geothermometry. Rim values may not always reflect maximum temperatures; however, the values of X_{Fe}^{Bi} in equilibrium with garnet cores are uniquely defined if and only if the rock has a thermodynamic variance ≤ 3, if the mineral assemblage that was in equilibrium with the the garnet core is known, and if the garnet has not undergone significant volume diffusion (Spear and Selverstone, 1983). A detailed analysis of compositionally zoned garnets is presented in Helms and Labotka (1990; 1991).

The Ganguly and Saxena model corrects for the effects of Mn and Ca on Fe-Mg mixing in garnet. Temperatures estimated with the Ganguly and Saxena (1984) garnet-biotite thermometer, with the compositional data in Table 2.4, are typically 30-40 °C higher than temperatures estimated with the calibration of Ferry and Spear (1978) (Table 2.5). As demonstrated below, the Ganguly and Saxena (1984) calibration produces results consistent with other phase equilibria; therefore, temperatures discussed here are based on the Ganguly and Saxena (1984) calibration. The calibration of Hodges and Spear (1982) corrects only for Ca in garnet; however, the Ca content in garnet is

Table 2.4. Mineral Compositions Used to Estimate Temperature Pressure and a_{H_2O}.

	Garnet			Biotite		Muscovite			Plag.	Chl.
	X_{Alm}	X_{Gro}	X_{Sps}	X_{Ann}	X_{Phl}	X_K	X_{Na}	X^{IV}_{Al}	X_{An}	X_{Cli}
1	0.788	0.072	0.045	0.429	0.375	0.796	0.134	0.940	0.273	------
2	0.895	0.018	0.023	0.539	0.240	0.815	0.154	0.949	0.158	------
3	0.750	0.020	0.140	0.421	0.324	0.931	0.053	0.927	0.202	------
4	------	------	------	0.432	0.301	0.924	0.049	0.936	0.198	------
5	0.748	0.024	0.150	0.446	0.321	0.849	0.130	0.946	0.196	------
6	0.864	0.052	0.034	0.537	0.215	0.831	0.052	0.940	0.230	------
8	0.534	0.048	0.303	0.312	0.497	0.755	0.234	0.916	0.220	0.585
9	0.540	0.044	0.293	0.291	0.538	0.760	0.201	0.881	0.242	0.617
10	0.726	0.028	0.171	0.436	0.375	0.854	0.103	0.942	0.021	0.440
11	0.639	0.043	0.231	0.381	0.441	0.818	0.145	0.902	0.207	0.500
12	0.638	0.056	0.266	0.474	0.327	0.852	0.077	0.880	0.225	0.384
13	0.876	0.047	0.020	0.508	0.294	0.823	0.151	0.934	------	------
14	0.798	0.019	0.111	0.454	0.336	0.779	0.190	0.942	0.156	------
15A	0.763	0.038	0.115	0.443	0.337	0.788	0.186	0.954	0.196	------
15B	0.805	0.028	0.100	0.464	0.313	0.780	0.179	0.948	0.169	------
16	0.790	0.025	0.106	0.458	0.334	0.809	0.191	0.934	0.176	------
17	0.770	0.027	0.131	0.453	0.339	0.755	0.216	0.964	0.154	0.377
18	0.834	0.020	0.063	0.432	0.359	0.779	0.201	0.942	0.125	------
19	0.828	0.019	0.095	0.485	0.305	0.785	0.138	0.955	0.020	------
20	0.796	0.031	0.087	0.420	0.389	0.777	0.204	0.939	0.181	0.448
21	0.872	0.019	0.033	0.466	0.329	0.781	0.198	0.955	0.156	0.407
22	0.769	0.043	0.112	0.452	0.338	0.772	0.176	0.947	0.215	------
23	0.696	0.031	0.172	0.392	0.428	0.760	0.223	0.924	0.183	0.502
24	0.781	0.032	0.100	0.426	0.376	0.729	0.257	0.933	0.160	0.455
25A	0.786	0.028	0.122	0.449	0.316	0.781	0.185	0.957	0.128	------
25B	0.768	0.024	0.138	0.469	0.318	0.773	0.158	0.955	0.154	------
25C	0.799	0.021	0.109	0.460	0.323	0.807	0.174	0.944	0.163	------
25D	0.785	0.024	0.120	0.469	0.321	0.766	0.179	0.958	0.147	------
27	0.495	0.060	0.411	0.468	0.322	0.962	0.032	0.888	0.230	------
28	0.790	0.055	0.092	0.468	0.316	0.815	0.185	0.954	0.155	------
29	0.745	0.047	0.086	0.362	0.392	0.802	0.121	0.899	0.254	------

Note: Averaged mineral compositions and average garnets rim compositions; X_{Alm} = Fe/(Fe + Mg + Mn + Ca), X_{Gro} = Ca/(Fe + Mg + Mn + Ca), X_{Sps} = Mn/(Fe + Mg + Mn + Ca), X_{Ann} = Fe/3, X_{Phl} = Mg/3, X_K = K, X_{Na} = Na, X^{IV}_{Al} = Al /2, X_{An} = Ca, X_{Cli} = Mg/5; Fe is assumed to be all Fe^{2+}.

Table 2.5. Comparative Results of Geologic Thermometry and Barometry

Sample	GB		AMPH		GBSH	GASP			AS	GBMP
	FS T (°C)	GS T (°C)	T(max) (°C)	a_{H2O}	a_{H2O}	IS P (kbar)	GS P (kbar)	NH P (kbar)	P (kbar)	P (kbar)
					Sillimanite Zones					
2	537	582	≤564	1.14	----	3.46	1.05	4.10	>2.59	3.35
28	454	528	≤566	0.70	----	3.53	1.99	4.10	>3.43	5.45
25B	483	549	≤551	0.99	----	3.40	1.68	4.04	~3.09	3.30
6	504	551	≤560	0.92	----	3.43	2.29	3.91	>3.08	4.15
5	511	543	≤548	0.96	----	2.48	1.32	3.11	>3.18	2.70
3	520	563	≤662	0.43	----	2.02	0.49	2.72	>2.89	3.54
27	487	527	----	----	----	----	----	----	-----	3.83
					Andalusite + biotite zone					
9	463	505	≤529	0.78	0.79	3.09	3.69	4.17	<3.68	3.66
15A	503	545	≤540	1.10	----	2.17	0.88	2.45	<3.64	3.98
8	483	534	≤537	0.98	----	3.31	3.77	4.52	<3.50	4.22
19	431	480	≤558	0.45	----	----	----	----	----	---
-										
14	455	501	≤511	0.90	----	2.02	0.71	2.78	<3.77	2.55
22	451	531	≤511	1.24	----	2.19	1.50	2.95	~3.35	3.89
17	461	513	≤517	0.98	1.07	2.28	1.35	2.98	<3.60	2.96
					Kyanite zone					
29	523	530	≤533	0.98	----	4.48	3.61	4.07	>4.20	4.22
					Staurolite + chlorite + biotite zone					
24	468	501	----	----	0.92	----	----	----	----	3.63
23	481	518	----	----	0.89	----	----	----	----	3.50
20	443	474	----	----	0.81	----	----	----	----	2.63
21	458	488	----	----	0.76	----	----	----	----	2.56
					Garnet -zone					
12	390	469	----	----	0.97	----	----	----	----	3.50
10	515	492	----	----	0.84	----	----	----	----	----
11	448	500	----	----	0.79	----	----	----	----	3.65

Note: GB - garnet-biotite geothermometer, FS- Ferry and Spear (1978) calibration of the garnet-biotite geothermometer, GS- Ganguly and Saxena (1984) corrected version of the garnet-biotite geothermometer; AMPH - aluminum silicate + muscovite + plagioclase + quartz + H2O equilibria, the activity of paragonite component was estimated from Chatterjee and Froese (1975); GBCH - garnet + chlorite + biotite + muscovite + quartz + H2O equilibria (reaction 13 estimated from Holland and Powell, 1985); GASP - garnet + aluminum silicate + plagioclase + quartz geobarometer based on reaction (8), IS - GASP geobarometer, the activity of anorthite estimeted from Saxena and Ribbe (1972) and the activity of grossular is estimated as ideal, GS - GASP geobarometer, the activity of anorthite is estimated from Saxena and Ribbe (1972) and the activity of grossular is estimated from Ganguly and Saxena (1984), NH - GASP geobarometer where the activties of grossular and anorthite are estimated with the models in Newton and Haselton (1981); AS - aluminum silicate equilibria from Holdaway (1971); GBPM - garnet + biotite + plagioclase + muscovite equilibria (Ghent and Stout, 1981).

very small ($X_{Gro} \leq 0.03$) and should have negligible effect on estimated temperatures. Indares and Martignole (1985) derived activity expressions for Ti and ^{VI}Al in biotite at granulite facies conditions; however, for amphibolite-facies conditions experienced in the Black Hills, we have assumed ideal mixing in biotite.

Temperatures estimated with the garnet-biotite thermometer are plotted on Figure 2.5 and contoured at 30 °C intervals. The accuracy of the garnet-biotite thermometer was reported as ±50 °C (Ferry and Spear, 1978); however, it is assumed that this uncertainty is present at the same unknown value in each sample. The contour interval produces results consistent with the isograds suggesting that the precision of the thermometer is close to ±30 °C. Garnet-biotite thermometry indicates that temperatures increased southward, with a high-temperature anomaly occurring adjacent to the Harney Peak granite (Figure 2.5). Average temperatures in the garnet zone range from 469 to 500 °C (Table 2.4), reflecting temperatures near the staurolite + biotite or andalusite + biotite isograds. The average temperatures for the different zones are 480 to 518 °C in staurolite + chlorite + biotite zone, 501 to 545 °C in the andalusite + biotite zone, 527 to 549 °C in the sillimanite zone, 551 to 583 °C in the garnet + biotite + sillimanite zone and ~ 563 °C in sillimanite + K-feldspar zone. A sample from the kyanite zone indicate a temperature of range of 520 to 540 °C.

Pressure was estimated with the reactions

andalusite = sillimanite, (8a)

andalusite = kyanite (8b)

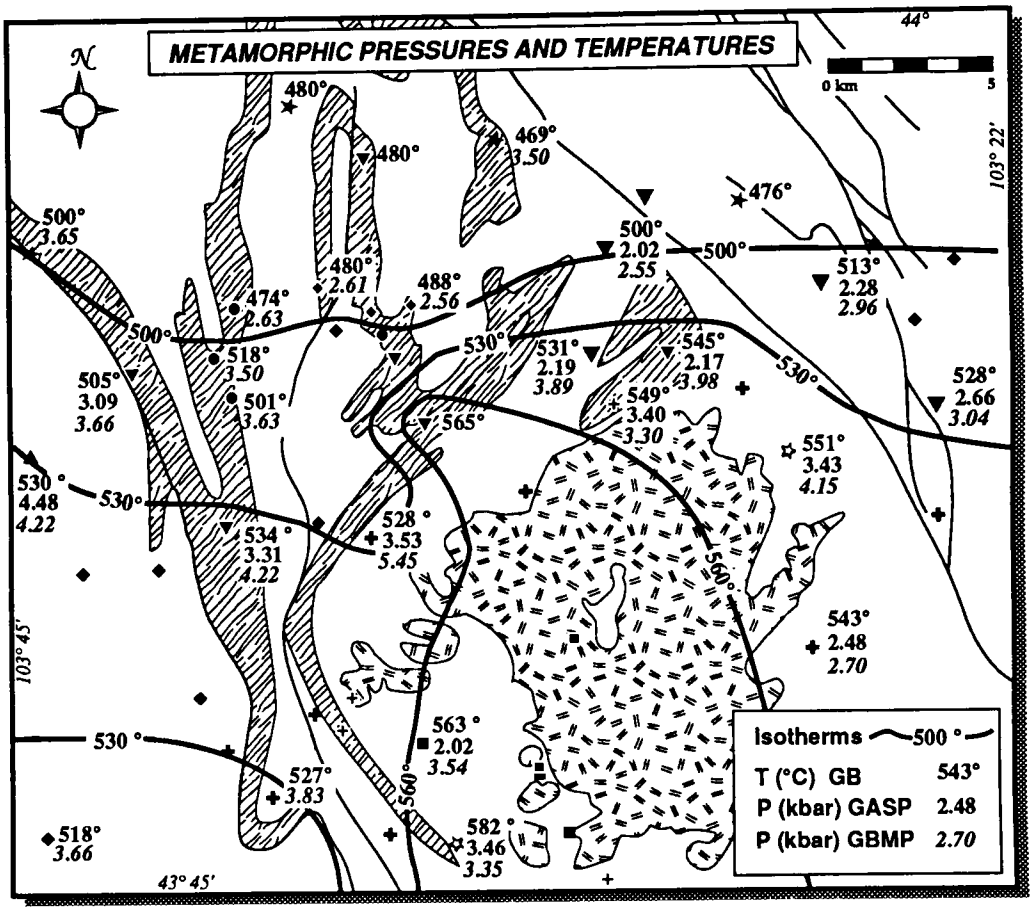


Figure 2.5. Metamorphic temperatures and pressures plotted on a simplified geologic map of the study area. Isotherms based on temperatures estimated with the Ganguly and Saxena (1984) garnet-biotite thermometer are plotted at a 30 °C contour intervals.

$$3 \text{ anorthite} = \text{grossular} + 2\ Al_2SiO_5 + \text{quartz}, \quad (9)$$

and

$$\text{annite} + 3 \text{ anorthite} = \text{almandine} + \text{grossular} + \text{muscovite}. \quad (10)$$

Reactions (8a) and (8b) are from Holdaway (1971). Reaction (9) was calibrated in the kyanite field (Koziol and Newton, 1988); therefore, reaction (8b) and reaction (9) were combined in order to estimate pressure in the andalusite zone. The P-T coordinates of reaction (10) were empirically determined by Ghent and Stout (1981).

The equilibrium constant for reaction (9) was estimated using three different models; the results from several representative samples are presented for comparison in Table 2.5. Although the Ganguly and Saxena (1984; 1985) formulation adequately models the activities of Fe and Mg in garnet, it fails to model the activity of Ca in garnet at concentrations ≤ 3 mole %. This failure results in unrealistically low-pressures (0.9-1.5 kbar). The activity model of Newton and Haselton (1981) resulted in more reasonable estimates; however, pressures tended to be high relative to the sillimanite-andalusite curve (e.g. samples 9 and 8, Table 2.5). Nearly ideal behavior of grossular component at dilution (< 10 mole %) in almandine garnet was observed by Cressey and others (1978). Koziol (1990) also inferred nearly ideal mixing of grossular in spessartine garnets. Garnets analyzed in this study are dominantly composed of almandine and spessartine (Table 2.5); therefore, grossular at dilution may behave ideally.

Pressure estimates that incorporate the activity expression for anorthite derived by Saxena and Ribbe (1972) from the data of Orville (1972) and an ideal solution model for grossular in garnet are in good

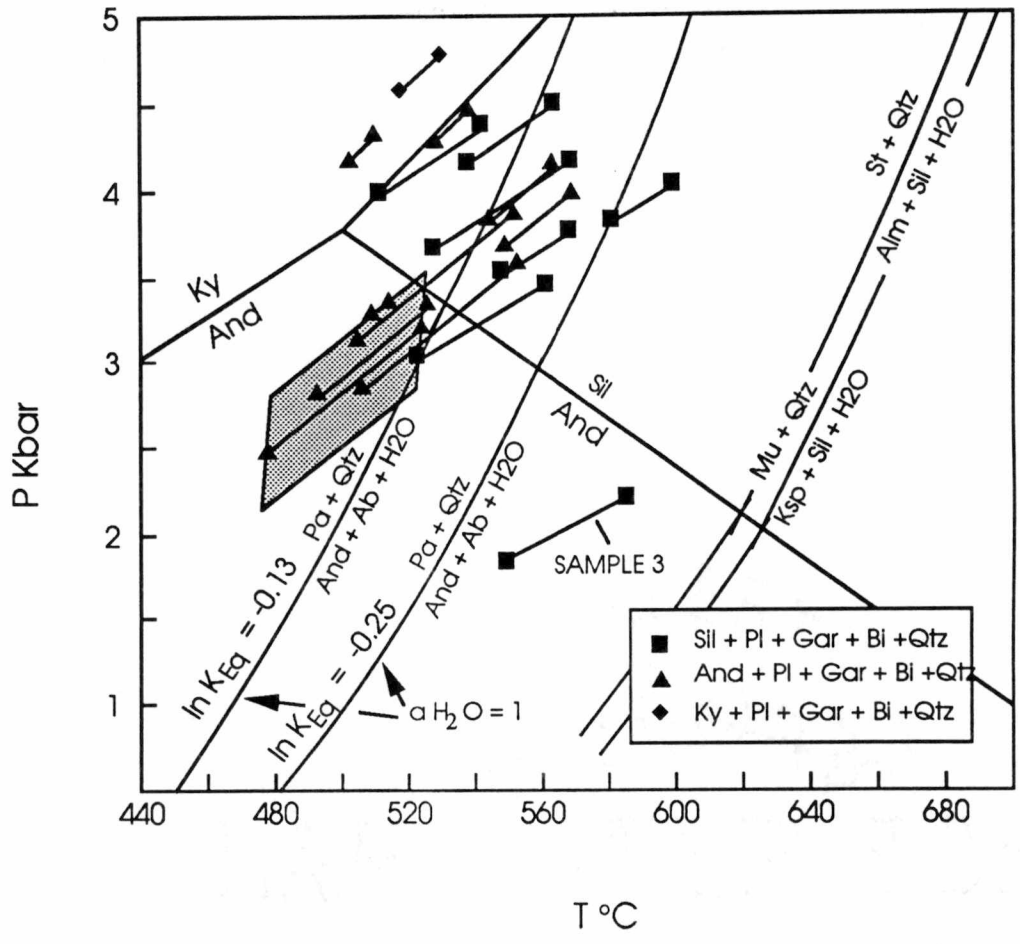


Figure 2.6. P-T conditions based on garnet-biotite thermometry and garnet- plagioclase (GSAP) geobarometry. Diagonal error-bars reflect one standard deviation about the average temperature calculated from the garnet + biotite geothermometer (Ganguly and Saxena, 1984). The variation in pressure results from the temperature dependence of the GASP barometer. The shaded polygon is a representative example of the error generated from variability in biotite, plagioclase and garnet compositions. The Al_2SiO_5 triple point is from Holdaway (1971), the muscovite + quartz stability curve is from Chatterjee and Johannes (1974), the paragonite + quartz stability curve is after Chatterjee (1971), and the staurolite + quartz stability curve is after Holdaway and others (1988).

agreement with the aluminum silicate phase diagram (Figure 2.6, Holdaway, 1971). Pressures based on reaction (9), that are reported in the remainder of the text, incorporate an ideal garnet mixing model for grossular and the Saxena and Ribbe (1972) mixing model for plagioclase.

Metamorphic pressures based on garnet-rim and matrix mineral compositions are plotted on Figure 2.5. Temperature estimates near the sillimanite isograd (reaction 8a) indicate a pressure of ~3 kbar. The presence of andalusite at the andalusite-biotite (~500 $^{\circ}$ C) isograd implies a maximum pressure of 3.7 kbar. Kyanite in the Bear Mountain dome indicates a minimum pressure of 4.3 kbar at 530 °C. Calculated temperatures and pressures with estimated error (1σ) are plotted on Figure 2.6. Temperature ranges shown on Figure 2.6 reflect compositional variation in garnet-rim and matrix biotite compositions. The pressure variation reflects the temperature dependence of reaction (9). The pressure range resulting from variation in measured plagioclase and garnet compositions has been excluded for clarity. However, one representative error polygon reflecting variation in plagioclase, biotite, and garnet compositions is shown as the shaded polygon in Figure 2.6. Activity-composition relations are still poorly understood for 4-component garnets (Koziol, 1990) and plagioclase (Carpenter and Ferry, 1984). We suggest that much of the pressure variation observed in the study area is within the uncertainty of the barometer due to poorly known activity-composition relationships.

Estimated pressure and temperature for samples close to the sillimanite-andalusite isograd fall near the sillimanite-andalusite reaction

curve, and pressure-temperature estimates typically fall near to, or in the appropriate aluminum silicate field. Sample 3 from the sillimanite + K-feldspar zone (Figure 2.6) records a pressure of 2.0 kbars and an average temperature of 563 °C this temperature and pressure are inconsistent with the aluminum silicate phase diagram (Figure 2.6) and indicate retrogradation. The average pressure for the study area is 3.0 ± 0.60 kbar (Table 2.5). The increase in pressure (4.4 kbar) in the Bear Mountain dome is consistent with presence of kyanite there.

The empirically derived geobarometer based on reaction (10) provides a means of estimating pressure with samples lacking an aluminum silicate. K_{eq} was calculated with the activity-composition models used by Ghent and Stout (1981). Estimates based on reaction (10) indicate a pressure range of 2.6 to 5.45 kbar (Table 2.4 and Figure 2.5). These estimates are in moderately good agreement with pressures based on reactions (8) and (9). Estimates for the garnet- and staurolite + chlorite + biotite-zones, where no experimentally calibrated barometers can be applied, indicate a pressure of 2.6 to 3.6 kbars.

The fugacity (f) of H_2O has been calculated from the reactions

$$\text{paragonite + quartz = albite + } Al_2SiO_5 + H_2O, \qquad (11)$$

$$\text{muscovite + quartz = K-feldspar + sillimanite + } H_2O, \qquad (12)$$

and,

$$3 \text{ clinochlore + muscovite + 3 quartz =}$$

$$4 \text{ pyrope + phlogopite + 12 } H_2O. \qquad (13)$$

Reactions (11) and (12) were experimentally investigated by Chatterjee (1971) and Chatterjee and Johannes (1974), respectively. The K_{eq} equation

for reaction (13) was estimated with the thermodynamic data of Holland and Powell (1990) and Burnham and others (1969). Reaction (13) was written with Mg-end members, because of the poor quality of most thermodynamic data on Fe-minerals (Newton, 1987; Holland and Powell, 1990). The fugacity (f^*) of pure H_2O was taken from Burnham and others (1969).

Estimated fugacities based on reactions (11), (12), and (13) typically indicate high values of a_{H_2O} ($\geq$ 0.8) in garnet-grade through andalusite + biotite-grade rocks (Table 2.5). Samples 19 is the only andalusite + biotite grade sample that records a significantly low a_{H_2O} (0.47). Sillimanite + muscovite-bearing samples also record high values of a_{H_2O} ($\geq$ 0.7). Sillimanite + K-feldspar-zone samples record low values of a_{H_2O} (0.43-0.60). Reactions (11) and (12) indicate nearly identical values of a_{H_2O}; however, this low value of a_{H_2O} may be a result of an erroneously-low temperature estimate (e.g. sample 3 plotted on Figure 2.6).

Estimated values of a_{H_2O} based on reaction (11) are typically close to 1. Therefore, temperatures based on the garnet-biotite geothermometer are close to the maximum temperature (Table 2.5) consistent with reaction (11). Reaction (11) is plotted on Figure 2.6 at a_{H_2O} = 1 and corrected for the solution of Ca in plagioclase and K in white mica. Two curves are plotted reflecting the extremes of the observed range X_{Na}^{Pl} =0.85 - 0.80 and X_{Na}^{Mu}= 0.25 - 0.15. Temperatures typically fall close to the maximum temperatures (Figure 2.6) estimated with reaction (11). The close agreement between fugacities estimated with reactions (11) and (12) in a sillimanite + K-feldspar rock, suggests that the activity-composition models (sample 3,

Table 2.5) are accurate.

CONTROLS ON ISOGRAD DISTRIBUTION

The distribution of isograds (Figure 2.1) and isotherms (Figure 2.5) record a regional increase in metamorphic temperature towards the south and a sharp increase in temperature near the Harney Peak granite. A high-temperature anomaly adjacent to the granite is signified by the breakdown of staurolite + muscovite + quartz and muscovite + quartz. The distribution of isograds also indicates higher pressure in the Bear Mountain dome and a regional westward-deepening exposure of the metamorphic complex. A regional increase in pressure towards the west and the Bear Mountain dome is also indicated by an increasing westward separation between the staurolite + biotite and andalusite + biotite isograds. A steeper field gradient (dP/dT) intersects the dehydration reactions at a smaller angle, resulting in greater separation of the isograds in the field.

Temperature and pressure dominantly controlled the distribution of isograds in the southern Black Hills. In isolated locations, low values of a_{H_2O} appear to have resulted in the stability of higher-grade assemblages within low-grade zones. Sample 19 contains andalusite + biotite, is located in the garnet zone, and is 6 km north of the andalusite + biotite isograd. Garnet-biotite geothermometry records a temperature of 463-497 °C, consistent with temperatures in the garnet zone; plagioclase + muscovite compositions indicate $a_{H_2O} = 0.49 \pm 0.10$ at this temperature (Table 2.5). A low value of a_{H_2O} explains the occurrence of andalusite + biotite in the garnet zone. Sample 19 also contains peristerite pairs (plagioclase An_2-An_{16-26}) and has a fine-grained texture similar to surrounding garnet-grade

rocks. Within the staurolite + biotite + chlorite and andalusite + biotite zones peristerites are absent, indicating that the solvus closed at or near the temperature associated with the staurolite + biotite isograd (~500 °C). The lower temperature, and therefore lower a_{H_2O}, recorded by sample 19 is supported by the presence of peristerite pairs, the fine-grained texture, and the isolated occurrence of andalusite + biotite in the garnet zone. The reason for the low a_{H_2O} recorded by sample 19 is unknown.

Sample 9 anomalously contains the assemblage andalusite + biotite, within the staurolite zone. Staurolite, biotite, and chlorite in sample 9 are highly enriched in Mg (Figure 2.2b and 2.2c) relative to samples containing andalusite + biotite. Dehydration reactions involving pure Mg components commonly occur at higher temperatures and pressures than their Fe counterparts; therefore, the extreme Mg-enrichment at nearly isobaric-isothermal conditions must result from a lower μ_{H_2O}. The dependence of mineral compositions on μ_{H_2O} in the assemblage andalusite + chlorite + biotite + staurolite was determined from the set of equations given in Table 2.6. This set consists of a Gibbs-Duhem equation for each phase, linearly independent equilibrium equations among the chemical potentials of the phase components (Thompson, 1982), and an equation which introduces the variable of interest dX_{Bi}^{Fe} (Rumble, 1976; Spear and others, 1982). In the absence of explicit thermodynamic data, the equations in Table 2.6 can be integrated from a reference state consisting of mineral compositions at a known pressure and temperature. In the following calculations, the reference state is taken as mineral compositions in sample 13. Simultaneous solution of the equations in Table 2.6 yields the expressions

Table 2.6. System of Homogeneous Differential Equations Necessary to Describe the Relationship Between μH_2O and X_{Mg} in the Assembalges Biotite + Staurolite + Andalusite + Muscovite + Quartz and Staurolite + Chlorite + Biotite + Muscovite + Quartz

$$
\begin{bmatrix}
1 & 0 & 0 & 0 & 0 & 0 & 0 & 0 & 0 & 0 & 0 \\
0 & 1 & 0 & 0 & 0 & 0 & 0 & 0 & 0 & 0 & 0 \\
0 & 0 & 1 & 0 & 0 & 0 & 0 & 0 & 0 & 0 & 0 \\
0 & 0 & 0 & X_{Fe}^{Chl} & X_{Mg}^{Chl} & 0 & 0 & 0 & 0 & 0 & 0 \\
1 & 0 & 0 & 0 & 0 & X_{Fe}^{Bi} & X_{Mg}^{Bi} & 0 & 0 & 0 & 0 \\
1 & 0 & 0 & 0 & 0 & 0 & 0 & X_{Fe}^{St} & X_{Mg}^{St} & 0 & 0 \\
-20 & 69 & 0 & 0 & 62 & 0 & -69 & 0 & -36 & -212 & 0 \\
18 & 8 & -62 & 0 & 0 & 0 & -8 & 0 & 12 & -12 & 0 \\
0 & 0 & 0 & 0 & 0 & 2 & -2 & -3 & 3 & 0 & 0 \\
0 & 0 & 0 & 2 & -2 & -3 & 3 & 0 & 0 & 0 & 0 \\
1 & 0 & 0 & 0 & 0 & 0 & -1 & 0 & 0 & 0 & \left(\frac{\partial^2 g^{Bi}}{\partial X_{Fe}^{Bi\,2}}\right)_{T,P,X_i}
\end{bmatrix}
\bullet
\begin{bmatrix}
d\mu^{Qtz} \\
d\mu^{Mu} \\
d\mu^{And} \\
d\mu^{Fe\text{-}Chl} \\
d\mu^{Mg\text{-}Chl} \\
d\mu^{Fe\text{-}Bi} \\
d\mu^{Mg\text{-}Bi} \\
d\mu^{Fe\text{-}St} \\
d\mu^{Mg\text{-}St} \\
d\mu^{H_2O} \\
d X_{Fe}^{Bi}
\end{bmatrix}
= 0
$$

$$\mu H_2O = (3RT/212) \int \{(64X^{Fe}_{Bi} + 24X^{Fe}_{St} - 93X^{Fe}_{Chl})/X^{Fe}_{Bi}(1-X^{Fe}_{Bi})\} dX^{Fe}_{Bi}$$

for the assemblage staurolite + biotite + chlorite + muscovite + quartz, and

$$\mu H_2O = RT \int \{(X^{Fe}_{Bi} - X^{Fe}_{St})/X^{Fe}_{Bi}(1-X^{Fe}_{Bi})\} dX^{Fe}_{Bi}$$

for the assemblage andalusite + biotite + staurolite + muscovite + quartz. Graphical results (Figure 2.7) of numerically integrating these expressions from X^{Fe}_{Bi}= 0.001 to 0.999 indicate that staurolite + biotite + chlorite are removed to Mg-rich compositions at low values of μH_2O. The assemblage in sample 9 equilibrated in a fluid with μH_2O that was 5000 joules lower than typical staurolite-zone assemblages. This represents a decrease in a_{H_2O} by 1/2, generally consistent with the values of a_{H_2O} calculated for samples 9 (a_{H_2O} = 0.78) and 17 (a_{H_2O} = 0.98) from reaction (11). Sample 9 was collected adjacent to a vein of plagioclase + quartz, and the decreased a_{H_2O} may have resulted from equilibration with a vein fluid with a low a_{H_2O}.

DISCUSSION AND CONCLUSIONS

In the past decade several tectono-thermal models have been proposed to explain regional low-pressure, high-temperature metamorphism (e.g. England and Thompson, 1984; Wickham and Oxburgh, 1985; Lux and others, 1986; Barton and Hanson, 1989; Thompson, 1989; Loosveld and Etheridge, 1990). Any model proposed to explain metamorphism in the Black Hills must account for the following observations: (1) metamorphism began during upright folding (F_2) and after recumbent folding (F_1). (2) Peak metamorphism and intrusion of the Harney Peak granite, occurred after folding and crustal thickening. (3) The

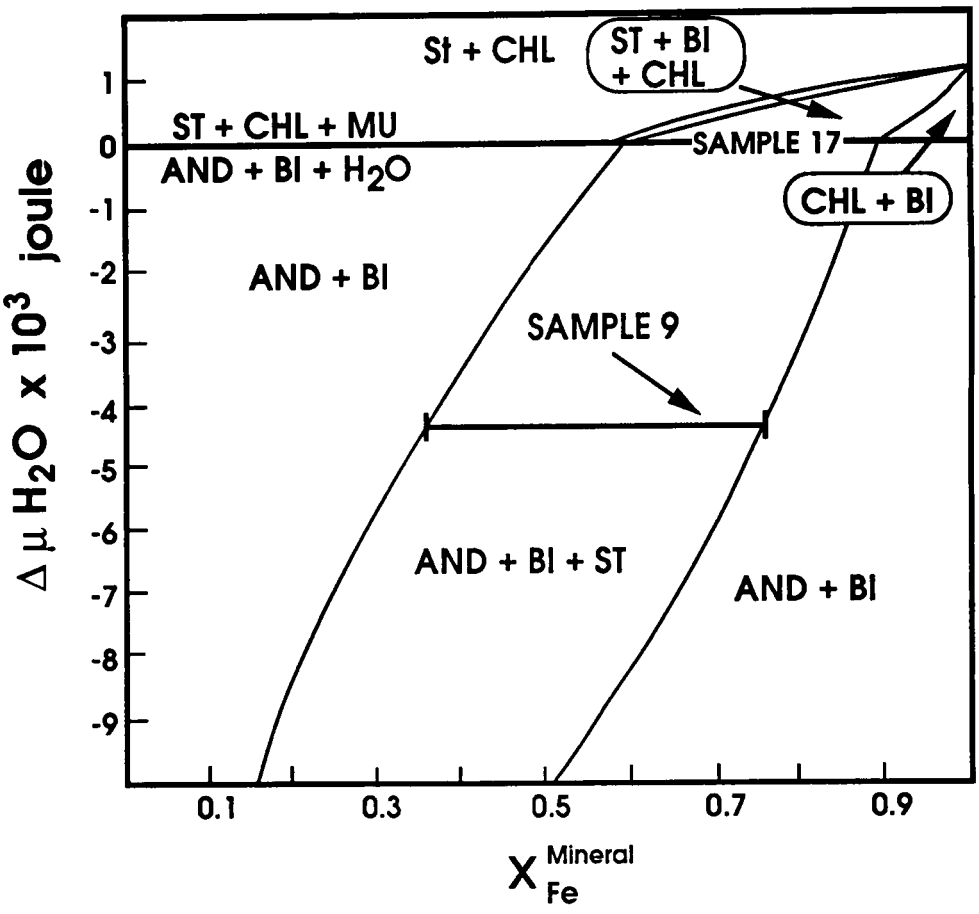


Figure 2.7. $X^{Fe}_{Mineral}$-μ_{H_2O} diagram calculated from the set of Gibbs-Duham relationships between coexisting Fe-Mg silicates

Harney Peak granite was derived from partial melting of sedimentary rock (e.g. Walker and others, 1986). (4) The highest temperatures were attained adjacent to the Harney Peak granite (~650 °C); however, metamorphism is regional and not contact in style. (5) Garnet-grade schists located at substantial distances from the granite contact (10 to 15 km), record temperature to depth ratio that are consistent with high-temperature, low-pressure conditions (~35 °C/km).

Recent studies of regional low-pressure, high-temperature metamorphic terrains have emphasized the role of magmatic advection as a principle cause of metamorphism (e.g. Lux and others, 1986; DeYoreo and others, 1986; Holdaway and others, 1988; Barton and Hanson, 1989). Lux and others (1986) suggest that regional low-pressure, high-temperature metamorphism in New England resulted from heat advected from the lower crust by magmas formed in response to crustal thickening.

Geobarometry indicates that the current level of crustal exposure has been transported 13 to 16 km vertically since peak metamorphism. The current thickness of the crust beneath the Black Hills is 45 to 55 km (McCamy and Meyer, 1964; Braile et al., 1989); therefore, the crust during metamorphism may have been 60 to 70 km thick. The 25 to 35 km of crustal thickening inferred to have occurred during faulting and folding was adequate to cause partial melting of the lower crust (Thompson and England, 1984) with subsequent formation of the Harney Peak granite.

Partial melting of the lower crust in response to crustal thickening provides a reasonable mechanism for generation of the Harney Peak granite; however, it is not clear that heat advected by the Harney Peak

granite resulted in regional metamorphism. Lux and others (1986) note that regional metamorphism can only result from heat advected by magma if sills initially at ~800 °C are emplaced at distances ≤ 2 km above or below the level of crustal exposure.

Gravity data (Kleinkopf and Redden, 1975) suggest that the Harney Peak granite may extend in the subsurface eastward and perhaps northward between the Union Hill antiform and the Empire Mine fault. Gravity data also indicate that granite underlies the Bear Mountain dome (Dewitt and others, 1989); however, this may represent the older 2.5 Ga Bear Mountain granite found in the core of the dome (Figure 2.1). There does not appear to be evidence for granite at depth (e.g. Dewitt and others, 1989) for much of the study area. There is also no evidence that the granite once overlaid the current level of exposure, as there are no exposed feeder dikes.

The thermal high adjacent to the Harney Peak granite is a minor perturbation of a metamorphic field gradient that is characterized by a gradual increase in temperature from garnet grade in the north to sillimanite grade in the south. The garnet zone extends ~20 km north of the study area before dipping beneath an unconformity below Palaeozoic lithologies, and the sillimanite-zone extends ~20 km south of the study area (Figure 2.1) before dipping beneath the unconformity. The regional trend of isograds and isotherms is east-west; however, the granite locally perturbed the isotherms and isograds along its northern flank. Heat supplied by the cooling Harney Peak magma undoubtedly had a local effect on the distribution of isograds; however, local perturbation of the isograds and isotherms may partly be due to doming of isotherms and isograds during granite emplacement.

Because of the regional extent of metamorphism, it is difficult to attribute metamorphism to advection by the Harney Peak granite alone. It is possible that the Harney Peak granite resulted from the same tectonic and thermal processes that caused low-pressure, high-temperature metamorphism. The cause of regional low-pressure, high-temperature may have been an increased heat flux from the mantle (e.g. Loosveld and Etheridge, 1990).

CHAPTER III

PT-PATHS: EVIDENCE FROM ZONED GARNETS, MINERAL INCLUSIONS, AND REACTION TEXTURES

INTRODUCTION

Metamorphism in the Black Hills began during the late stages of polyphase folding; peak temperatures and the intrusion of the Harney Peak granite (1.7 Ga; Walker et al., 1986; Redden et al., 1991) occurred after folding. Isograds and isotherms generally trend east-west, and resulted from a gradual southward increase in temperature. The highest temperatures occurred adjacent to the Harney Peak granite, which represents a local anomaly on a regional metamorphic field gradient.

The causes of regional low-pressure, high-temperature metamorphism remain the subject of intense investigation (e.g. Thompson and England, 1984; Lux et al., 1986; DeYoreo, et al., 1986; Wichham and Oxburgh, 1988; Labotka and Albee, 1988; Thompson, 1989; Barton and Hanson, 1990; Loovsveld and Etheridge, 1990). Accurate determination of pressure-temperature-time (PTt) paths will provide the essential clues necessary to understand the causes of regional low-pressure, high-temperature metamorphism.

This chapter presents pressure-temperature (PT) paths experienced by Proterozoic schists from the Harney Peak area. Compositionally zoned garnets have been used extensively to interpret prograde PT paths (e.g. Tracy et al., 1976; Selverstone and Spear, 1983; St-Onge, 1987). At temperatures below ~500 to 600 °C, intracrystalline garnet diffusion rates (Lasaga et al., 1977; Tracy, 1982) are extraordinarily slow relative to garnet-growth rates; consequently, compositional zoning in low-grade garnets results from fractionation of components supplied by prograde reactions. PT paths can be estimated from reaction-zoned garnets, provided that the garnet-producing

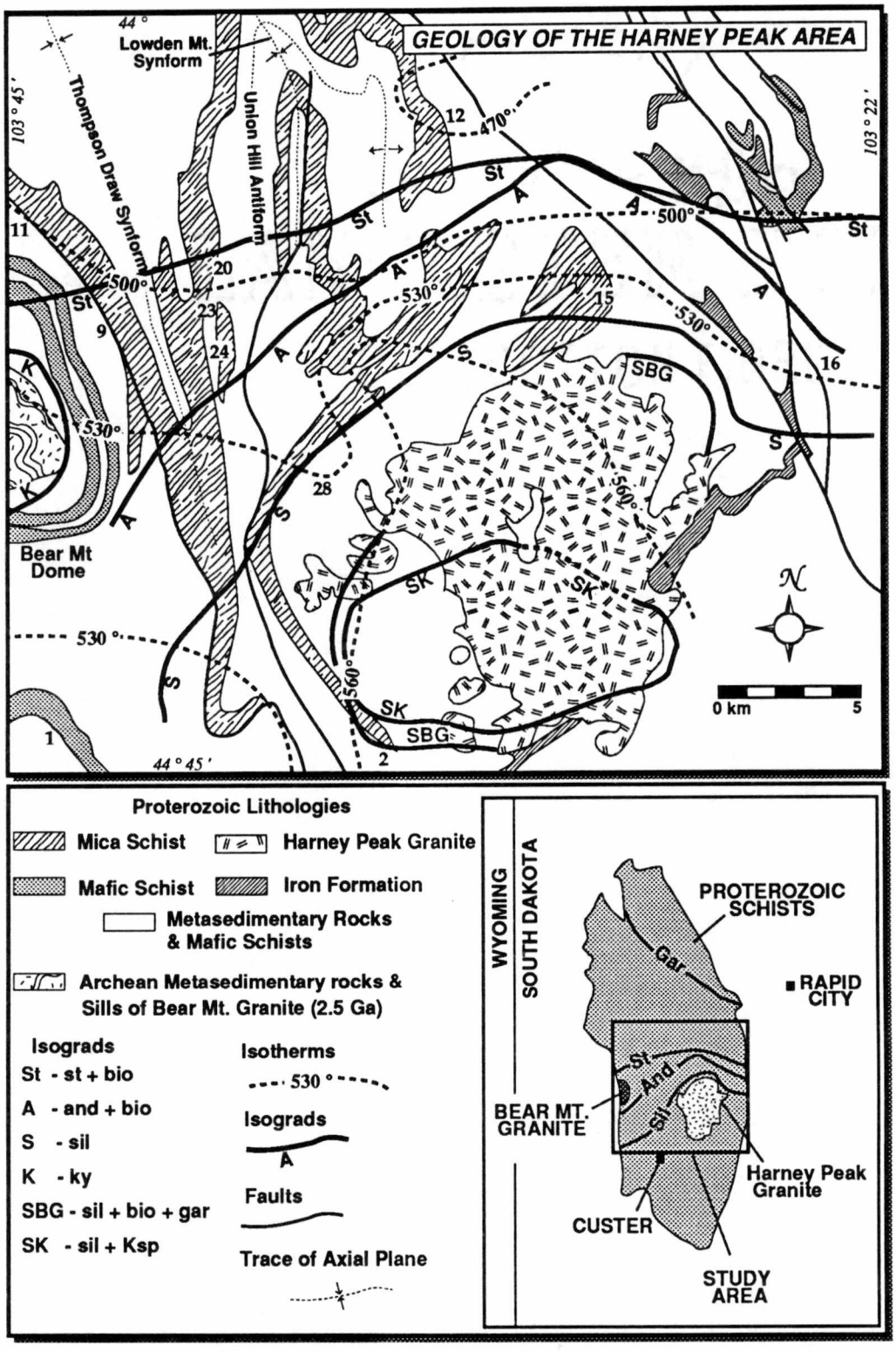
reactions are identified and the temperature and pressure dependence of the reactions governing garnet growth are known (e.g. Spear and Selverstone, 1983). Garnet zoning is commonly interpreted by the Gibbs method (Spear and Selverstone; Spear and Menard, 1989). However, the pressure and temperature dependence of the garnet-producing reactions may be expressed as a set of equilibrium constant equations, which are directly solved for pressure and temperature at garnet-core compositions. In this paper the results of both techniques are presented and compared.

PT paths combined with geothermometry, geobarometry, structural data, and geophysical data limit the choices of tectonothermal models appropriate for this terrain. Unfortunately, prograde changes in pressure and temperature with absolute time (PTt paths) are currently unknown, and only qualitative estimates of Δt can be made.

GEOLOGIC SETTING

A geologic map of the southern Black Hills, simplified from DeWitt and others (1986; 1989), is presented in Figure 3.1. Archean and Proterozoic rocks comprise a supracrustal sequence that records ~800 Ma of crustal evolution. Proterozoic deformation was characterized by the formation of east- to northeast-trending isoclinal folds (F_1), which were overturned to the northwest and subsequently refolded into upright northwest-trending folds (F_2) (Redden and Norton, 1975; Dewitt et al., 1986). Foliation developed during the formation of northwest-trending F_2 folds (Redden and Norton, 1975; Dewitt et al., 1986). In the south-central portion of the field area, doming associated with the intrusion of the Harney Peak granite greatly deformed the original interference pattern (Redden, 1963; 1968).

Figure 3.1. Geologic map of the Black Hills showing the distribution of isograds, isotherms and simplified geology (after Dewitt et al., 1988). Numbers on the map represent sample locations discussed in text. Isotherms are based on Fe/Mg partitioning between garnet and biotite (Ganguly and Saxena, 1984).


GEOLOGY OF THE HARNEY PEAK AREA
Lowden Mt. Synform
Thompson Draw Synform
Union Hill Antiform
44°
44°45'
103°45'
103°22'
Bear Mt Dome
SBG
SK
St
A
S
K
470°
500°
530°
560°
0 km
5
Proterozoic Lithologies
Mica Schist
Harney Peak Granite
Mafic Schist
Iron Formation
Metasedimentary Rocks & Mafic Schists
Archean Metasedimentary rocks & Sills of Bear Mt. Granite (2.5 Ga)
Isograds
St - st + bio
A - and + bio
S - sil
K - ky
SBG - sil + bio + gar
SK - sil + Ksp
Isotherms
530°
Isograds
Faults
Trace of Axial Plane
WYOMING
SOUTH DAKOTA
PROTEROZOIC SCHISTS
Gar
RAPID CITY
St
And
Sil
BEAR MT. GRANITE
Harney Peak Granite
CUSTER
STUDY AREA

Igneous activity included intrusion of the Bear Mountain granite at 2.5 Ga (Gosslin et al., 1988) and Harney Peak granite at 1.7 Ga. Both are interpreted to be anatectic S-type granites (Walker et al., 1986; Gosslin et al., 1988; Redden et al., 1982). The Harney Peak granite has an areal extent of ~100 km^2 and is structurally and texturally heterogeneous, comprising thousands of coarse-grained to pegmatitic dikes and sills and ubiquitous screens of metasedimentary rock (Redden et al., 1982; Duke et al., 1988). A small number of dikes and sills are deformed and metamorphosed, indicating that metamorphism and granite intrusion were partly synchronous.

The distribution of isograds (Figure 3.1) records a regional increase in temperature towards the south and a high-temperature anomaly adjacent to the Harney Peak granite. A regional southward increase in temperature is characterized by the east-trending staurolite, andalusite, and sillimanite isograds. A thermal-high adjacent to the Harney Peak granite resulted in the breakdown of staurolite + muscovite and muscovite + quartz. The distribution of mineral assemblages indicates a westward-, and perhaps southward-deepening exposure of the metamorphic complex. Higher pressures are indicated by kyanite in the Bear Mountain dome, and by increased resolution of the staurolite and andalusite isograds towards the west (Helms and Labotka, 1991). Redden (1963) also identified kyanite outside the study area, south of sample location 1 (Figure 3.1).

Fe/Mg partitioning between garnet and biotite (Ganguly and Saxena, 1984) indicates a temperature increase from ~460-500 °C in the garnet zone to ~530-555 °C in the sillimanite zone on the north flank of the Harney Peak granite (Helms and Labotka, 1991). Slightly higher temperatures (~563-585

°C) are recorded along the south flank of the granite in the sillimanite + garnet + biotite and sillimanite + K-feldspar zones. Isotherms based on garnet-biotite thermometry (Figure 3.1) are generally consistent with the distribution of isograds.

Geobarometry based on garnet + plagioclase + Al_2SiO_5 + quartz (Koziol and Newton, 1988; Holdaway, 1971) and garnet + plagioclase + biotite + quartz (Ghent and Stout, 1981) equilibria indicate an average pressure of 3.0 kbar and a range of 4.4 to 2.5 kbar (Helms and Labotka, 1991). The highest pressure was measured in the kyanite zone at the Bear Mountain dome and in the sillimanite zone adjacent to the Harney Peak Granite. Except in the Bear Mountain area, the variation in estimated pressures is commonly within the range of uncertainty of the calibration (~ ± 0.75 kbar, Helms and Labotka, 1991).

ANALYTICAL METHODS

Mineral compositions were measured with a wavelength-dispersive Cameca SX50 electron microprobe using synthetic and natural standards and operating at an accelerating voltage of 15 kV. A beam current of 0.015 μA and beam diameter ~10 μm were used to analyze micas and feldspars. All other phases were analyzed with a beam current of 0.03 μA and a beam diameter of ~5 μm. Analyses were reduced in real time utilizing ZAF corrections.

Silicates were normalized on the basis of the appropriate number of oxygens. Holdaway et al. (1988) suggest that staurolite contains 3 hydrogen atoms for each unit cell. For consistency with the thermodynamic data sets used in this study (Berman et al., 1988; Holland and Powell, 1990), staurolite compositions were normalized to 23 oxygens consistent with a half unit cell of

22 oxygens and 2 $(OH)^-$ groups (e.g. Griffen and Ribbe, 1973; Pigage and Greenwood, 1982). Mineral analyses are presented in the Appendix 3.

CALCULATION OF PT PATHS

In an equilibrium mineral assemblage composed of n independent system components and m phases, where each phase consists of k mineral or fluid components, there are $(m \cdot k)$-n independent continuous reactions possible among the mineral and fluid components (Thompson, 1982). The system components are the minimum number of components necessary and sufficient to describe the compositions of the minerals and fluid. The set of j continuous reactions govern the composition and mode of the coexisting minerals. Dependence of the continuous reactions on temperature, pressure, mineral composition, and fluid composition can be expressed as a set of equilibrium constant (K_{Eq}) equations of the form

$$0 = \Delta G(1, 298) + \int_{298}^{T} \Delta C_p dT - \int_{298}^{T} \Delta C_p d\ln T + P\Delta V_s + \pi \nu_i RT\ln(\gamma_i x_i)_s + \nu_i RT\ln(f_{H_2O})_f,$$

where ν_i is the stoichiometric coefficient of the mineral component in the continuous reaction, x_i is the mole fraction of the component in a particular mineral, and γ_i is the activity coeffecient of the mineral component. The subscripts s and f indicate a solid and a fluid, respectively. The algebraic difference between the number of independent K_{eq}-equations and the total number of independent thermodynamic variable (e.g. T, P, x_i, etc.) is equal to the thermodynamic variance of the system.

A set of equations that state the relationship between the dependent

and independent compositional variables is implicitly included in the set of K_{Eq} equations. A mineral or fluid composed of k components contains k-1 independent components. For example, pelitic garnets are commonly composed of almandine, pyrope, spessartine, and grossular components (Table 3.1); because the sum of the mole fractions of the four components is 1, any mole fraction can be expressed in terms of the other three. In an assemblage with a thermodynamic variance of 3 or less, garnet composition provides the necessary number of independent compositional variables to solve for pressure, temperature, and the mole fractions of all the components in the coexisting phases. Therefore, interior garnet compositions can be used to estimate pressure and temperature, if the garnet grew in an assemblage with a thermodynamic variance ≤ 3. The array of pressures and temperatures estimated with a zoned garnet provides a portion of the PT path.

PT paths may also be calculated from zoned garnets using the Gibbs, or differential method. The differential method and its application to zoned garnets is throughly developed by Spear et al. (1982), Spear and Selverstone (1983), Spear (1986), Spear (1989), and Spear and Menard (1989). Estimation of a PT path from a zoned mineral using the differential method requires the temperature, pressure, and matrix mineral compositions that are consistent with the equilibrium conditions at the garnet rim (i.e. the final garnet composition). Therefore, a PT path can be estimated with the differential method only if the garnet interior was in equilibrium with the final matrix assemblage. In contrast, the only information needed to determine pressure and temperature from an interior garnet composition and a set of independent K_{Eq} equations, are the mineral assemblage in equilibrium with

Table 3.1. Abbreviations and Compositions of Mineral Components.

GARNET	
Almandine (Alm)	$Fe_3Al_2Si_3O_{12}$
Pyrope (Pyr)	$Mg_3Al_2Si_3O_{12}$
Spessartine (Sps)	$Mn_3Al_2Si_3O_{12}$
Grossular (Gro)	$Ca_3Al_2Si_3O_{12}$
STAUROLITE	
Staurolite (St)	$Fe_2Al_9Si_{3.75}O_{22}(OH)_2$
Mg-Staurolite (Mg-St)	$Mg_2Al_9Si_{3.75}O_{22}(OH)_2$
Mn-Staurolite (Mn-St)	$Mn_2Al_9Si_{3.75}O_{22}(OH)_2$
BIOTITE	
Annite (Ann)	$KFe_3AlSi_3O_{10}(OH)_2$
Phlogopite (Phl)	$KMg_3AlSi_3O_{10}(OH)_2$
Siderophylite (Sid)	$KFe_2Al_3Si_2O_{10}(OH)_2$
Eastonite (East)	$KMg_2Al_3Si_2O_{10}(OH)_2$
Ti-Eastonite (TiTs-Ea)	$KMg_2TiAl_3SiO_{10}(OH)_2$
CHLORITE	
Daphnite (Dap)	$Fe_5Al_2Si_3O_{10}(OH)_8$
Clinochlore (Clin)	$Mg_5Al_2Si_3O_{10}(OH)_8$
Amesite (Ams)	$Mg_4Al_4Si_2O_{10}(OH)_8$
MUSCOVITE	
Muscovite (Mu)	$KAl_3Si_3O_{10}(OH)_2$
Paragonite (Pa)	$NaAl_3Si_3O_{10}(OH)_2$
Mg-Phengite (Mg-Phen)	$KAl_2Mg_{0.5}Si_{3.5}O_{10}(OH)_2$
Ti-Muscovite (TiTs-Mu)	$KAl_3TiSi_2O_{10}(OH)_2$
PLAGIOCLASE	
Albite (Ab)	$NaAlSi_3O_8$
Anorthite (An)	$CaAl_2Si_2O_8$
Andalusite (And)	Al_2SiO_5
Sillimanite (Sil)	Al_2SiO_5
Quartz (Qtz)	SiO_2

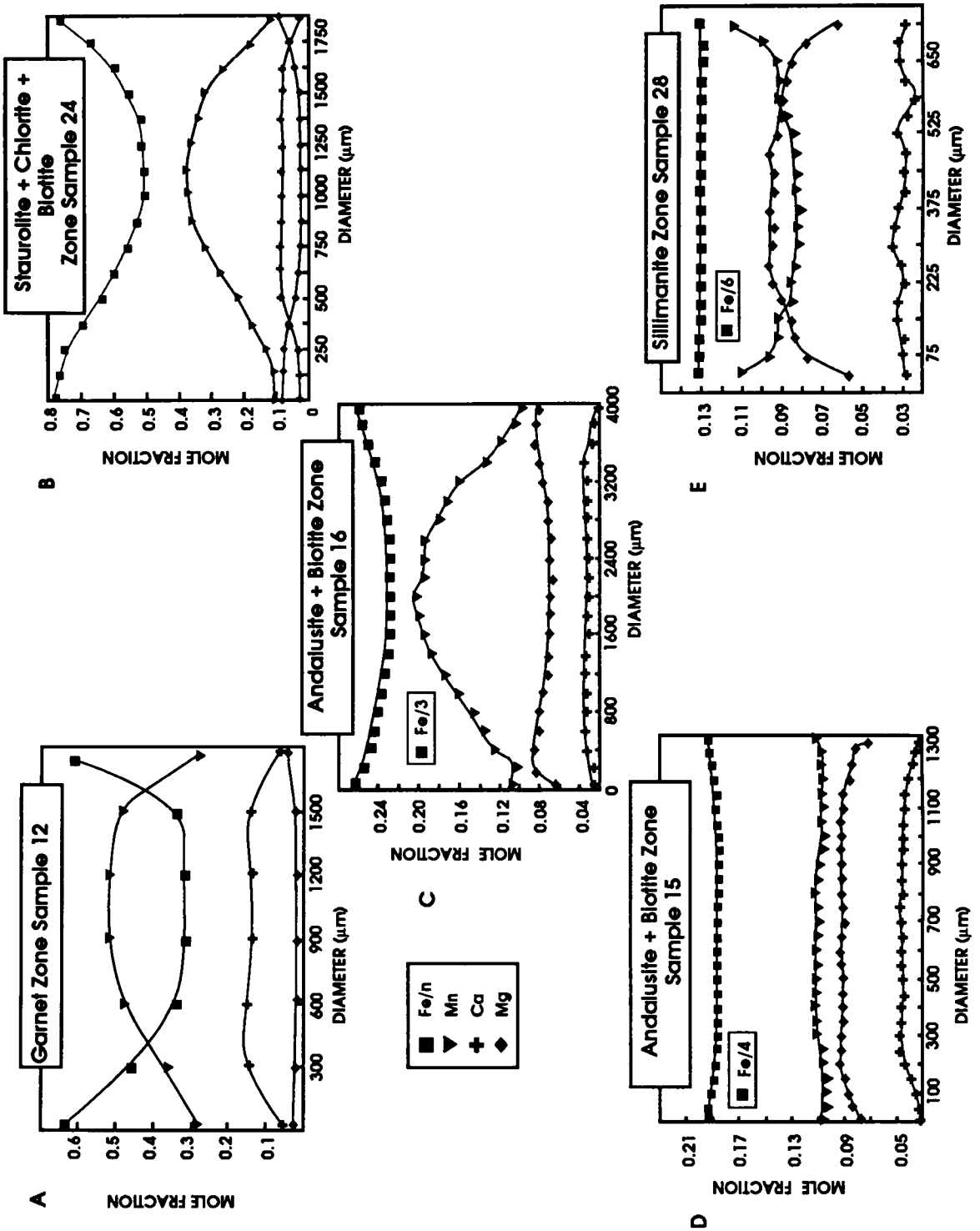
the garnet core and the appropriate data to estimate the K_{Eq} equations.

The differential and integrated methods should produce identical results. The differential method, however, requires only entropy and volume data. Spear and Selverstone (1983) state that entropy and volume data have less associated error than enthalpies of formation required for K_{eq} equations. Although preliminary, results presented here indicate that very little difference exists between PT paths estimated using the differential and integrated methods. Therefore, these two methods used together may allow a greater amount of flexibility for modeling reaction zoned garnets. The program GIBBS (Spear and Menard, 1989), which uses the thermodynamic data set of Berman (1988), is used to calculate PT paths by the differential method.

GARNET ZONING

Garnets from the Black Hills exhibit a variety of compositional zonation patterns. Garnets from the garnet zone and staurolite zone (Figure 3.2a and 3.2b) are strongly zoned with respect to Fe and Mn. The concentrations of Fe and Mn are inversely correlated across zoning profiles, and Mn is depleted from core to rim. Ca in garnets of almost all grades decreases abruptly at the rim, but commonly exhibits negligible variation in the interior. At low-grades, Mg appears to increase towards the rim; however, the Fe/Mg increases from core to rim. Andalusite + biotite-grade garnets collected at distances > 1.5 to 2.0 km from the granite contact exhibit compositional zoning patterns similar to those observed in lower-grade rocks (Figure 3.2c); however, the rim-to-core variation is more subdued.

Figure 3.2. Representative compositional zoning profiles of garnets from (A) the garnet zone, (B) the staurolite + biotite + chlorite zone, (C) and (D) from the andalusite + biotite zone, and (E) the sillimanite zone. Symbols are as follows: squares-X_{Fe}, diamonds - X_{Mn}, triangles - X_{Mg} crosses - X_{Ca}. Note that X_{Fe} has been normalized in Figures (C), (D), and (E) to graphically enhance variations in the other components.


Garnet Zone Sample 12
Staurolite + Chlorite + Biotite Zone Sample 24
Andalusite + Biotite Zone Sample 16
Andalusite + Biotite Zone Sample 15
Sillimanite Zone Sample 28
Fe/n
Mn
Ca
Mg
Fe/3
Fe/4
Fe/6
MOLE FRACTION
DIAMETER (μm)
A
B
C
D
E

Garnets from the andalusite + biotite and sillimanite zones adjacent to the Harney Peak Granite are nearly homogeneous (Figure 3.2d-e); however, Fe and Mn increase slightly towards the rim, and Mg and Ca decrease towards the rim (Figure 3.2e). Many of the garnets in the sillimanite zone were partially resorbed, resulting in depletion of Mg and enrichment in Mn and Fe at the rim. Because of the effects of homogenization and resorption in sillimanite-zone rocks, only zoned garnets from the garnet, staurolite, and andalusite zones are used to estimate quantitatively PT paths.

THE COMPOSITIONAL SYSTEM AND MINERAL COMPONENTS

The major rock-forming minerals that compose pelitic schists can be described by the eleven oxides: SiO_2, TiO_2, Al_2O_3, MgO, FeO, MnO, ZnO, CaO, Na_2O, K_2O, and H_2O. It is currently impossible to deal with this compositional system because very few experimental and thermodynamic data exist for staurolite components, for the tschermakitic end-members of chlorite and mica, and for the Zn-, Ti-, and Mn-end member components. It is possible to choose simpler compositional subsystems that preserve the thermodynamic variance of the system. For example, if both the system component TiO_2 and the phase ilmenite are excluded, the variance of the system is unaffected. Ignoring TiO_2, however, affects the system of equations relating independent and dependent mineral components. For example, biotite contains significant ^{VI}Ti, and by excluding TiO_2 from consideration, a variable is lost from the equation $^{VI}Mg = 3 - {}^{VI}[Fe + Ti + Al + \square]_{Biotite}$. If the compositional system is simplified by dropping TiO_2, other relationships, such as the variation of Ti with Mg in biotite, must be included in the system

of K_{Eq} equations.

Several simplifying assumptions can be made about the mineral formulas that reduce the number of system components and the number of K_{Eq} equations that must be solved simultaneously. The "extra" octahedral components from the layer silicates can be assumed to be approximately constant. The sum of octahedral components (i.e. ^{VI}[Ti + Al + □]) in biotite other than Fe and Mg is normally distributed about the average value of 2.35 moles (Figure 3.3a). The amount of interlayer Na in biotite is also small (<0.07 mole percent), and the concentration of interlayer K is approximately constant (0.89 moles). The concentration of Fe + Mg in chlorite is normally distributed about the average value of 4.58 moles (Figure 3.3b). The variation in the concentration of ^{VI}Al in muscovite is not normally distributed (Figure 3.3c); therefore, the average value has no significance. However, there is no systematic variation in ^{VI}Al with metamorphic grade (Helms and Labotka, 1991), and the variation is probably a function of fO_2, as total Fe and Al (weight percentage) are negatively correlated. It is assumed that ^{VI}Al is fixed at 1.9 moles. Interlayer K in muscovite varies between 0.72 and 0.92 moles; however, in schists lacking K-feldspar, K is restricted to values between 0.72 and 0.86 moles. The amount of interlayer site-vacancy in muscovite is quite small (~ 0.03 moles) and is assumed to be constant.

As an approximation, the Al- and Ti-tschermakitic components in the layer silicates, the Na-biotite component, and the interlayer vacancy component in muscovite are assumed constant. Plagioclase from the Black Hills (Helms and Labotka, 1991) is almost completely composed of anorthite and albite components, so $X_{An}^{Pl} \approx (1\text{-}X_{Ab}^{Pl})$. The concentration of Mn-phase components in layer silicates is also very small (Helms and Labotka, 1991)

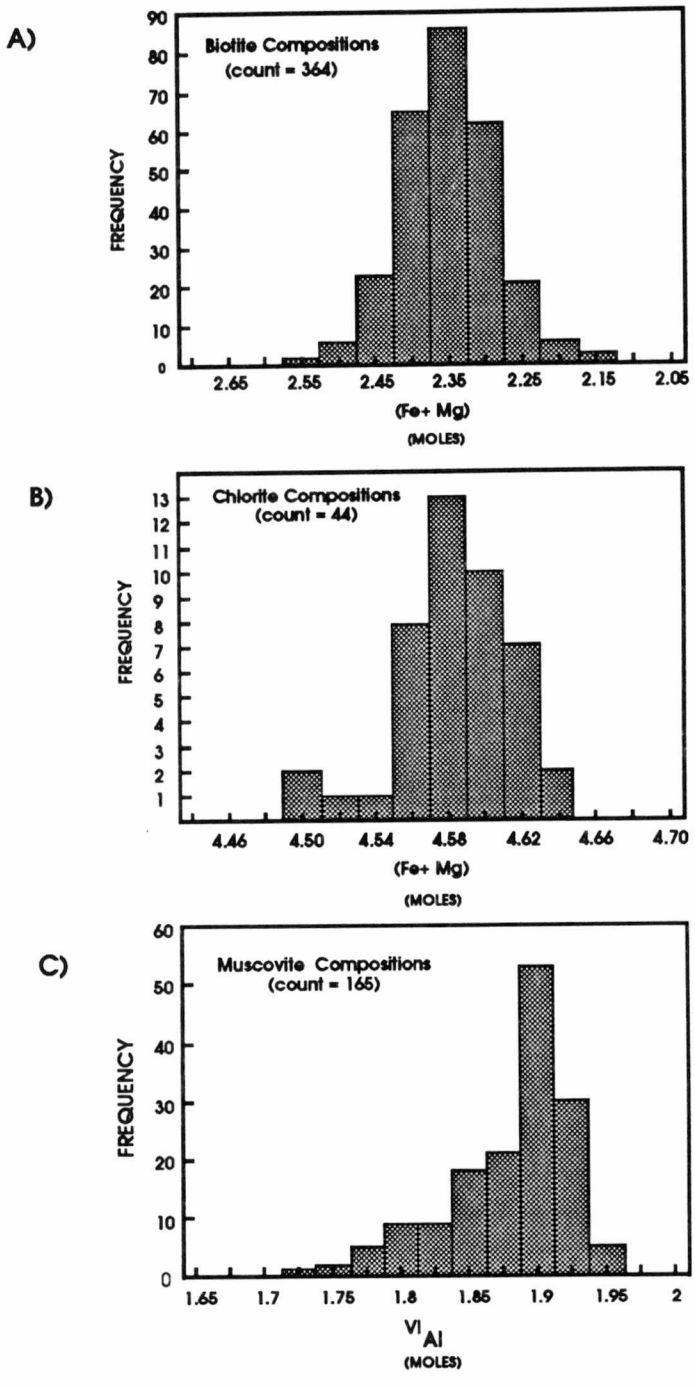


Figure 3.3 A) Frequency distribution of moles ^{VI}[Fe + Mg] in biotite. B) Frequency distribution of moles(Fe + Mg) in chlorite. C) Frequency distribution of moles ^{VI}Al in muscovite.

and is excluded from consideration. These approximations significantly reduce the number of mineral components, and consequently the number of K_{Eq} equations that are solved for pressure and temperature. Sets of continuous reactions appropriate for the simplified system SiO_2, Al_2O_3, MgO, FeO, CaO, Na_2O, K_2O, and H_2O were determined for the garnet zone, the staurolite zone, and the andalusite zone assemblages (Table 3.2). The net-transfer reactions (Table 3.2) control the mineral mode, whereas the exchange reactions determine the distribution of Fe and Mg between the coexisting phases, and also conserve the modal abundance of the coexisting phases (Thompson, 1982).

K_{Eq}-EQUATION SETS

The dependence of the continuous reactions (Table 3.2) on temperature, pressure, mineral composition, and fluid composition is expressed as sets of K_{Eq} equations in Tables 3.3 and 3.4. K_{Eq} equations in this study are taken directly from experimental data whenever possible (i.e. standard geothermometers and geobarometers). Where experimental data are lacking, K_{Eq} equations have been estimated with the thermodynamic data set of Holland and Powell (1985; 1990). The choice of the Holland and Powell data set was arbitrary, and equilibria estimated with the Berman (1988) data set reveal only small differences. The source for each of the K_{Eq} equations is listed in Tables 3.3 and 3.4. Staurolite was excluded from sets of K_{Eq} equations because of discrepancies between experimental (Richardson, 1968; Ganguly, 1972; Dutrow, 1989) and field evidence for staurolite stability (Ferry, 1980; Pigage and Greenwood, 1982; Lang and Rice,

Table 3.2. Reaction Sets for the Garnet Zone, Staurolite Zone, and Andalusite ZoneAssemblages

GARNET ZONE

Net-Transfer Reactions

(1) Pyr + Gro + Mu = 3 An + Phl

(2) 21 An + 12 Ab + 3 Clin = 5 Pyr + 7 Gro + 12 Pa + 15 Qtz

(3) 3 Clin + Mu + 3 Qtz = 4 Pyr + Phl + 12 H_2O

Exchange Reactions

(4) Pyr + Ann = Alm + Phl

(5) 5 Pyr + 3 Dap = 5 Alm + 3 Clin

STAUROLITE ZONE

Net-Transfer Reactions

(1) Pyr + Gro + Mu = 3 An + Phl

(2) 21 An + 12 Ab + 3 Clin = 5 Pyr + 7 Gro + 12 Pa + 15 Qtz

(3) 3 Clin + Mu + 3 Qtz = 4 Pyr + Phl + 12 H_2O

(6) 36 Mg-St + 34 Phl + 70 Ab + 39 Qtz = 58 Pyr + 70 Pa + 34 Mu

Exchange Reactions

(4) Pyr + Ann = Alm + Phl

(5) 5 Pyr + 3 Dap = 5 Alm + 3 Clin

(7) 2 Pyr + 3 St = 2 Alm + 3 Mg-St

ANDALUSITE ZONE

Net-Transfer Reactions

(1) Pyr + Gro + Mu = 3 An + Phl

(8) 3 An = Gro + And + 2 Qtz

(9) Pa + Qtz = And + Ab + H_2O

Exchange Reactions

(4) Pyr + Ann = Alm + Phl

Table 3.3. Equilibrium Constant Equations Used to Solve for Pressure and Temperature at Garnet Core Compositions Buffered by the Garnet-Zone Assemblage.

Independent Variables

$X_{Mg}^{Gar}, X_{Ca}^{Gar}, X_{Mg}^{Bi}, X_{Mg}^{Chl}, X_{K}^{Mu}, X_{Ca}^{Pl}, T, P, a_{H_2O}$

Dependent Variables

$X_{Na}^{Pl} = (1 - X_{Ca}^{Pl})$;

$X_{Na}^{Mu} = (0.97 - X_{K}^{Mu})$

$X_{Fe}^{Bi} = (1 - X_{Mg}^{Bi})$ and $X_{Mg}^{Bi} = Mg^{Bi}/(Fe^{Bi} + Mg^{Bi} \approx 2.4)$

$X_{Fe}^{Chl} = (1 - X_{Mg}^{Chl})$ and $X_{Mg}^{Chl} = Fe^{Chl}/(Fe^{Chl} + Mg^{Chl} \approx 4.6)$

Equilibrium Constant Equations:

(1) $P\ (bar) = (19657 + 96.598T + RT\ln K_{eq(1)})/7.3$

(2) $P\ (bar) = (-19616 + 95.618T + RT\ln K_{eq(2)})/4.9$

(3) $f_{H_2O}\ (bar) = \exp\{-(1106554 - 2051.6T + 0.2398T^2 - 23.99P + RT\ln K_{eq(3)})/12RT\}$

(4) $X_{Mg}^{Bi} = 1/[1 + (1 - X_{Mg}^{Gar})\exp\{(12454 - 4.662T + 0.057P)/(-3RT)\}/X_{Mg}^{Gar}]$

(5) $X_{Mg}^{Chl} = 1/[1 + (1 - X_{Mg}^{Chl})\exp\{(51906 - 7.541T + 0.438P)/-15RT)\}/X_{Mg}^{Chl}]$

Equilibrium Constants

$K_{eq(1)} = [(X_{Mg}^{Gar})^3 (X_{Ca}^{Gar})^3 X_{K}^{Mu} \gamma_{K}^{Mu}]/[(X_{Ca}^{Pl} \gamma_{Ca}^{Pl})^3 (X_{Mg}^{Bi})^3 X_{K}^{Bi}]$

$K_{eq(2)} = [(X_{Ca}^{Gar})^{1.75} (X_{Mg}^{Gar})^{1.25} \gamma_{Na}^{Mu} X_{Na}^{Mu}]/[(X_{Ca}^{Pl} \gamma_{Ca}^{Pl})^{1.75} X_{Na}^{Pl} (X_{Mg}^{Chl})^{1.25}]$

$K_{eq(3)} = [(X_{Mg}^{Bi})^3 X_{K}^{Bi} (X_{Mg}^{Gar})^{12}]/[X_{K}^{Mu} \gamma_{K}^{Mu} (X_{Mg}^{Chl})^8]$

The numbers assigned to the K_{eq} eqautions corresponds to the appropriate reaction number in Table 3.4. Equations (1)-(3) were calculated from Holland and Powell (1990). Equation (4) is from Ferry and Spear (1978) and equation (5) is from Dickenson and Hewitt (1986).

Table 3.4. Equilibrium Constant Equations Used to Solve for Pressure and Temperature at Garnet Core Compositions Buffered by the Andalusite + Biotite Zone Assemblage.

Independent Variables

$X^{Gar}_{Mg}, X^{Gar}_{Ca}, X^{Bi}_{Mg}, X^{Mu}_{K}, X^{Pl}_{Ca}, T, P, a_{H_2O}$

Dependent Variables

$X^{Pl}_{Na} = (1- X^{Pl}_{Ca})$;

$X^{Mu}_{K} = (0.97-X^{Mu}_{Na})$

$X^{Bi}_{Fe} = (1- X^{Bi}_{Mg})$ and $X^{Bi}_{Mg} = Mg^{Bi}/(Fe^{Bi} + Mg^{Bi} \approx 2.4)$

Equilibrium Constant Equations:

(1) $P\ (bar) = (19657 + 96.498\ T + RT\ln K_{eq(1)})/7.3$

(8) $P\ (bar) = (2725.34 - 123.58T - 0.003997T^2 - 3RT\ln K_{eq(8)})/-4.86$

(9) $f_{H_2O}\ (bar) = \exp\{(-84789.99 + 161.79T + 0.332\ P - RT\ln K_{eq(9)})/RT\}$

(4) $X^{Bi}_{Mg} = [\ 1+ (1- X^{Gar}_{Mg})\exp\{(12454-4.662T + 0.057P)/(-3RT)\}/X^{Gar}_{Mg}\ ]^{-1}$

Equilibrium Constants

$K_{eq(1)} = [(X^{Gar}_{Mg})^3(X^{Gar}_{Ca})^3 X^{Mu}_{K} \gamma^{Mu}_{K}]/[(X^{Pl}_{Ca}\gamma^{Pl}_{Ca})^3(X^{Bi}_{Mg})^3 X^{Bi}_{K}]$

$K_{eq(8)} = (X^{Gar}_{Ca})/(X^{Pl}_{Ca}\gamma^{Pl}_{Ca})$

$K_{eq(9)} = \gamma^{Mu}_{Na} X^{Mu}_{Na}/X^{Pl}_{Na}$

Equation (1) was calculated from Holland and Powell (1990). Equation (8) is from Koziol and Newton (1988) and Holdaway (1971); equation (4) is from Chatterjee (1971); equation (4) is from Ferry and Spear (1978).

1985; Holdaway et al., 1988). Because staurolite has not been considered, there is no need to express the staurolite zone reaction set as K_{Eq}-equations. The sets of equations, therefore, model changes in mineral composition with pressure, temperature and a_{H_2O}, in the simplified garnet-zone assemblage (Table 3.3)

garnet + biotite + chlorite + muscovite + plagioclase + quartz + H_2O,

and the andalusite zone assemblage (Table 3.4)

garnet + biotite + andalusite + muscovite + plagioclase + quartz + H_2O.

The thermodynamic variance of most pelitic assemblages from the Black Hills is greater than 3. The set of 5 equations in Table 3.3 contains 9 unknowns and the set of 4 equations in Table 3.4 contains 8 unknowns. Solving either set of equations for pressure and temperature requires that four variables be held constant. Garnet composition in the Mn-absent system provides 2 independent variables. The remaining variables can be provided by multicomponent mineral inclusions. Unfortunately, mineral inclusions are not common. Pressures and temperatures were therefore estimated within fixed ranges of muscovite composition and a_{H_2O}. The mole fraction of K in the interlayer-site of muscovite is restricted to values between 0.72 and 0.86 moles in pelitic schists lacking K-feldspar. Therefore, the system of K_{Eq} equations is solved for pressure and temperature at the extremes of these compositional limits. The a_{H_2O} is also assumed to be between 0.7 and 1.0, consistent with high values (0.8-1.0) measured in Helms and Labotka (1991).

Equations that govern the activities of mineral components in solid solution and the fugacity of H_2O at temperature and pressure are included in

the system of equations listed in Tables 3.3 and 3.4. The fugacity of H_2O was estimated using the modified Redlich-Kwong equation of Bowers and Helgeson (1983). The activities of plagioclase and muscovite components were estimated with the expression of Saxena and Ribbe (1972) and Chatterjee and Froese (1975), respectively. All other solid solutions were assumed to be ideal.

The system of non-linear equations in both Tables 3.3 and 3.4 were solved numerically using Newton's method. The accuracy of the equations was tested by solving the system of equations in Table 3.4 with measured garnet rim and matrix muscovite compositions. Calculated values of X_{Mg}^{Bi}, X_{Mg}^{Chl}, and X_{An}^{Pl} are compared with measured values in Table 3.5. Estimated mineral compositions are in moderately good agreement with measured compositions, indicating that the set of equations provides a reasonable means of estimating temperature and pressure at garnet-core compositions where X_{Mg}^{Bi}, X_{Mg}^{Chl}, X_{An}^{Pl}, and X_{K}^{Mu} are unknown.

THE GARNET AND STAUROLITE + CHLORITE + BIOTITE ZONES

Garnet-zone pelitic schists are characterized by the assemblage

garnet + biotite + chlorite + muscovite + plagioclase + quartz (A).

The first appearance of garnet results from the continuous reaction

3 clinochlore + muscovite + 3 quartz =

4 pyrope + phlogopite + 12 H_2O (3).

Chlorite was never completely consumed at garnet-grade conditions; therefore, assemblage (A) buffered garnet composition during the entire period of garnet growth. Garnet in the assemblage garnet + biotite + chlorite

Table 3.5. T,P, and Mineral Compositions Calculated at Measured Garnet Rim and Muscovite Values, with the System of Equations Presented in Table 3.3.

	Input Data						
Sample:	Xgr	Xpy	Xal	Xmu	Xan	Xphl	Xclin
11	0.041	0.089	0.636	0.758	0.207	0.442	0.523
					0.200	0.409	0.506
					3.4 %	7.4 %	3.2 %
20	0.029	0.090	0.696	0.760	0.183	0.422	0.502
					0.180	0.390	0.484
					1.6 %	7.5 %	3.6 %
24	0.032	0.087	0.787	0.729	0.170	0.374	0.455
					0.184	0.364	0.452
					8.2 %	2.8 %	0.6 %
8	0.047	0.116	0.567	0.781	0.229	0.493	0.587
					0.240	0.469	0.581
					4.8 %	4.9 %	1.0 %
23	0.031	0.086	0.796	0.77	0.181	0.374	0.448
					0.198	0.349	0.433
					9.4 %	6.7 %	3.3 %

Note: The first row of data for each sample consists of measured mineral compositions. The second row of data consists of values of X_{An}, X_{Phl}, and X_{Clin} ,estimated with the equation set in Table 3.4 and the input data listed above. The precentages in the third row for each respective sample = 100 x (measured value - calculated value)/ measured value.

+ staurolite + plagioclase + muscovite + quartz (B)

also grew entirely in the presence of assemblage (A), as no phase is completely removed at the staurolite isograd. A system of K_{Eq} equations appropriate for assemblage (B) was not used, as it is uncertain when staurolite nucleated in relationship to the zoning profile and because garnet was likely to have been consumed to produce staurolite by the reaction

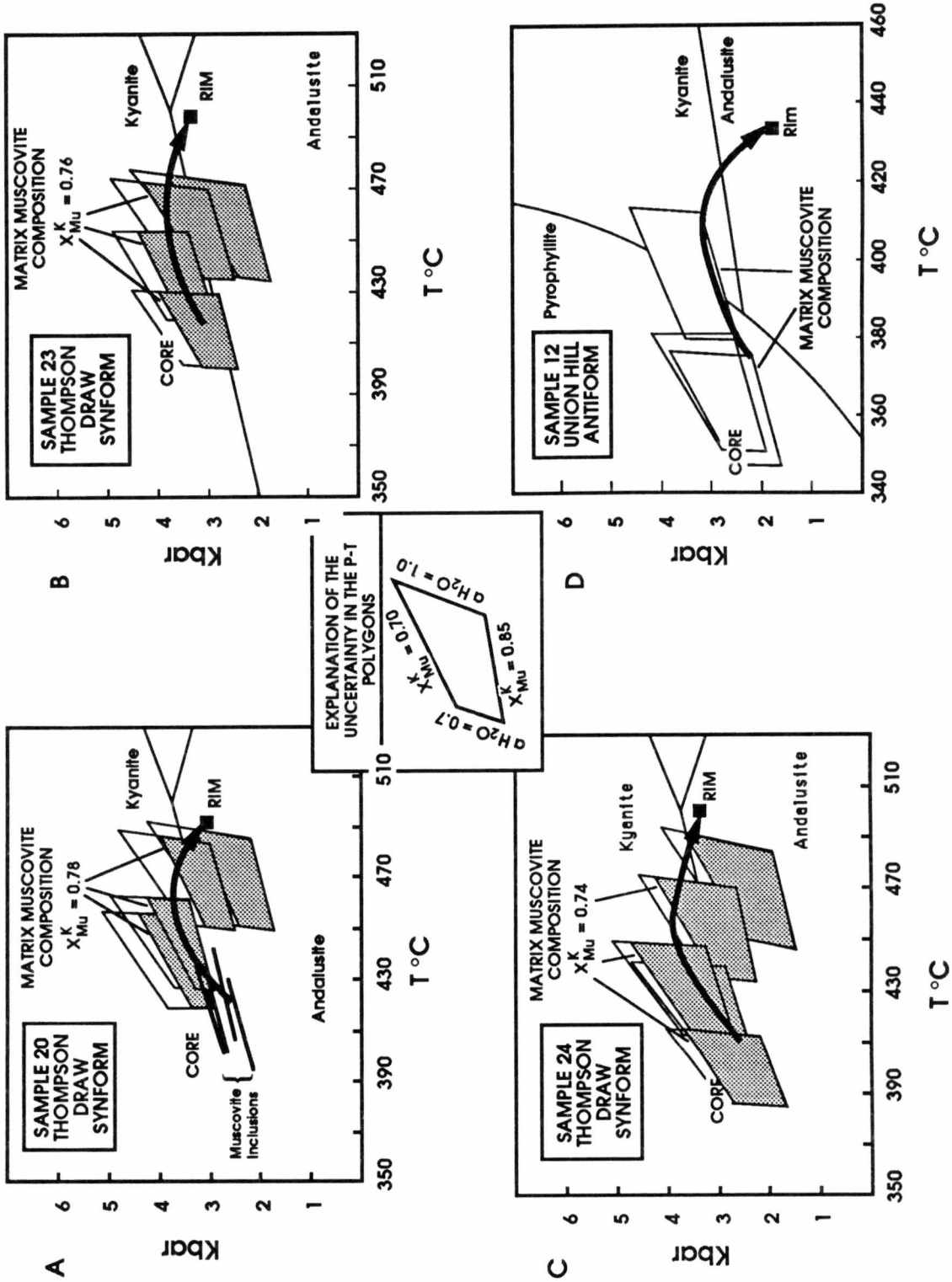
garnet + chlorite + muscovite = staurolite + biotite + H_2O (10)

at the staurolite isograd (Helms and Labotka, 1991).

The system of K_{Eq} in Table 3.3 is used to model garnet growth in the presence of assemblages (A) and (B). PT paths plotted on Figure 3.4 are based on staurolite zone samples from the Thompson Draw synform and on a garnet zone from the Union Hill antiform. P-T polygons reflect the range in muscovite composition and a_{H_2O}. The upper and lower face of the polygons are isopleths of $X_K^{Mu} = 0.7$ and $X_K^{Mu} = 0.85$, respectively. The near-vertical faces represent constant a_{H_2O}; on the high temperature face $a_{H_2O} = 1$, and on the low temperature face $a_{H_2O} = 0.7$. Because a_{H_2O} may have been lower, PT paths record a minimum temperature increases of 60 °C to 100 °C. Heating was initially accompanied by burial and followed by small amounts of exhumation. Fortunately, uncertainty in a_{H_2O} does not result in large uncertainties in pressure.

Although the array of P-T polygons for any particular sample encompasses significant uncertainty, the approximate behavior of muscovite composition in response to garnet growth in assemblages (A) and (B) is predictable. Reaction (3), the linear combination of reactions (3) and (4)

Figure 3.4. PTt paths calculated for garnet-core compositions for samples 23 (A), 12 (B), 24 (C), and 20 (D). The polygons reflect uncertainty in muscovite composition and a_{H_2O}; the vertical faces reflect constant a_{H_2O} at 1.0 and 0.7, and the sub-horizontal faces are isopleths of constant muscovite composition at X_K^{Mu} = 0.7 and 0.85. The shaded regions in the uncertainty polygons are bounded by X_K^{Mu} = 0.85 and X_K^{Mu}= the composition of matrix muscovite.


A
B
C
D
Kbar
T °C
SAMPLE 20 THOMPSON DRAW SYNFORM
SAMPLE 23 THOMPSON DRAW SYNFORM
SAMPLE 24 THOMPSON DRAW SYNFORM
SAMPLE 12 UNION HILL ANTIFORM
MATRIX MUSCOVITE COMPOSITION
X^K_{Mu} = 0.78
X^K_{Mu} = 0.76
X^K_{Mu} = 0.74
CORE
RIM
Rim
Muscovite Inclusions
Kyanite
Andalusite
Pyrophyllite
EXPLANATION OF THE UNCERTAINTY IN THE P-T POLYGONS
a_{H_2O} = 1.0
a_{H_2O} = 0.7
X^K_{Mu} = 0.70
X^K_{Mu} = 0.85

(the Fe-end member), and a Mn equivalent of reaction (3), are the major producers of garnet component in assemblage (A). Because these reactions consume muscovite component, it is likely to become progressively enriched in paragonite component with garnet growth. PT paths will therefore tend to pass along paths that reflect increasing paragonite component. When the reaction

garnet + chlorite + muscovite = staurolite + biotite + quartz + H2O (10)

is encountered at the staurolite isograd (Helms and Labotka, 1991), significant amounts of muscovite component are used to produce staurolite + biotite, and the composition of muscovite should become further enriched in paragonite component. The preceding predictions are supported by muscovite inclusions found in a garnets from sample 23. Muscovite inclusions range in composition between X_K^{Mu} = 0.81-0.86, whereas muscovite in the matrix has X_K^{Mu} = 0.78. The composition of muscovite inclusions remains rich in muscovite component, even close to the rim. Sample 23 is composed of assemblage B; therefore, enrichment in paragonite likely occurred at the staurolite isograd, where garnet was consumed.

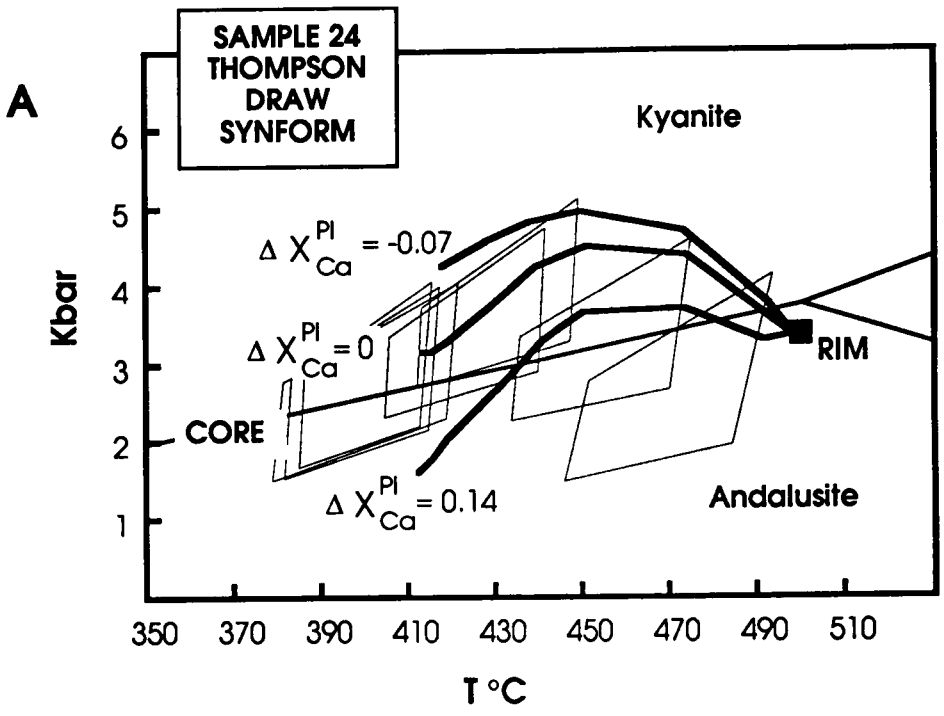
The initial muscovite composition that coexisted with the garnet core is unknown for garnet samples lacking muscovite inclusions; however, muscovite is unlikely to become enriched in paragonite component towards the core of the garnet. PT polygons in Figure 3.4 have been shaded within the region bounded by the isopleths of muscovite compositions X_K^{Mu} = 0.85 and the value of X_K^{Mu} measured in the matrix. PT paths (Figure 3.4) were constructed such that paragonite increases from core to rim. Following the

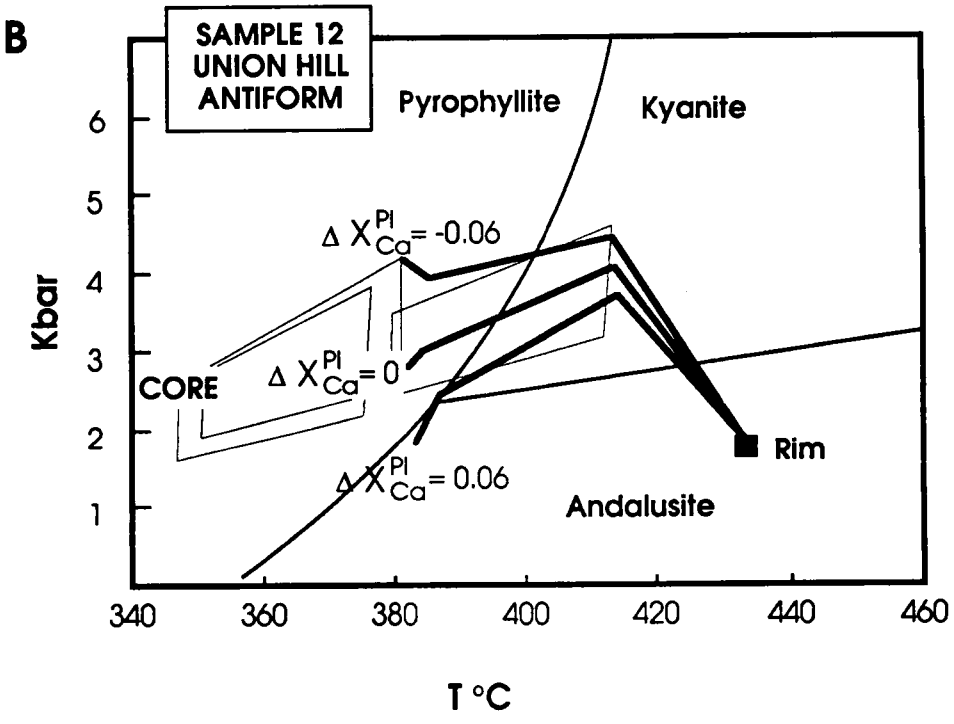
above constraints, the PT paths in Figure 3.4 indicate heating with an initial period of burial (~ 2 km) followed by small amounts of decompression (~ 2 km).

PT paths estimated by the differential method (Spear and Menard, 1989) also indicate an initial period of heating and burial followed by continued heating and uplift (Figure 3.5). The program GIBBS does not allow variation in either muscovite or fluid composition; however, it is completely arbitrary which components are held constant. For comparison, a_{H_2O} was held at 1.0 and the composition of plagioclase was assumed to change continuously from the rim value in either a positive or negative sense. P-T polygons calculated from K_{Eq} equation are also shown for comparison. Kinks in the PT paths calculated by the differential method correspond to the vertical faces of the polygons where a_{H_2O} =1, indicating excellent agreement between the two methods.

Garnet and plagioclase are the only two minerals that contain Ca, whereas muscovite and plagioclase are the only two minerals containing significant amounts of Na. As garnet grows, anorthite component must be used to produce grossular component (all garnets in this study contain some grossular), causing plagioclase to become enriched in albite component. Muscovite and plagioclase lose K and Ca respectively with garnet growth; consequently, both phases should become relatively enriched in Na with garnet growth. It is possible that plagioclase could maintain a constant anorthite component, or even become enriched in anorthite component with garnet growth, if albite component is used to make paragonite component as garnet grows (e.g. reaction 2). If this occurred muscovite would become increasingly paragonitic as plagioclase becomes increasingly anorthitic. The P-T path consistent with increasing paragonite component in

Figure 3.5 PTt paths calculated with using the program GIBBS (Spear and Menard,1989), P-T polygons calculated with K_{Eq} equations are also plotted for comparison. 3.5a. PTt paths calculated for sample 24 from the Thompson Draw synform, a_{H_2O} is assumed to be unity and ΔX_{Ca}^{Pl} is allowed to vary with equal increments between - 0.07 and + 0.14 from the matrix plagioclase value. 3.5b. PTt paths calculated for sample 12 from the Union Hill antiform, a_{H_2O} is assumed to be unity and ΔX_{Ca}^{Pl} is allowed to vary with equal increments between - 0.06 and + 0.06 from the matrix plagioclase value.


A
SAMPLE 24
THOMPSON
DRAW
SYNFORM
Kyanite
Kbar
6
5
4
3
2
1
ΔX^{Pl}_{Ca} = -0.07
ΔX^{Pl}_{Ca} = 0
CORE
RIM
ΔX^{Pl}_{Ca} = 0.14
Andalusite
350
370
390
410
430
450
470
490
510
T °C


B
SAMPLE 12
UNION HILL
ANTIFORM
Pyrophyllite
Kyanite
Kbar
6
5
4
3
2
1
ΔX^{Pl}_{Ca} = -0.06
CORE
ΔX^{Pl}_{Ca} = 0
Rim
ΔX^{Pl}_{Ca} = 0.06
Andalusite
340
360
380
400
420
440
460
T °C

muscovite (Figure 3.4) is essentially the same as the PT path for increasing albite component in plagioclase (Figure 3.5). Therefore, it is difficult for plagioclase to become enriched with anorthite at the same time muscovite is enriched in paragonite, as this would be imply two different P-T paths. Consequently, the lower pressure paths (Figure 3.5) estimated with the program GIBBS are the more likely paths (i. e. ΔX_{Ca}^{Pl}= 0.14, Figure 3.5a, and ΔX_{Ca}^{Pl}= 0.06, Figure 3.5b).

THE ANDALUSITE + BIOTITE ZONE

With increasing metamorphic grade, chlorite is completely eliminated in Fe-rich rocks. The resulting andalusite-biotite zone assemblages are either

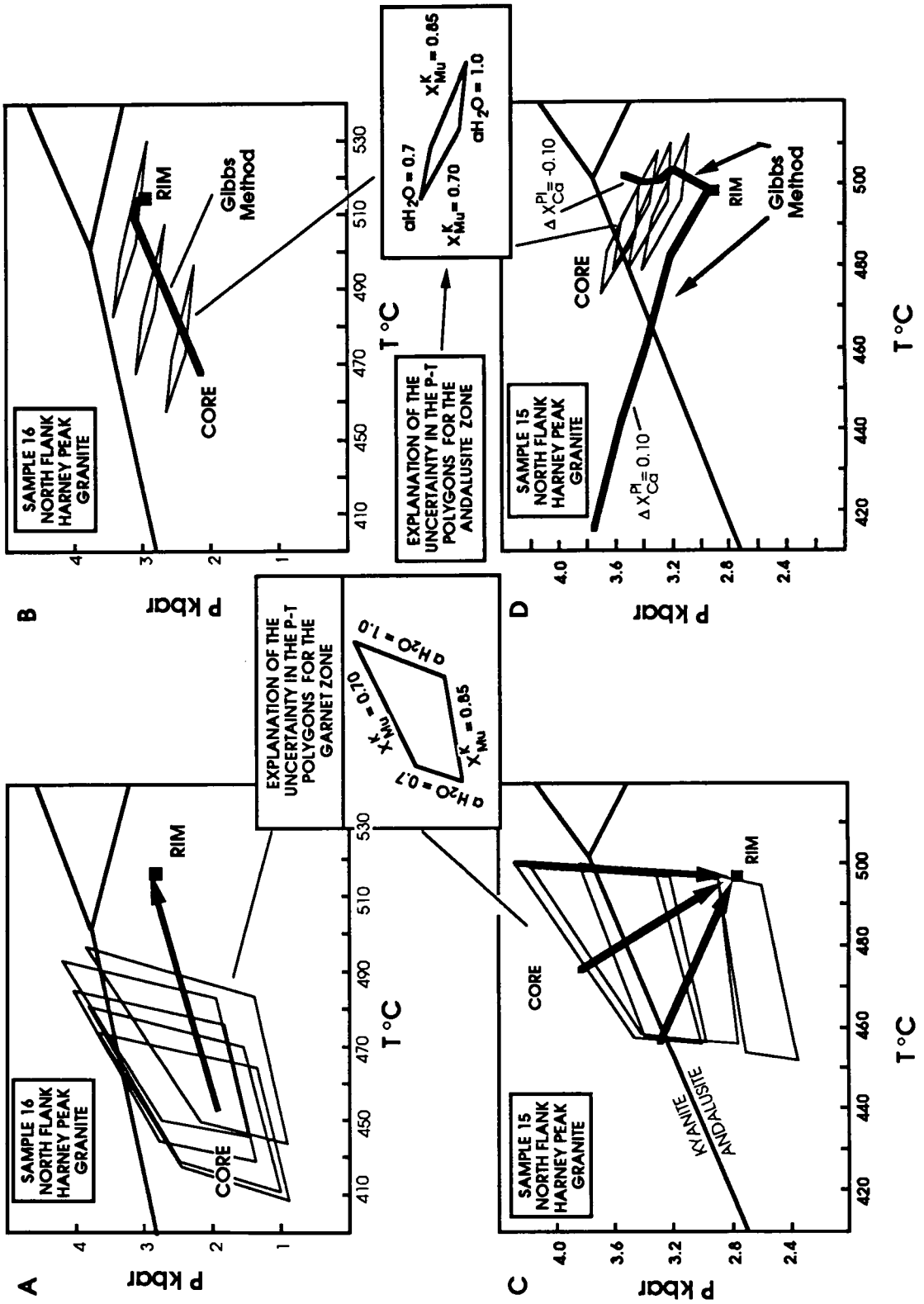
garnet + biotite + staurolite + andalusite + muscovite + plagioclase + quartz (C1)

or

garnet + biotite + andalusite + muscovite + plagioclase + quartz (C2).

Garnets from the andalusite + biotite zone are commonly homogeneous; however, sample 16 from the northeastern flank of the Harney peak granite is moderately zoned (Figure 3.3c). Garnet from sample 16 may have grown in the presence of assemblage (A) initially, followed by growth in the presence of assemblage C1. The PT path calculated with the equation set in Table 3.3 (garnet zone) indicates a prograde, low-pressure path (Figure 3.6a). Within the presumed compositional limits, X_K^{Mu}= 0.7-0.85, and a_{H2O} = 0.7-1, ΔP is poorly resolved. Note that no reasonable prediction can be made about the changes in muscovite composition with garnet growth. Although the garnet core is likely to have been buffered by the garnet zone assemblage, in the andalusite-zone assemblage muscovite composition is governed to a large extent by reaction (9), which is very sensitive to changes in temperature

Figure 3.6. Andalusite zone PT paths A) PT paths calculated for garnet sample 16 using the set of equations in Table 3.3 (the garnet zone). B) PT path calculated for garnet sample 16 with the set of equations in Table 3.4 (andalusite zone); the PT path was estimated with the program GIBBS at X_{Fe}^{St} = 0.88. C) PT path calculated for garnet sample 16 with the set of equations in Table 3.4 (the garnet zone). D) PT path calculated for garnet sample 16 with the set of equations presented in Table 3.4 (andalusite zone); the PT paths were estimated with the program GIBBS assuming ΔX_{Ca}^{Pl} = -0.10 and + 0.10.


A
SAMPLE 16
NORTH FLANK
HARNEY PEAK
GRANITE
RIM
CORE
P kbar
T °C
B
SAMPLE 16
NORTH FLANK
HARNEY PEAK
GRANITE
RIM
CORE
Gibbs
Method
P kbar
T °C
EXPLANATION OF THE
UNCERTAINTY IN THE P-T
POLYGONS FOR THE
GARNET ZONE
EXPLANATION OF THE
UNCERTAINTY IN THE P-T
POLYGONS FOR THE
ANDALUSITE ZONE
C
SAMPLE 15
NORTH FLANK
HARNEY PEAK
GRANITE
CORE
RIM
KYANITE
ANDALUSITE
P kbar
T °C
D
SAMPLE 15
NORTH FLANK
HARNEY PEAK
GRANITE
CORE
RIM
Gibbs
Method
P kbar
T °C

and a_{H_2O}. The PT path (Figure 3.6b) calculated with the equation set in Table 3.4 (andalusite zone) indicates burial under prograde conditions. The PT path was estimated by the differential method assuming constant staurolite composition (staurolite components are retained for calculation made with the program GIBBS). PT polygons (Figure 3.6b) were estimated with the equation set in Table 3.5, at the extremes of the limits X_K^{Mu} = 0.7-0.85, and a_{H2O} = 0.7-1. No matter which assemblage is assumed to have buffered garnet composition, garnet zoning records a minimum ΔT of ~50 °C; however, ΔP is uncertain.

Garnets, from schists located 1-2 km from the granite contact, are nearly homogeneous. Sample 15, located 1.5 km north of the Harney Peak granite, is nearly homogeneous; however, in the outer 200 μm of the garnet Fe and Mn slightly increase, whereas Mg and Ca slightly decrease. The PT path estimated with the equations in Table 3.3 (garnet zone) indicates some decompression (Figure 3.6c). The PT paths calculated with the equation set in Table 3.4 (andalusite zone) also indicate decompression (Figure 3.6d). PT paths estimated with the equation set in Table 3.4 are shown as error polygons (Figure 3.6d). A set of possible PT paths were also calculated by the differential method at ΔX_{CA}^{Pl} = -0.10 and 0.10, assuming a_{H2O} = 1 (Figure 3.6d); both methods indicate decompression.

SILLIMANITE AND SILLIMANITE + BIOTITE + GARNET ZONE

Sillimanite-grade garnets are not used to calculate PT paths because they have been partially consumed by continuous reactions. As a further complication, sillimanite-grade garnets may have grown in the presence of several different assemblages, and it is uncertain with which assemblage to

model core compositions. Reaction textures in sillimanite-zone schists provide qualitative clues about the PT path. The reaction set presented in Table 3.2 for the andalusite zone assemblage is equally appropriate for the sillimanite-zone assemblage

garnet + biotite + sillimanite + muscovite + plagioclase + quartz (D)

if andalusite is replaced by sillimanite. Mineral textures and compositional zoning in garnet indicate that garnet partially reacted to form sillimanite and biotite. Garnets are commonly embayed by mats of fibrolitic sillimanite. Garnet and biotite are the only ferromagnesian silicates in assemblage (D); therefore, all closed-system garnet-consuming reactions produce biotite. The small enrichment in Fe and the depletion of Mg at the garnet rim are consistent with the reaction of garnet to form biotite because $X_{Mg}^{Bi} >> X_{Mg}^{Gar}$. Biotite contains negligible amounts of Mn (~0.005 mole % in rocks from the Black Hills) and no Ca; consequently, garnet-consuming reactions should result in Mn and Ca enrichment in garnet rims. Garnet sample 28 shows both textural evidence of resorption and an enrichment in spessartine component at the rim (Figure 3.3e). There is no Ca enrichment at the rim, perhaps reflecting production of anorthite.

The major garnet-consuming reactions in assemblage (D)

pyrope + muscovite = 2 sillimanite + phlogopite + quartz, (1-8)

almandine + muscovite = 2 sillimanite + annite + quartz, (1-8+4)

and

grossular + Al_2SiO_5 + 2 quartz = 3 anorthite (8)

are sensitive to changes in pressure. PT space has been contoured for constant garnet (Figure 3.8) in the simplified KFMASH systems with the thermodynamic data set of Holland and Powell (1990). Reactions (1 + 8) (the linear combination of reactions (1) and (8) from Table 3.3) and (1 - 8 + 4) largely control the mode of garnet in assemblage (D) and reaction (8) controls the amount of grossular component in garnet. Because garnet is on the high-pressure, high-temperature side of the isopleths for X_{Mg}^{Gar}, the greatest amount of garnet resorption occurs with decompression and cooling. The lack of a Ca enrichment in garnet rims is consistent with the production of anorthite during decompression. The lack of change in grossular also indicates that the decompression path has nearly paralleled the grossular isopleths. The grossular isopleths have a positive slope (e.g. reaction (8) has a positive slope), indicating that the PT path was characterized by decompression and cooling. The amount of decompression and/or cooling that occurred is difficult to evaluate quantitatively. The presence of muscovite pseudomorphs of andalusite (some preserving chiastolite structures) in the sillimanite zone indicates that the lower-temperature portions of the PT path occurred at pressures below 3.7 kbar (i.e. Holdaway, 1971). These data at least suggest a clockwise PT path (Figure 3.7)

DISCUSSION

The error associated with the PT paths is potentially great. In garnet- and staurolite-grade rocks, the effects of volume diffusion have probably been very small, because peak temperatures were ≤500 °C (e.g. Lasaga et al., 1977; Tracy, 1982; Cygan and Lasaga, 1985). However, there are uncertainties in the thermodynamic data, the experimentally determined geothermobarometers,

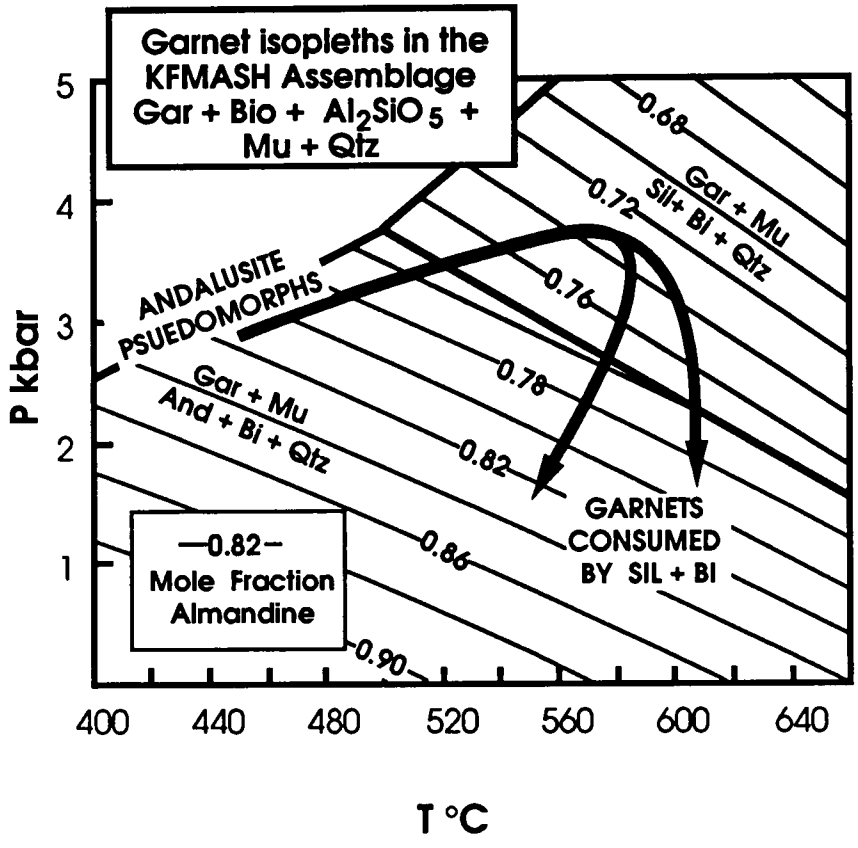


Figure 3.7. Isopleths of garnet and biotite compositions in the KFMASH assemblages garnet + biotite + sillimanite + muscovite + quartz and garnet + biotite + andalusite + muscovite + quartz.

the activity-composition relationships used for the solid solutions, as well as uncertainty associated with microprobe analyses. Uncertainty in the K_{Eq} equations is difficult to evaluate; however, the reproduction of mineral compositions (Table 3.5) is generally good, suggesting that the system K_{Eq}-equations are approximately correct. The consistency in PT paths estimated from the three Thompson Draw garnets indicate that the activity-composition models are also generally reliable, as the three garnets have different rim compositions. Agreement between PT paths estimated with the differential and integrated methods is also reassuring, as the former method does not incorporate the errors associated with the enthalpies of reaction (Spear and Selverstone, 1983).

PT paths from the Thompson Draw synform are prograde, near-isobaric, and clockwise. Garnet sample 23 from the Thompson Draw synform contains muscovite inclusions that clearly indicate that the garnet core equilibrated at the same pressure as the rim (2.5-3.5 kbar); therefore, the final prograde PT path (100 to 70 °C) of sample 23 is nearly isobaric, with perhaps a small increase in pressure (~ +0.5 kbar) followed by a decrease in pressure of the same magnitude. Arrays of PT polygons, estimated from two other garnet samples (20 and 24) from the Thompson Draw synform, are consistent with the path estimated with garnet sample 23. All estimated PT paths, exclusive of sample 15, are very similar to the path of the metamorphic field gradient.

Garnet sample 15 is homogeneous except for the outer 200 μm, suggesting retrograde diffusion (e.g. Selverstone and Chamberlain, 1990). The decompression path recorded by sample 15 is specious because other

adjacent homogeneous garnets record either isothermal-isobaric growth, or near-isobaric growth with increasing a_{H_2O} and temperature.

Homogeneous andalusite-grade garnets can be interpreted in at least 3 different ways. These include (1) homogenenization due to volume diffusion, (2) isothermal-isobaric growth, and (3) near-isobaric heating with a coeval increase in a_{H_2O}. Distinction among these three possibilities could provide a crude approximation of the amount of time that amphibolite-facies conditions were maintained.

Garnets may have grown at nearly constant pressure and temperature. It is possible for garnet to nucleate in a rock of the appropriate composition at temperatures and pressures consistent with andalusite-grade conditions, and to remain at these conditions during garnet growth. Homogeneous andalusite zone garnets, however, have approximately the same composition as the rims of zoned garnets in the staurolite zone (e.g. ~10 mole % Mn, ~80 mole % Fe, ~8 mole % Mg, ~2 mole % Ca). Because biotite contains negligible concentrations of Mn at all grades, chlorite is the major source of Mn for growing garnets. The andalusite zone is characterized by the absence of chlorite at Fe-rich compositions. Garnet nucleating in the andalusite zone can only receive Fe, Mg, and Mn from biotite, and should contain negligible spessartine component from core to rim. Therefore, isobaric-isothermal growth seems an unlikely cause of flat zoning profiles in andalusite-grade garnets.

Flat zoning profiles in the high-grade portion of the andalusite zone may reflect garnet growth with increasing a_{H_2O} and temperature, at near isobaric conditions. The latter case does not seem consistent with the generally high, and remarkably similar values of a_{H_2O} (~0.9 ± 0.1) recorded by

the matrix assemblages (Helms and Labotka, 1991).

Prograde homogenization of garnet strongly suggests that volume diffusion erased compositional zoning. Homogenization of compositional zoning by volume diffusion is common in upper amphibolite facies garnets (600-650 °C, Lasaga et al., 1977; Yardley, 1977; Tracy, 1982; Cygan and Lasaga, 1985; Spear, 1988). The temperature range 600-650 °C is consistent with the second-sillimanite zone and perhaps the sillimanite + biotite + garnet zone; however, maximum temperatures recorded in the andalusite + biotite zone are ~565 °C (Helms and Labotka, 1991). Homogeneous garnets in the andalusite-zone typically have radii of ~5.0 x 10^{-4} m. The characteristic time necessary for homogenization of 2 coupled components (i.e. Fe-Mn) in a garnet with this radius is approximately ~40 x 10^{6} years at 600 °C (Cygan and Lasaga, 1985). At a temperature of 565°C the time required for homogenization is ~300 x 10^{6} years. Temperature is unlikely to have been at a maximum during the entire temperature-time path; therefore, these times represent a minimum time for homogenization to occur (Spear, 1988).

The unrealistically large characteristic time for diffusion at temperatures recorded by andalusite-grade schists suggests that volume diffusion could not have homogenized garnets. However, the activation energy (239 kJ/mole) reported by Cygan and Lasaga (1985) has a reported uncertainty of ±16 kJ/mole. Within this modest range of uncertainty, the characteristic time for diffusion for a garnet at 565 °C, with a radius of ~5.0 x 10^{-4} m, varies between 3 x 10^{9} and 2.8 x 10^{7} years. The lower limits of this range indicate that within the uncertainty associated with the activation energy, it possible that volume diffusion erased compositional heterogeneity

in garnets within a reasonable amount of geologic time (~10^8 years; e.g., England and Thompson, 1984).

There is also a direct correlation between the radius of the garnet and the degree of homogenization at andalusite grade. For example, compare andalusite grade sample 15 (Figure 3.2c) and 16 (Figure 3.2d). Garnet sample 16 has a radius of approximately 4 mm and garnet sample 15 has a radius of 1.4 mm. Because the degree of homogenization due to volume diffusion is directly related to the radius of the garnet (e.g. Spear, 1988), this comparison provides qualitative evidence that volume diffusion has erased the original compositional heterogeneity in andalusite-grade garnets.

TECTONIC SIGNIFICANCE

Prograde low-pressure, high-temperature metamorphism in compressional tectonic terrains has been attributed to (1) heat advected from the lower crust to the middle crust by anatectic melts (e.g. England and Thompson, 1984; Lux et al., 1986) and to (2) an increased heat flux from the mantle (e.g. Loovsfeld and Etheridge, 1990; Labotka and Albee, 1988). The model of England and Thompson (1984) demonstrates that crustal thickening can result in lower crustal temperatures exceeding the wet, and perhaps the dry granite solidus; consequently, case (1) does not necessarily imply case (2).

There are certainly other models for low-pressure, high-temperature metamorphism. The numerical simulations of crustal thickening of England and Thompson (1984) produced some PTt paths that passed retrogressively across the sillimanite-andalusite transition during exhumation. Retrograde PTt paths occurred only when the extreme limits of

the input parameters were incorporated in the model. More importantly, however, PT paths from the Black Hills are clearly prograde.

Models based on crustal thinning with coincident asthenospheric (thermal) upwelling (e.g. Wickham and Oxburgh, 1985; Thompson, 1989) are not appropriate for the Black Hills, because the thermal anomaly associated with crustal thinning commonly lasts less than 50-60 million years (e.g. Loovsfeld and Etheridge, 1990). Crustal thickening in the Black Hills was associated with the Trans-Hudson orogeny at ~1.8 Ga, and mafic schists that might be interpreted as basaltic lavas associated with extension are > 1.8 Ga in age (Redden et al., 1991). Metamorphism in the Black Hills occurred at approximately 1.7 Ga. Therefore, the 100 million years between crustal thickening and peak metamorphism indicates that crustal thinning was not an important factor in regional metamorphism.

Assuming the preceding models are inappropriate for the Black Hills, further consideration is given to advective heating and an increased heat flux from the mantle. A cooling granitic magma at a depth of 12-14 km can only cause amphibolite facies temperatures (~500 °C) at a distance of ~1-2 km from its contact (e.g. Lovering, 1935; Lux et al., 1986; Barton and Hanson, 1989; Loovsfeld and Etheridge. 1990). Gravity data (Duke et al., 1991) indicate that much of the sillimanite zone south of the field area is underlain by granite, and that the Harney Peak granite extents in the subsurface north of the granite-country rock contact; however, there is no evidence for granite beneath the Thompson Draw synform. It is possible that granite once overlaid the synform; however, this is clearly impossible to verify from simple observation.

The amount of real time (Δt) along the PT paths in Figure 3.4 is

needed to distinguish between advective heating and an increased heat flux at the base of the crust. Because the advective heat source must be very close to the metamorphosed rock, advective heating will be rapid relative to heating caused by an increased flux at the base of the crust. Assuming a thermal diffusivity (κ) of 9.0×10^{-7} m^2/s (e.g. England and Thompson, 1984), the characteristic time ($t = l^2/\kappa$) for a heat pulse to travel l = 1 km to 2 km, is of the order of 10^5 years. The characteristic time for a pulse of heat to travel from the base of the crust to the middle crust ($l \geq 40$ km) is 10^8 to 10^7 years. If PT paths in Figure 3.4 are due to heat derived from a cooling granite, Δt should be a factor of 10^5 years. If the PT paths are due to an increased heat flux from the mantle Δt will be a factor of 10^7 years.

The only constraint on Δt is provided by homogeneous andalusite-grade garnets. Contact metamorphism in the upper crust is a transient thermal event that results in amphibolite-facies conditions that last no more than ~10^5 years (e.g. Lovering, 1935; Lux et al., 1986; Loovsfeld and Etheridge. 1990). If volume diffusion caused homogenization of garnets at andalusite-grade conditions, then PT paths (Figure 3.4) are unlikely to have resulted from "regional" contact metamorphism. We suggest that regional metamorphism in the Black Hills resulted from a thermal anomaly that sustained amphibolite facies conditions on the order of at least 10^7 years. The cause of a sustained thermal anomaly is uncertain. An increased heat flux at the base of the crust is one possible cause of such a long-lived thermal anomaly (Loovsfeld and Etheridge, 1990). Another possible cause of a sustained thermal anomaly is self-heating due to the decay of radiogenic isotopes, concentrated in the upper crust (e.g. Sclater et al., 1980).

Homogeneous thickening of the crust followed by slow uplift (~0.015 mm/yr) can cause temperatures in the upper crust (-13 km) to reach middle amphibolite facies conditions isobarically, and results in lower crustal (> -30 km) temperatures exceeding the granite solidus (Helms, 1991).

CONCLUSIONS

The distribution of isotherms and isograds in the Black Hills indicates a gradual southward increase in temperature. Isotherms and isograds are approximately oriented east-west, but locally wrap around the northern flank of the Harney Peak granite. The sporadic occurrence of kyanite in the western portion of the study area and to the immediate south of the study area indicate a gradual increase in pressure to the south and west of the Harney Peak granite. PT paths recorded by garnets indicate a 100 to 70 °C increase in temperature with pressure changes of ± 0.5 kbar (± 2 km). The initial portion of the PT paths generally records a slight increase in pressure, followed by a decrease in pressure of similar magnitude. At distances of < 1.5 km from the Harney Peak granite, garnets are commonly homogeneous. The cause of homogeneity is uncertain but may reflect volume diffusion.

The tectonothermal interpretation of PT paths estimated in this study are uncertain because the value of Δt along the path is unknown. Homogenization of andalusite-grade garnets by volume diffusion suggests amphibolite-grade conditions must have been maintained on the order of $\sim 10^7$ years. It is unlikely that a cooling magma could maintain amphibolite-facies conditions for more than 10^5 years. The Harney Peak granite, however, undoubtedly provided much of the heat necessary for sillimanite + garnet + biotite and sillimanite + K-feldspar conditions adjacent to the

granite. The cause of regional metamorphism appears to have been a long-lived thermal anomaly. The cause of the thermal anomaly is uncertain, but may have been an increased heat flux at the base of the crust and/or self-heating caused by thickening of the upper crust, which is believed be enriched in radiogenic heat-producing elements.

CHAPTER IV

THE THERMAL CONSEQUENCES OF HOMOGENEOUS CRUSTAL THICKENING AND SLOW UPLIFT: A MODEL FOR LOW-PRESSURE, HIGH-TEMPERATURE METAMORPHISM

INTRODUCTION

The tectonic and thermal processes that result in regional low-pressure, high-temperature metamorphism remain uncertain and controversial (e.g. Barton and Hanson, 1989; Loovsfeld and Ethridge, 1990). Regional low-pressure, high-temperature metamorphism occurs in a variety of tectonic environments, including volcanic arcs (Miyashiro, 1963; Barton and Hanson, 1989), continental collision zones (Lux et al., 1986; Loovsfeld, 1989; Helms and Labotka, 1991a; 1991b), and continental rift zones (Wickham and Oxburgh, 1985; Grambling et al., 1989; Thompson, 1989). The diversity of tectonic environments effected by regional low-pressure, high-temperature metamorphism suggests that a single tectonic and thermal model is unlikely to be applicable to all terrains.

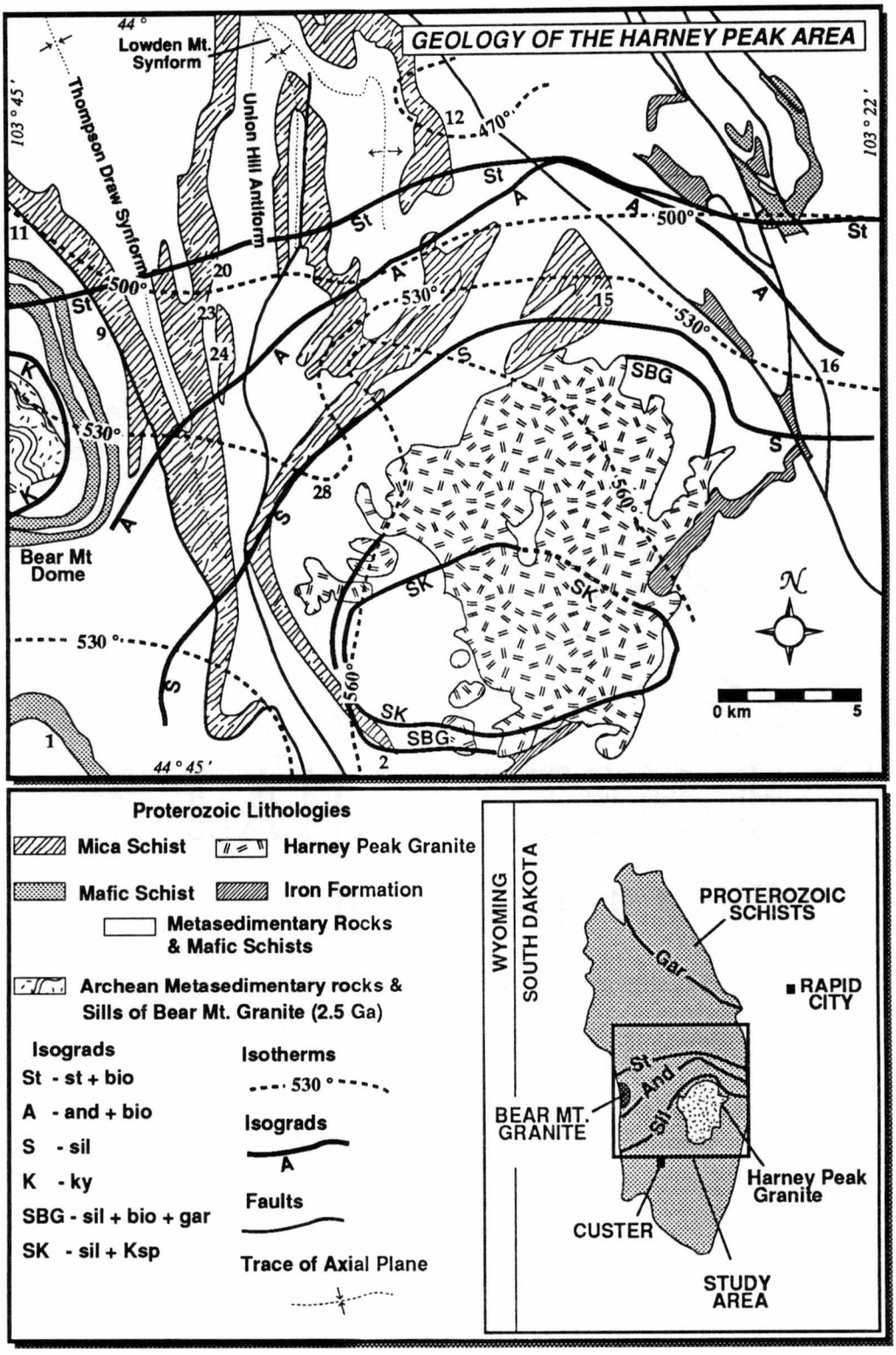
Although regional low-pressure, high-temperature metamorphism has affected terrains of all ages, it is particularly common in Early Proterozoic terrains that are between 1.8-1.6 Ga in age (Dewey and Burke, 1973; Windley, 1977). Proterozoic schists exposed in the Black Hills, S.D. were regionally metamorphosed under low-pressure, high-temperature conditions, characterized by temperature-to-depth ratios of 35-65 °C/km at ~1.8-1.7 Ga (Redden et al., 1991). Metamorphism in the Black Hills occurred during and after compressional tectonics related to the accretion of the Archean-aged Wyoming and Superior cratons, and may also be related to thermal activity associated with the development of the ~1.7 Ga Midcontinent orogen to the south (Redden et al., 1991).

Metamorphism began during the late stages of polyphase folding; however, upper greenschist through upper amphibolite facies conditions,

and intrusion of the Harney Peak granite (Figure 4.1) occurred after the major period of folding (Redden, 1963; Redden, 1968; Redden and Norton, 1975; Helms and Labotka, 1991a). The Harney Peak granite is a peraluminous, S-type granite (Walker et al., 1986). Geologic thermometry and barometry indicate that metamorphism in the Black Hills occurred at a pressure of 3.0 ± 0.6 kbar (Helms and Labotka, 1991a). Slightly higher pressures (~4.2 kbar) are recorded by kyanite-bearing schists in the Bear Mountain area (Figure 4.1), and in the area south of sample location 1 on Figure 4.1 (Redden, 1963). The distribution of isograds and isotherms (Figure 4.1) record a gradual southward increase in metamorphic grade (Helms and Labotka, 1991a; Redden and Norton, 1975). Isotherms based on temperatures estimated with the garnet-biotite geothermometer (Ganguly and Saxena, 1984) are contoured on Figure 4.1 (Helms and Labotka, 1991a). A broad garnet zone extends ~25 km southward from an unconformity between Cambrian and Early Proterozoic lithologies, to an east-trending staurolite isograd. Together, the staurolite and andalusite zones are approximately 5 km to 10 km wide and are bounded to the south by a broad sillimanite zone. Sillimanite-zone schists extend ~30 km southward before dipping beneath the unconformity below Cambrian lithologies. Sillimanite + K-feldspar conditions were reached locally along the southern flank of the Harney Peak granite.

Metamorphism has not been dated; however, schists adjacent to the Harney Peak granite record the highest temperatures, suggesting that

Figure 4.1. Map of the Harney Peak area including the distribution of isograds, isotherms and simplified geology (after Dewitt et al., 1988). Isotherms are based on Fe/Mg partitioning between garnet and biotite (Ganguly and Saxena, 1984).

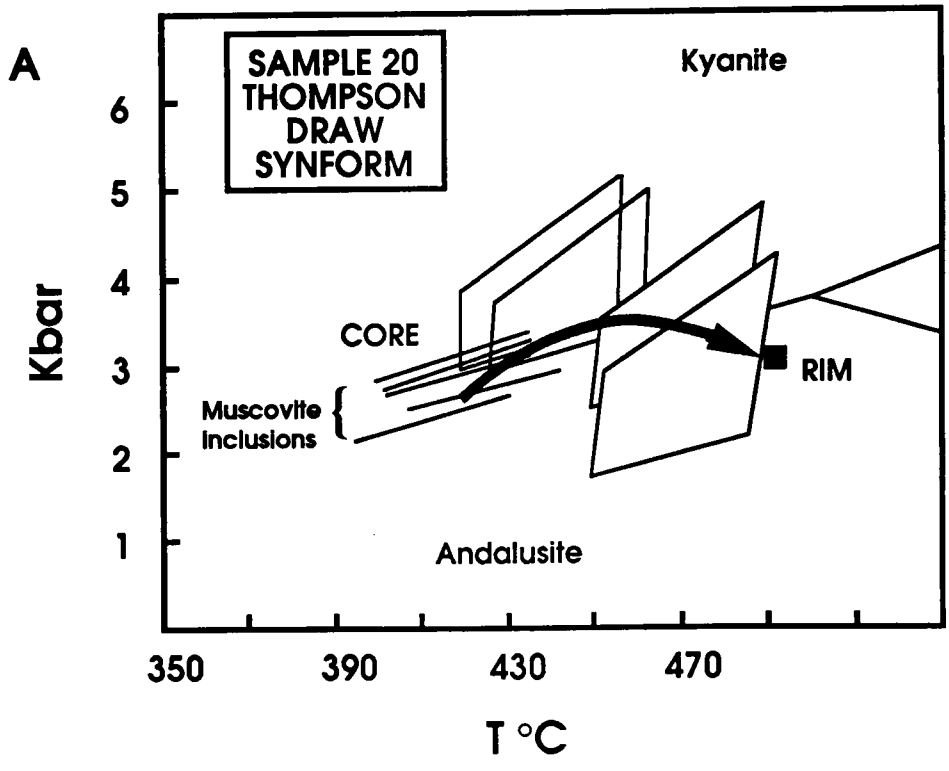

GEOLOGY OF THE HARNEY PEAK AREA
44°
103° 45'
103° 22'
Lowden Mt. Synform
Thompson Draw Synform
Union Hill Antiform
Bear Mt Dome
SBG
SK
St
A
S
K
470°
500°
530°
560°
0 km
5
44° 45'
Proterozoic Lithologies
Mica Schist
Harney Peak Granite
Mafic Schist
Iron Formation
Metasedimentary Rocks & Mafic Schists
Archean Metasedimentary rocks & Sills of Bear Mt. Granite (2.5 Ga)
Isograds
St - st + bio
A - and + bio
S - sil
K - ky
SBG - sil + bio + gar
SK - sil + Ksp
Isotherms
530°
Isograds
Faults
Trace of Axial Plane
WYOMING
SOUTH DAKOTA
PROTEROZOIC SCHISTS
Gar
RAPID CITY
St
And
Sil
BEAR MT. GRANITE
Harney Peak Granite
CUSTER
STUDY AREA

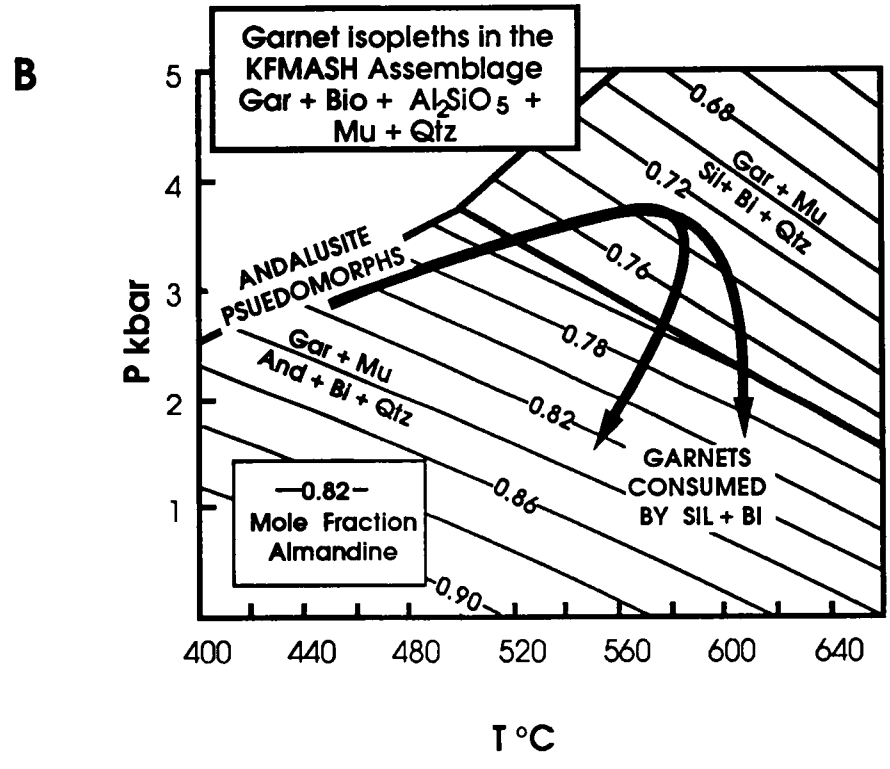
metamorphism and granite emplacement were partly coeval. Both Rb/Sr (Riley, 1970; Walker, et al., 1986) and U/Pb (Redden et al., 1991) whole rock isochrons indicate that the granite crystallized at 1.71 Ga. The granite locally deformed north-trending fold axes, and may have deformed east-trending andalusite and sillimanite isograds (Figure 4.1); however, the apparent deformation of isograds may be a thermal effect.

Prograde PT paths were inferred from compositionally zoned garnets and reaction textures in Helms and Labotka (1991b). Prograde PT paths were found to be clockwise and nearly isobaric (Figure 4.2). Reaction textures in sillimanite-zone rocks indicated a retrograde clockwise decompression path. Positive correlation between grade and the degree of homogenization suggested that homogenization resulted from volume diffusion, indicating that middle- to upper-amphibolite facies conditions were maintained at least on the order of 10^7 years (Helms and Labotka, 1991b).

High-temperature, low-pressure metamorphism associated with crustal thickening and continental collision has been modeled in previous studies; however, none of these simulations are consistent with observations made about the metamorphism of the Black Hills. The extensive numerical experiments of England and Thompson (1984) simulated the thermal consequences of uplift subsequent to instantaneous, homogeneous crustal thickening, and crustal thickening by a single, instantaneously emplaced horizontal thrust sheet. Within the chosen range of uplift rates (0.13 to 0.7 mm/yr), low-pressure, high-temperature metamorphism occurred only with a combination of high-radiogenic heat production (2.33 $\mu W/m^3$), high mantle heat flux (40 mW/m^2), and low thermal conductivity (1.5 W/mK).

Figure 4.2. A) Representative PT path estimated from a reaction zoned garnet collected in the Thompson Draw synform (sample 24, Figure 4.1). PT polygons represent uncertainty in the muscovite composition and aH_2O; the vertical faces reflect constant aH_2O at 1.0 and 0.7, whereas the sub-horizontal faces are isopleths of constant muscovite composition at X_K^{Mu} = 0.7 and 0.85 (Helms and Labotka, 1991b). B) Qualitative PT path based on reaction textures in sillimanite-grade schists (Helms and Labotka, 1991b).


A
SAMPLE 20
THOMPSON
DRAW
SYNFORM
Kyanite
CORE
RIM
Muscovite
inclusions
Andalusite
Kbar
6
5
4
3
2
1
350
390
430
470
T °C


B
Garnet isopleths in the
KFMASH Assemblage
Gar + Bio + Al2SiO5 +
Mu + Qtz
0.68
0.72
Gar + Mu
Sil + Bi + Qtz
ANDALUSITE
PSUEDOMORPHS
0.76
0.78
Gar + Mu
And + Bi + Qtz
0.82
GARNETS
CONSUMED
BY SIL + BI
—0.82—
Mole Fraction
Almandine
0.86
0.90
P kbar
5
4
3
2
1
400
440
480
520
560
600
640
T °C

In contrast to PT paths from the Black Hills, low-pressure, high-temperature PTt paths in England and Thompson (1984) passed through the sillimanite-andalusite transition retrogressively. Crustal thickening, however, resulted in lower crustal temperatures that exceeded the wet and dry granite solidi (England and Thompson, 1984).

Lux et al. (1986) suggested that regional low-pressure, high-temperature metamorphism in continental collision zones results from advective heating by granitic melts that form in the lower crust in response to crustal thickening. Even at an exhumation rate of ~0.35 mm/yr (Lux et al., 1986), the portion of the PTt paths resulting from advective heating is characterized by isobaric heating and cooling. Although isobaric heating is consistent with PT paths determined by in Helms and Labotka (1991b), a cooling granitic magma can only cause amphibolite-facies conditions at distances less than ~2 km from the contact (e.g. Lovering, 1935; Lux et al., 1986; Labotka et al., 1988). Although there is geophysical evidence to suggest some buried plutons in the Black Hills, the quantity is probably insufficient to account for regional metamorphism. Furthermore, the time that amphibolite-facies temperatures are maintained in a contact metamorphic environment is on the order of 10^6 years; in contrast, homogenized garnets within 1-2 km of the Harney Peak granite suggest amphibolite facies conditions lasted on the order of 10^7 years.

Loosveld (1989) suggested that low-pressure, high-temperature metamorphism synchronous with crustal thickening results from rapid thinning of the lithosphere. Lithospheric thinning may be a consequence of continent-continent collision (Bird, 1978; Houseman et al., 1981). The effect

of thinning or removing the lithosphere is to place hot (~1300-1450 °C) asthenospheric convection cells closer to the upper crust. In contrast to PT paths from the Black Hills, model PTt paths presented in Loosveld (1989) are anticlockwise and characterized by isobaric cooling.

Several one-dimensional and two-dimensional numerical heat flow experiments were performed to determine potential causes of metamorphism in the Black Hills. A simple thermal model is sought that is both consistent with observation and relies upon both a normal mantle heat flux and radiogenic heat supply. Numerical experiments focus on the thermal effects of slow exhumation rates subsequent to homogeneous crustal thickening. The models presented below first examine the effects of homogeneous thickening followed by differing rates of uplift with a simple one-dimensional finite difference model. This first model incorporates radiogenic heat production rates measured from several lithologic units from the Black Hills and assumes a mantle heat flux consistent with modern values. Two-dimensional finite-difference models are also used to examine the thermal consequences of emplacing a pluton into a steady-state geotherm both before homogeneous thickening and slow uplift, and after ~36 million years of slow uplift.

CRUSTAL THICKENING AND UPLIFT IN THE BLACK HILLS

Regional metamorphism and deformation between ~1.8 and 1.7 Ga were associated with the collision and subsequent suturing of the Archean Wyoming and Superior cratons (Redden et al., 1991). The amount of crustal thickening that occurred during the suturing of these two continental blocks and the elapsed time between crustal thickening and peak metamorphism

are uncertain. Information available to evaluate the amount of thickening includes the current crustal thickness, the amount of erosion that occurred after peak metamorphism, and by analogy, crustal thicknesses measured in modern continental-collision zones. Geobarometry indicates that 12 to 16 km of crust have been removed from the present crustal thickness of 45 to 55 km (McCamy and Meyer, 1964; Braile et al., 1989). The sum of these thicknesses suggests a total crustal thickness of ~60 to 70 km at the time of peak metamorphism. Substantial uncertainty is associated with this estimate of the crustal thickness at 1.7 Ga. It is possible that the present thickness was modified during Tertiary Laramide orogensis or during the later stages of crustal thickening at 1.7 Ga. The thickness of 60 to 70 km is, however, consistent with thicknesses measured at modern continental collision zones such as the Himalayas and the Tibetan Plateau (e.g. Dewey and Burke, 1973; Molnar and Tappnnier, 1975). In models presented below the crustal thickness is doubled from 35 km to 70 km.

The mode of crustal thickening in the Black Hill is uncertain, as structural control in the vertical dimension is unavailable. Ductile polyphase folding (Figure 4.1) suggests approximately homogeneous thickening of the crust. Because of the rapid rate of crustal thickening inferred from modern continental collision zones (~1-2 cm/yr; Trumpy, 1979; Gansser, 1979) and the relatively slow rate of heat conduction in rock, several workers have modeled the thermal consequences of crustal thickening as instantaneous (e.g. Oxburgh and Turcotte, 1972; England, 1978; England and Thompson, 1984). Instantaneous homogeneous thickening is assumed in the models presented below.

The uplift rate in the Black Hills following crustal thickening is also uncertain. Early Proterozoic metamorphic schists are unconformably overlain by Cambrian sandstone (~0.6 Ga); consequently, following peak metamorphism at 1.7 Ga, between 12 and 16 km of uplift occurred in $\sim 10^9$ years. A constant and continuous exhumation would indicate a rate of ~0.014 mm/yr. It is impossible to know instantaneous uplift rates, and the constant rate of 0.014 mm/yr is only one possible answer. However, the PT paths shown in Figure 4.3 are consistent with a small vertical component of motion during heating. Figure 4.3a indicates a ~100 °C increase in temperature coincident with only small changes in depth (± 2 km).

HEAT SOURCES AND HEAT SINKS

The conductive steady-state geotherm of continental crust is governed by the distribution of radioactive heat-producing isotopes and by the heat flux Q_r at the base of the crust (Sclater et al., 1980). The radioactive heat production A_r is commonly modeled as constant (e.g. Roy et al., 1968; England and Thompson, 1984) to a depth D, or as having a rate that exponentially approaches 0 at D (Lachenbruch, 1970). The mantle heat flux, the distribution of radioactive heat-producing isotopes, and the thickness of the heat-producing layer are poorly known (Sclater et al., 1980).

The mantle heat flux at 1.8-1.7 Ga is model-dependent (e.g. Davies, 1980). Estimates of the mantle heat flux in eastern North America indicate a value of ~33 mW/m^2 (Sclater et al., 1980). A portion of the mantle heat flux must be due to the the decay of radioactive isotopes in the lower crust and mantle; therefore, the mantle heat flux is likely to have been greater at 1.8-1.7 Ga. The value of 33 mW/m^2 is incorporated in the models presented below,

although, this is probably a lower limit.

The initial thickness of the upper heat-producing layer is set at 15 km (cf. England and Thompson, 1984). Heat production due to the decay of radioactive elements was estimated from the concentrations of U, Th, and K in the Bear Mountain granite (Gosselin et al., 1989), the Harney Peak granite (Shear et al., 1987), and the mica schist unit (Schwandt, personal communication). The Bear Mountain granite may be representative of the basement rocks on which supracrustal lithologies were deposited (Walker et al., 1986; Dewitt et al., 1986; Gosselin et al., 1989). The average concentrations of U, Th, and K (Table 4.1) in both the Bear Mountain granite and the mica schist unit indicate an average heat production rates of 3.0 $\mu W/m^3$ and 3.3 $\mu W/m^3$, respectively at 1.7 Ga. The concentrations of U, Th, and K (Table 4.1) in the Harney Peak granite vary considerably (Table 4.1), consequently, the rate of heat production varies between 3.6 and 13.7 $\mu W/m^3$. A gamma-ray survey has also revealed a significant anomaly above the Harney Peak granite (Dewitt et al., 1986), indicating a higher concentration of radiogenic isotopes in the granite relative to the surrounding country rock. Rates of radiogenic heat production (Table 4.1) were estimated using the decay and heat production constants reported in Turcotte and Schubert (1982).

The internal heat production due to the decay of ^{40}K, ^{238}U, ^{235}U, and ^{232}Th is time-dependent. Several numerical experiments presented below follow PTt paths where t = 10^9 years; this is a sufficient amount of time to decrease the internal heat production by ~40%. However, maximum temperatures were attained within ~10^7 years; this is an insufficient time to alter significantly the rate of heat production. Because this study is primarily concerned with the causes of prograde metamorphism, A_r is assumed

Table 4.1. Heat Production Rates of Selected Lithologies from the Black Hills

	U (ppm)	Th (ppm)	K_2O (wt. %)	Heat Production ($\mu W/m^3$)
Bear Mt. Granite	3.82	6.68	4.81	3.0
Mica Schist Unit	2.70	17.98	4.04	3.3
Harney Peak Granite	6.-30.0	6.-10	3.72-6.50	3.6-13.7

Note: Decay constants and heat production rates are from Oxburgh and Schubert (1982)

constant unless stated otherwise.

Decay of radiogenic isotopes constitutes the major crustal heat source. There are, however, other minor and transient crustal heat sources and heat sinks. Dehydration reactions are almost always endothermic. The rate of heat absorption due to devolatization reactions is approximately

$$A_{h.r.} = x_j \rho_r \Delta H_r / \Delta t \qquad (1).$$

In equation (1) ΔH_r is enthalpy of the dehydration reaction, x_j is the weight percentage of H_2O released from the rock and Δt is the time over which dehydration occurs. Table 4.2 presents the enthalpies of some major chlorite-and muscovite-consuming reactions that characterize prograde greenschist and lower-amphibolite facies metamorphism in pelitic schists. Enthalpies were estimated from the data set of Holland and Powell (1990). The average heat of reaction is ~85 kJ/mole H_2O (4722 kj/kg H_2O) at a temperature of 450 °C.

Hot aqueous fluids released by dehydration reactions in the underlying thickened crust advectively heat the overlying crust, although only to a minor degree (e.g. England and Thompson, 1984; Brady, 1989; Loovesfeld and Etheridge, 1990). The heat production from a single-pass (Wather and Wood, 1984), intergranular fluid flux in a unit volume of rock is

$$A_f = F \rho_f c_f \left(\frac{\partial T}{\partial z}\right) \qquad (2)$$

(e.g. Brady, 1989), where F is the fluid flux (m^3 fluid/m^2 s), ρ_f is the density of the fluid, c_f is the heat capacity of the fluid, and $\left(\frac{\partial T}{\partial z}\right)$ is the geothermal gradient. The heat consumed by endothermic dehydration reactions and the

Table 4.2. Heats of reaction for some major low-grade dehydration reactions.

SOME REPRESENTATIVE GREENSCHIST AND LOWER AMPHIBOLITE FACIES NET-TRANSFER DEHYDRATION REACTIONS	ΔH_r (j/mole H_2O)
daphnite + muscovite = annite + staurolite + quartz + fluid $31\ Mg_5Al_2Si_3O_{10}(OH)_2 + 41\ KAl_3Si_3O_{10}(OH)_2 = 41\ KFe_3AlSi_3O_{10}(OH)_2 + 8\ Fe_2Al_9Si_{3.75}O_{22}(OH)_2 + 33\ SiO_2 + 108\ H_2O$	$\Delta H_r = 102989.82 - 30.41\ T\ (°C)$
clinochlore + muscovite + quartz = pyrope + phlogopite + fluid $3\ Mg_5Al_2Si_3O_{10}(OH)_2 + KAl_3Si_3O_{10}(OH)_2 + 3\ SiO_2 = 4\ Mg_3Al_2Si_3O_{12} + KMg_3AlSi_3O_{10}(OH)_2 + 12\ H_2O$	$\Delta H_r = 97834.43 - 24.50\ T(°C)$
daphnite + muscovite + quartz = almandine + annite + fluid $3\ Fe_5Al_2Si_3O_{10}(OH)_2 + KAl_3Si_3O_{10}(OH)_2 + 3\ SiO_2 = 4\ Fe_3Al_2Si_3O_{12} + KFe_3AlSi_3O_{10}(OH)_2 + 12\ H_2O$	$\Delta H_r = 91939.68 - 19.22\ (°C)$

NOTE: Heats of reactions were estimated with the data set of Holland and Powell (1990).

approximate maximum heat advected by fluids released from dehydration reactions are of the same order of magnitude as the uncertainty in A_r and, consequently, have a small effect on the thermal models. For example, in several of the models presented below, peak metamorphism occurs ~40 million years after thickening. If a 10 km column of pelitic crust releases ~5 weight % H_2O, the maximum flux F at the top of the column will be 10^{-12} m^3 fluid/m^2 s. At this fluid flux, a geothermal gradient of 45 °C/km, and a value of $\rho_f c_f = 3.5 \times 10^6$ j/m^3K (Brady, 1989), the rate of heat production is ~ 0.2 $\mu W/m^3$. If a unit volume of rock is dehydrated by 12 % volume (5 weight %, Walther and Orville, 1982) over a period of 40 million years, the rate of heat absorption is -0.4 $\mu W/m^3$. Therefore, the heat source and heat sink are of the same magnitude but have opposite signs, so that each tends to cancel the effects of the other in the thermal model.

Crustal thickening results in lower crustal temperatures that substantially exceed the water-saturated granite solidus (e.g. England and Thompson, 1984; Lux et al., 1986). The heat of fusion H_f for a granite is approximately 200 kJ/kg (e.g. Spear and Peacock, 1989). The rate of heat absorbed by a unit volume of rock undergoing partial melting is

$$A_{h.f.} = -x_i \rho_r H_f / \Delta t, \qquad (3)$$

where x_i is the volume percentage of rock that is melted and Δt is the time span over which partial melting occurs in a unit volume of rock. The heat sink resulting from partial melting is modeled by assuming that 50% of the crust exceeding 650 °C is partially melted over a period of 50×10^6 years ($A_{h.f.}$ = - 0.17$\mu W/m^3$).

THE THERMAL MODEL

The numerical models that follow assume that the crust is instantaneously shortened in the direction parallel to the surface and extended normal to surface. The geotherm T(z) resulting from homogeneous thickening is modeled as

$$T(z) = T_o(z)T(\gamma z_{max})/T(z_{max}), \qquad (4)$$

where γ is the factor of crustal thickening and $T_o(z)$ is the pre-thickening geotherm. The initial geotherm $T_o(z)$ for the crust is estimated following England and Thompson (1984). The mantle geotherm is simply estimated as

$$T(z) = T(z_{moho}) + (z\text{-}z_{moho})Q_r/K_{mantle}, \qquad (5)$$

where K_{mantle} is the conductivity of the mantle lithosphere. Figure 4.3 shows examples of the geotherm before and after thickening. Geotherm C (Figure 4.3) is consistent with a heat producing layer with a thickness of 30 km (2D), and represents the steady-state geotherm that would result if no uplift and erosion occurred after homogeneous doubling of the crust.

The time-dependent heat conduction equation for a semi-infinite crustal block uplifted at an erosion rate of v and with a rate of heat production A_T ($A_r + A_f + A_{h.f.} + A_{h.r.}$) is

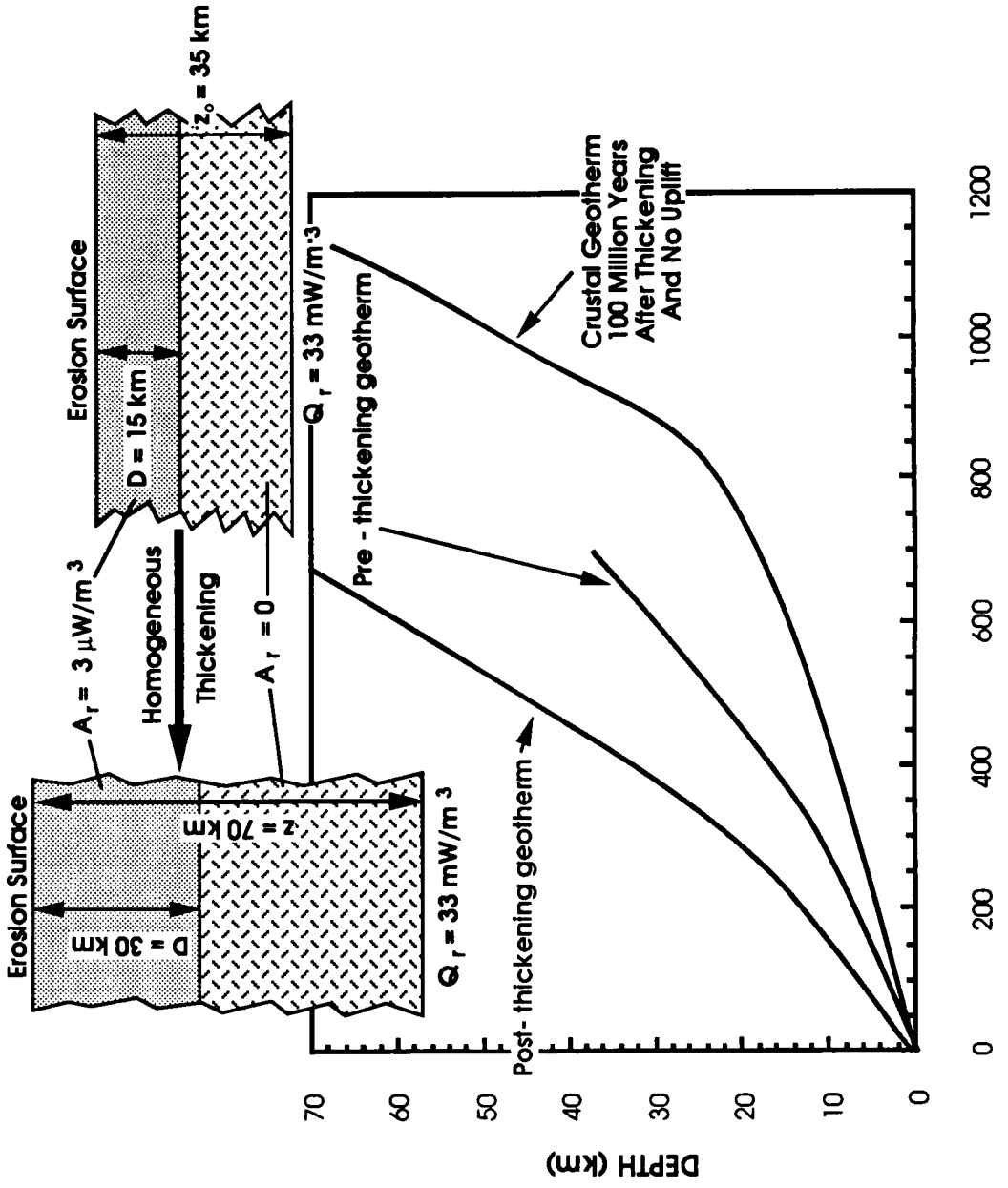
$$\frac{\partial T}{\partial t} = \kappa \frac{\partial^2 T}{\partial z^2} + \frac{A_T}{K} - v\frac{\partial T}{\partial z}. \qquad (6)$$

Where the effects of a cooling pluton are included in the model, the term

$$\kappa \frac{\partial^2 T}{\partial x^2} \qquad (6a)$$

is included with equation (6) to account for lateral heat transport. The specific heat and the thermal conductivity of the crust are assumed to be constant and to have the respective values 2.5×10^6 J/K m^3 and 2.25 ± 0.25 W/mK (Clark, 1969). The conductivity of the mantle is fixed at 3.5 W/mK

Figure 4.3. Temperature to depth diagram showing the geotherm before crustal thickening, after instantaneous homogeneous thickening, and 100 million years after thickening and no erosion.


Erosion Surface
D = 15 km
z_o = 35 km
A_r = 3 μW/m^3
Homogeneous
Thickening
A_r = 0
Q_r = 33 mW/m^{-3}
Pre - thickening geotherm
Crustal Geotherm
100 Million Years
After Thickening
And No Uplift
Erosion Surface
D = 30 km
z = 70 km
Q_r = 33 mW/m^3
Post- thickening geotherm
DEPTH (km)
0
10
20
30
40
50
60
70
0
200
400
600
800
1000
1200
T °C

(e.g. Sclater et al., 1980).

The boundary conditions are

$$T = 0\ ^{\circ}C \text{ at } z = 0$$

and

$$Q_r = -K\frac{\partial T}{\partial z} \text{ at the base of the lithosphere (-150 km).}$$

In instances where cooling magma was included in the model, the right-hand boundary was set at

$$T \rightarrow T_o \text{ as } x \rightarrow \infty,$$

and the left-hand boundary was assumed symmetrical to the right-hand boundary.

Equation (1), with the initial and boundary value conditions, was solved numerically with an explicit finite difference program (e.g. Abramowitz and Stegun, 1964). Program source codes, comparisons of numerical solutions with analytical solutions at simple boundary conditions, and tests for numerical stability are in Appendices A2 and A3, respectively.

CRUSTAL THICKENING AND SLOW UPLIFT

The thermal consequences of crustal thickening and erosion were treated in detail by England and Thompson (1984) for a broad range of physical conditions. Within the range of uplift rates (~0.35 mm/yr) and physical constants used in their numerical experiments, the sillimanite-andalusite transition was intersected only along retrograde PTt paths. PT paths from the Black Hills are prograde and clockwise.

The maximum temperature attained along a PTt path subsequent to crustal thickening is highly dependent upon the uplift rate. Uplift and

erosion thins the heat-producing layer and reduces the steady-state geothermal gradient that is approached by the exhuming crust. As the uplift rate increases, the convection term in equation (6) also decreases in value and is less than zero. The effect of changing the uplift rate between 0.35 and 0.015 mm/yr after homogeneous thickening is illustrated on Figure 4.4. The rate of radioactive heat production was set at 3.3 $\mu W/m^3$ and the heat flux at the base of the crust was set at 33 mW/m^2. At a uplift rate of 0.35 mm/yr, a maximum temperature of 350 °C is reached within 13 million years and the maximum temperature is approached along a nearly isothermal decompression path. In contrast, at an uplift rate of 0.015 mm/yr, a maximum temperature of 530 °C is reached in ~130 million years, and the maximum temperature is reached along a near-isobaric heating path that is followed by a clockwise cooling path.

Exhumation at a rate of 0.014 mm/yr after instantaneous and homogeneous crustal thickening would have resulted in temperature-to-depth ratios that were either consistent, or nearly consistent, with low-pressure, high-temperature metamorphism (Figure 4.5). The PTt paths shown in Figure 4.5 are consistent with A_r equals 3.3 $\mu W/m^3$ and Q_r = 33 mW/m^2. It is also assumed that 30% of the crust exceeding 650 °C is partially melted over a period of 40 million years. The paths are shown as gray bands which reflect the range in thermal conductivites (2.0 to 2.5 W/mK). The maximum temperatures are attained at unrealistically large amounts of time (125 to 161 Ma) after crustal thickening. However, triple-point conditions are reached 36 million years after crustal thickening, and sillimanite-grade conditions are reached at 54 million years. Pressures recorded in the Black

Figure 4.4. Decompression paths estimated for a section of crust initially at a depth of 14 km subsequent to homogeneous doubling of the crust initially 35 km thick. The four paths are shown to demonstrate the effect of decreasing the uplift rate from 0.35 mm/yr to 0.015 mm/yr. The heat flux at the base of the crust Q_r is 33 mW/m^2 and the radiogenic heat production A_r is fixed at 3.3 $\mu W/m^3$ to a depth of 15 km. As the decompression rate decreases, the heating phase of the PTt paths changes from near isothermal decompression to isobaric heating.

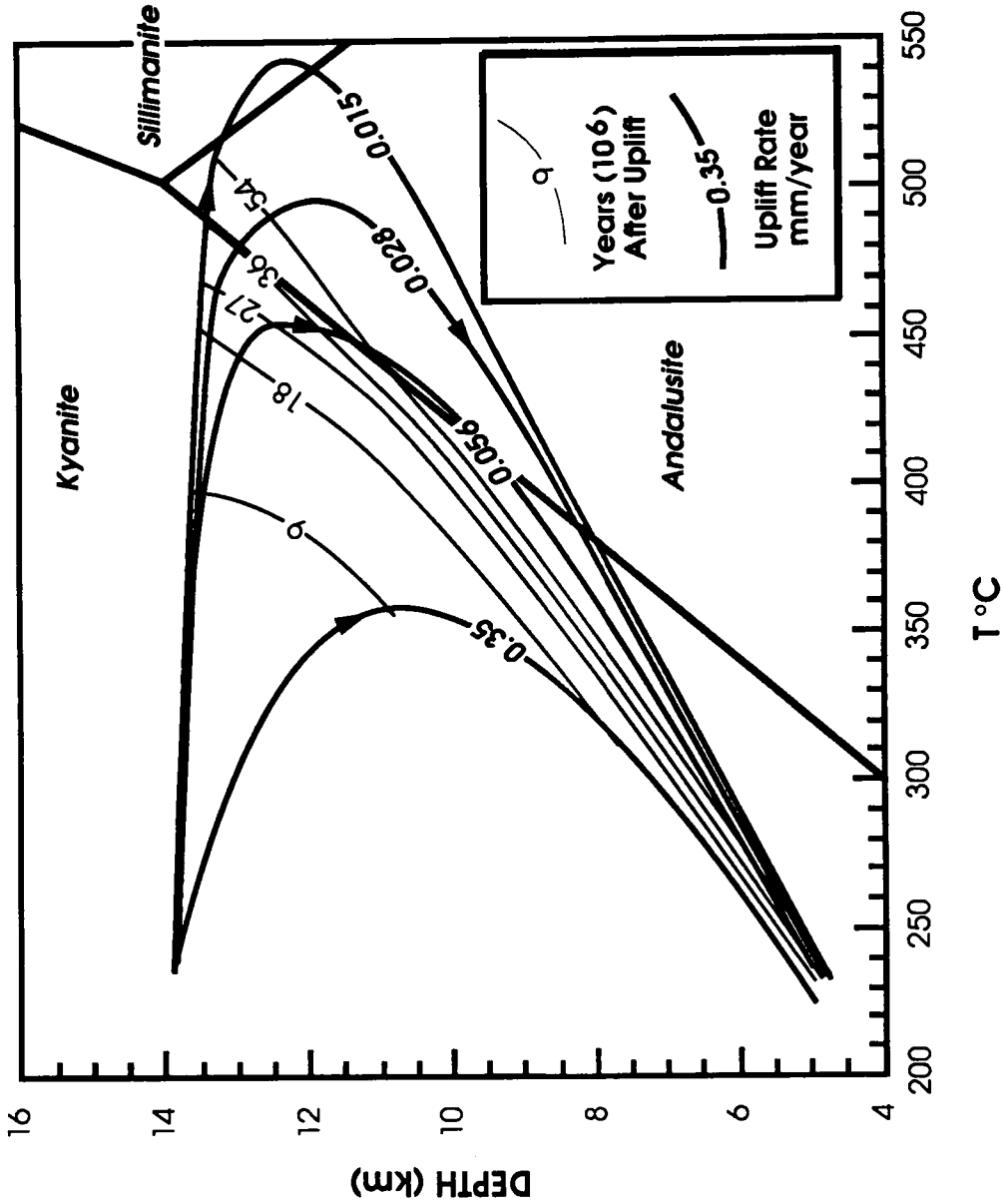
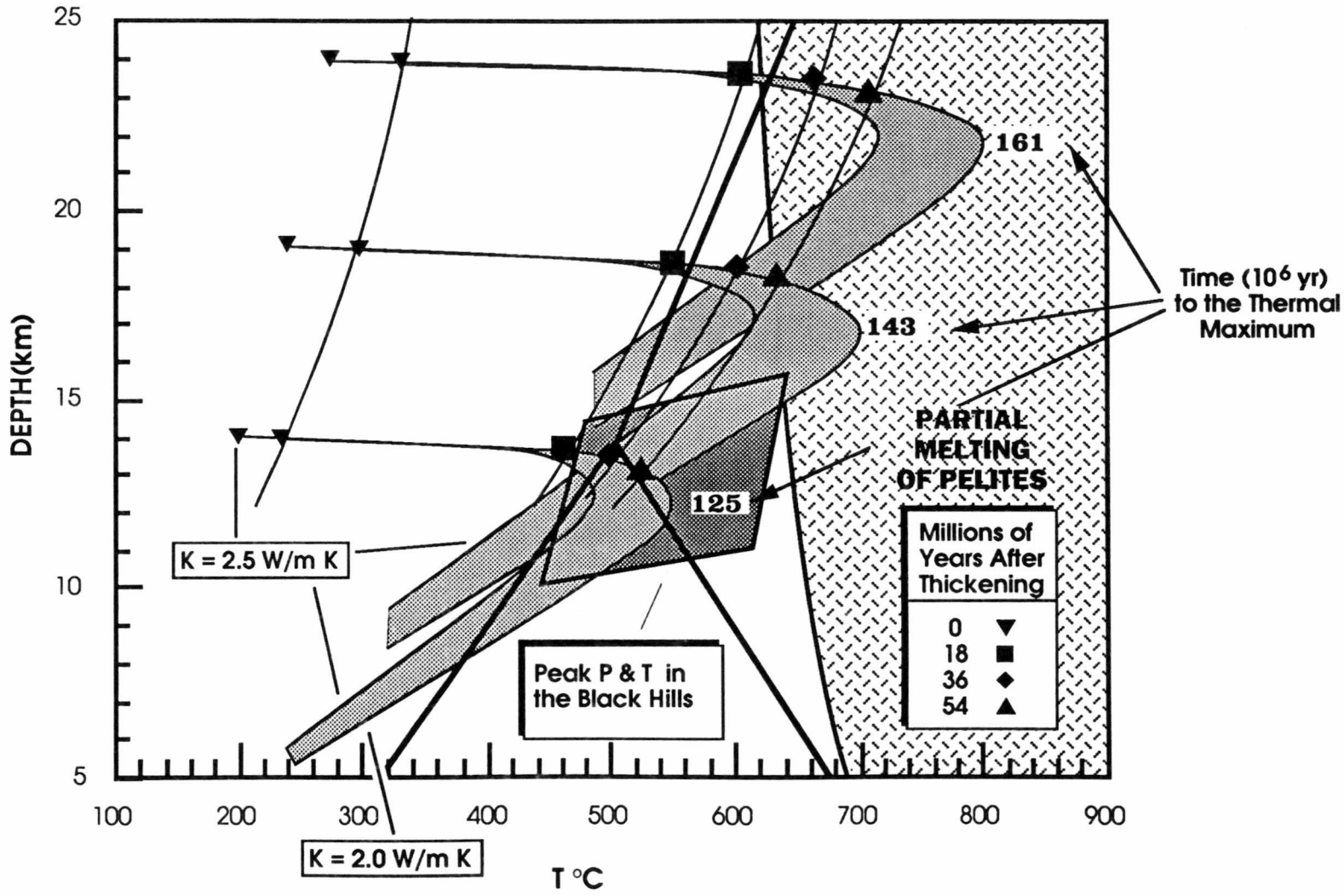

Sillimanite
Kyanite
Andalusite
Years (10⁶) After Uplift
Uplift Rate mm/year
0.35
0.28
0.056
0.015
54
36
27
18
9
DEPTH (km)
T °C
16
14
12
10
8
6
4
200
250
300
350
400
450
500
550

Figure 4.5. Decompression paths estimated for sections of crust initially at depths of 14, 19, and 24 km, after homogeneous doubling of a section of crust initially 35 km thick. The rate of uplift is 0.014 mm/yr, the mantle heat flux is fixed at 33 mW/m^2, and the radiogenic heat production is set at 3.3 $\mu W/m^3$. Portions of the crust exceeding 650 °C are assumed to absorb heat at a rate of -0.17 $\mu W/m^3$, consistent with 50% of a unit volume of rock melting over a period of 40×10^6 yr. The PTt paths are shown as shaded bands consistent with a range of thermal conductivites between 2.0 and 2.5 W/m K.

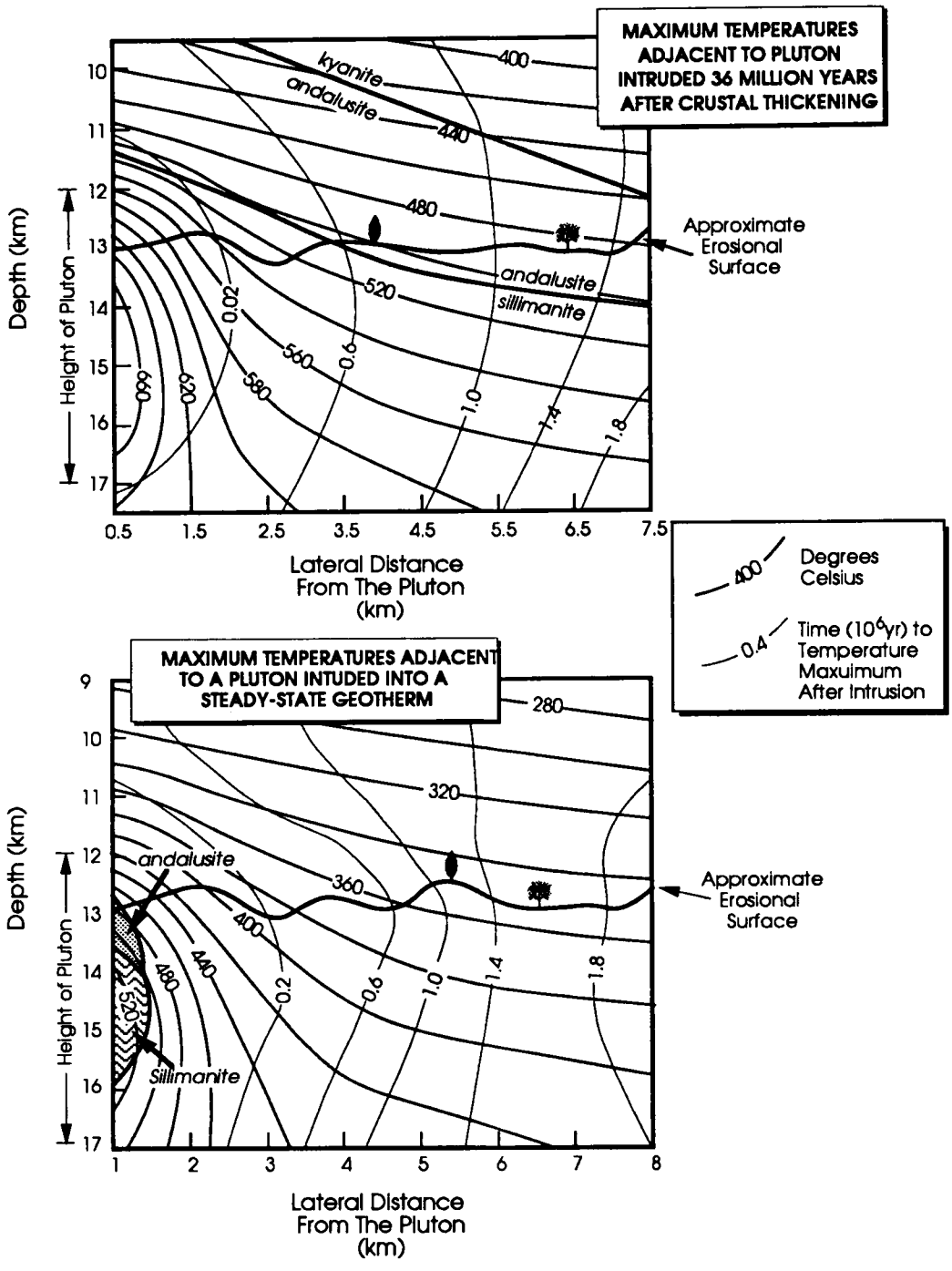

25
20
15
10
5
DEPTH(km)
100
200
300
400
500
600
700
800
900
T °C
161
143
125
Time (10^6 yr) to the Thermal Maximum
PARTIAL MELTING OF PELITES
Millions of Years After Thickening
0
18
36
54
Peak P & T in the Black Hills
K = 2.5 W/m K
K = 2.0 W/m K

Hills commonly indicate depths of 12 to 14 km; however, kyanite-bearing and many sillimanite-bearing rocks indicate depths of ~16 km (4.3 kbar).

Near-triple point metamorphism, and garnet- through staurolite-grade metamorphism (480 to 500 °C at ~3.0 kbar) can be attributed to slow decompression for ~36 million years, a mantle heat flux of 33 mW/m^2, and an internal heat production of ~3.3 $\mu W/m^3$. Sillimanite through sillimanite + K-feldspar grade conditions (≥ 510 °C) at depths of 13 to 14 km are not attained within a reasonable amount of time. However, sillimanite-grade conditions are attained at pressures ~4.0 kbar (15 km; Figure 4.5) within 36 million years after uplift, and the broad sillimanite zone in the southern portion of the Black Hills may be due to a gradual southward deepening (≥ 15 km) exposure. Higher pressures to the south of the granite are indicated by the presence of sporadic occurrences of kyanite south of sample location 1 (Redden, 1963). Kyanite-grade conditions similar to those recorded in the Bear Mountain dome (532 °C, 4.4) are attained 18 million years after uplift begins.

PTt paths (Figure 4.5) of pelitic schists initially at depths of 19 km exceed the temperature of the wet granite solidus at 36 million years after crustal thickening. Therefore, magma (Harney Peak granite) is generated at depths that are only ~5 km below the present level of crustal exposure. Magma transported from ≥ 5 km below the current level of crustal exposure (12 to 15 km) undoubtedly provided the remaining heat necessary for upper-sillimanite (staurolite-out) and sillimanite + K-feldspar grade temperatures. Figure 4.6a shows maximum temperatures adjacent to a pluton that is intruded 36 x 10^6 years after crustal thickening and slow uplift (0.014

Figure 4.6. Thermal profiles adjacent to a pluton. A) Maximum temperatures estimated for the country rock adjacent to a pluton intruded intantaneously at an initial temperature of 850 °C, and consisting of 50% melt. The pluton has a radius of 7 km and a thickness of 5 km and, the top of the pluton is set at a depth of 12 km. The pluton is intruded 36 Ma after the crust is homogeneously doubled from a thickness of 35 km, and uplifted at a rate of 0.014 mm/yr. The mantle heat flux is initially 33 mW/m^2 and the radiogenic heat production is 3.3 $\mu W/m^3$. The surrounding 2 km of country rocks absorb heat through endothermic dehydration reactions at a rate of -8 $\mu W/m^3$ for a period of 5×10^5 years. B) Maximum temperatures estimated for the country rock adjacent to a the same pluton shown in Figure 4.6A; however, the pluton is intruded into a steady-state geotherm (Q_r = 33 mW/m^2 and A_r = 3.3 $\mu W/m^3$). The surrounding 2 km of country rocks absorb heat through endothermic dehydration reactions at a rate of -16 $\mu W/m^3$ for a period of 5×10^5 years.


MAXIMUM TEMPERATURES ADJACENT TO PLUTON INTRUDED 36 MILLION YEARS AFTER CRUSTAL THICKENING
kyanite
andalusite
andalusite
sillimanite
Approximate Erosional Surface
Depth (km)
Height of Pluton
Lateral Distance From The Pluton (km)
Degrees Celsius
Time (10^6yr) to Temperature Maxuimum After Intrusion
MAXIMUM TEMPERATURES ADJACENT TO A PLUTON INTUDED INTO A STEADY-STATE GEOTHERM
andalusite
Sillimanite
Approximate Erosional Surface
Depth (km)
Height of Pluton
Lateral Distance From The Pluton (km)

mm/year). The isochrons on Figure 4.6 represent millions of years after granite emplacement. The granite has a radius of 7 km (Figure 4.1), a thickness of 5 km (Duke et al., 1991) and the top of the pluton is placed at a depth of 12 km. The magma is emplaced at a temperature of 850 °C and has a rate of radioactive heat production equal to 8.0 $\mu W/m^3$ (Table 4.1). The magma is assumed to consist of 50% melt and the latent heat of crystallization is released over a period of a half a million years ($A_{h.f.}$ = 17.0 $\mu W/m^3$). Schists that are adjacent to the pluton have already attained staurolite- to sillimanite-grade conditions before intrusion and much of the rock will have been dehydrated. Therefore, only 1 weight % dehydration is incorporated into the model and the surrounding 2 km of country rock are assumed to absorb heat through endothermic dehydration reactions at a rate of -8.0 $\mu W/m^3$ for half a million years.

There are several uncertain parameters associated with the results of the thermal model shown in Figure 4.6a; however, the results demonstrate the magnification of the distance between the pluton and isotherms after the geothermal gradient has been enhanced. (For comparison, Figure 4.6b shows the same pluton intruded into a steady-state geotherm where Q_r = 33 mW/m^3 and A_r =3.3 $\mu W/m^2$.) The intersection between the present erosional surface and isotherms in Figure 4.6a are remarkably similar to those observed along the northern flank of the Harney Peak granite (Figure 4.1). The model distribution of isotherms shown on Figure 4.6a indicate that amphibolite facies conditions extend over 7.5 km from the granite contact. Along the northern flank of the Harney Peak granite (Figure 4.1) the sillimanite isograd (~520 to 530 °C) is ~2 to 3 km from the granite contact.

The sillimanite-andalusite transition intersects the modern erosional surface (-13 km) at a distance of 3 to 4 km from the contact on Figure 4.6a. In contrast, note that unless the geotherm is enhanced prior to the intrusion of the Harney Peak granite, sillimanite- and andalusite-grade conditions will be restricted to distances that are ≤ 1.5 km from the granite contact (Figure 4.6b). The real staurolite isograd, which is approximately equivalent to the 480 °C isotherm, is located 7 to 15 km from the granite contact (Figure 4.1). The model 480 °C isotherm (Figure 4.6a) intersects the -13 km surface at 7.5 km from the granite contact. Garnet-grade conditions in the Black Hills occurred at temperatures between 400 °C and 480 °C (Helms and Labotka, 1991a; 1991b). The garnet zone in the Black Hills also extends ~25 of kilometers north of the staurolite isograd. The model results (Figure 4.6a) indicate that garnet-grade conditions should extend tens of kilometers from the granite contact. Model sillimanite-grade conditions extend in the subsurface in Figure 4.6a at shallow levels (~14 km) for several kilometers from the granite contact; therefore, the broad sillimanite zone south of the Harney Peak granite may reflect only slightly deeper sections of the crust.

DISCUSSION AND CONCLUSIONS

Low-pressure, high-temperature metamorphism and anatexis in the Black Hills can be modeled by crustal thickening followed by slow uplift for a time ≥ 36 million years. Crustal thickening followed by slow uplift enhances the geothermal gradient sufficiently for upper greenschist- to lower amphibolite-facies conditions to be attained at a depth of -12 to 13 km (~3.3 kbar) and sillimanite grade conditions at depths of -14 to 15 km (~3.8 kbar). Temperatures exceeding the water-saturated granite solidus are attained at

depth of 19 km within 36 million years. Emplacement of anatectic melts after enhancement of the geotherm provides the additional heat necessary for sillimanite + K-feldspar conditions (≥ 600°).

The model presented above accounts for near-isobaric, prograde PT paths and clockwise cooling paths inferred from reaction-zoned garnets and reaction textures (Helms and Labotka, 1991), respectively. It is also consistent with peak metamorphism occurring after polyphase folding and crustal thickening. The heat source maintains amphibolite facies conditions for times on the same order of magnitude inferred from homogeneous garnets in the Black Hills (~10^7 years; Helms and Labotka, 1991b).

The major detraction of this model is the amount of time (10^9 years) required for the crust to return to a normal thickness of 40 ± 10 km. However, it is only necessary to maintain a rate of slow uplift (0.014 mm/yr) for ~36 million years for the temperatures in the upper crust to attain staurolite- to andalusite-grade conditions (Figure 4.4 and 4.5). This amount of time is of the order of magnitude associated with continental collision and orogenesis (e.g. Gansser, 1979), and is also similar to the lag time (~20 x 10^6 years) believed to exist between crustal thickening and rapid uplift (~1 to 0.35 mm/yr; Oxburgh and Turcotte, 1974; Richardson and England, 1979; England and Thompson, 1984).

The preceding model provides a simple mechanism to explain regional low-pressure, high-temperature metamorphism and crustal anatexis. The model relies on values of heat production estimated from the measured concentrations of radiogenic isotopes from major lithologic units and on a mantle heat flux that is consistent with a modern stable craton. In several

low-pressure, high-temperature terrains there is a correlation between metamorphic grade and the proximity of syn- to post-tectonic granitic plutons. Commonly, however, the distance between the pluton and isotherms far exceeds the values expected in a simple contact metamorphic aureole (e.g. Holdaway et al., 1988; Helms and Labotka, 1991a). This relationship strongly suggests that the geothermal gradient is enhanced prior to the emplacement of the granite. The geotherm may be enhanced either by radiogenic self-heating (Figure 4.6) or by an increased heat flux at the base of the lithosphere or crust (e.g. Bird, 1978; Labotka and Albee, 1988; Lovesfeld, 1989). The model presented above obviates the need for an enhanced mantle heat flux as a cause of regional low-pressure, high-temperature metamorphism. This model certainly does not preclude the possiblity of processes that would increase the mantle heat flux, such as lithospheric thinning (Houseman et al., 1980) or lithospheric delamination (Bird, 1978); however, it is not necessary to invoke these models to explain metamorphism in the Black Hills.

Low-pressure, high-temperature terrains are not restricted to any particular time in Earth history; however, practically all Early Proterozoic metamorphic terrains are characterized by anatexis and low-pressure, high-temperature metamorphism (Windely, 1978). The radiogenic heat production estimated from measured values of U, Th, and K in lithologies from the Black Hills, is ~30 % higher in the Early Proterozoic (1.8 to 1.7 Ga) than in the Cenozoic. For example, the mica schist unit has a radiogenic heat production value of 3.3 $\mu W/m^3$ at 1.7 Ga and 2.5 $\mu W/m^3$ at the present. Although the the thermal history of the mantle remains uncertain (e.g Davies, 1980), the residual heat flux Q_r is due in part to the decay of

radiogenic isotopes; therefore, the mantle flux was undoubtedly higher at 1.7 Ga than at the present. I have chosen to use a modern estimate of the mantle heat flux in the thermal models presented in Figure 4.5 and 4.6 as a conservative lower limit; however, if the model shown in Figure 4.5 is estimated with Q_r = 40 mW/m^2 (30 % higher), triple point conditions are attained in 18 million years instead of 36 million years after crustal thickening. The somewhat higher geothermal gradient during the Early Proterozoic may account for the commonplace occurrence of Early to Middle Proterozoic (1.8 to 1.6 Ga) high-temperature, low-pressure terrains.

CHAPTER V

CONCLUSIONS

The Late Archean to Early Proterozoic terrain exposed in the Black Hills of South Dakota, records a history of deformation, metamorphism, and igneous activity extending from ~2.5 to 1.7 Ga. Metamorphism began during crustal thickening; however, maximum temperatures were attained after crustal thickening during a regional low-pressure high-temperature event that was partly synchronous with the emplacement of the Harney Peak granite at 1.7 Ga. A broad garnet zone extends ~25 km southward from an unconformity between Cambrian and Early Proterozoic lithologies, to an east-trending staurolite isograd. Isograds mapped in the terrain include the first appearance of staurolite + biotite, andalusite + biotite, sillimanite, sillimanite + biotite + garnet, and sillimanite + K-feldspar. In the extreme western exposure of the terrain, kyanite + biotite occurs instead of andalusite + biotite. The staurolite and andalusite zones are approximately 5 km to 10 km wide and are bounded to the south by a broad sillimanite zone. Sillimanite-zone schists extend ~30 km southward before dipping beneath the unconformity below Cambrian lithologies. Sillimanite + K-feldspar conditions were reached locally along the southern flank of the Harney Peak granite. Geobarometry indicates that metamorphism occurred between 2.0 and 4.4 kbar. Temperature increased from 469-500 °C in the garnet zone to 528-555 °C in sillimanite zone on the northern flank of the Harney Peak granite. Higher temperatures are recorded along the southern flank of the granite in the sillimanite + biotite + garnet zone (585 °C) and in the sillimanite + K-feldspar zone (≤ 662 °C). The distributions of isograds, isotherms, and major fold axes indicate that the Harney Peak granite was at the locus of a regional thermal high and that doming during granite

emplacement locally deformed preexisting isograds and fold axes.

Pressure-temperature paths based on compositionally zoned garnets from garnet-grade and staurolite-grade rocks indicate that prograde metamorphism from 400 °C to 500 °C occurred at almost isobaric conditions (± 0.5 bars). PT paths based on compositionally zoned garnets also have a clockwise orientation. Because of volume diffusion and retrograde decompression, prograde PT paths could not be determined from sillimanite and sillimanite + K-feldspar zone garnets; however, reaction textures in these rocks strongly suggest clockwise decompression and cooling paths. Homogenization of garnets at a temperature of ~565 °C indicates heating and cooling occurred at a minimum of ~4×10^7 years.

Low-pressure, high-temperature metamorphism in the Black Hills followed crustal thickening associated with continental collision and the suturing of the Archean-aged Superior and Wyoming provinces. One- and two-dimensional numerical models were constructed to examine the thermal consequences of rapid homogeneous crustal thickening and slow uplift. The uplift rate (0.014 mm/year) was estimated from the amount of uplift determined from geobarometry (14 to 16 km) and the time interval between peak metamorphism at 1.7 Ga and the age of the Cambrian (~0.6 Ga) lithologies unconformably overlying the Proterozoic crystalline complex. This value requires that uplift was constant and continuous. At an uplift rate of 0.014 mm/year, low-pressure, high-temperature metamorphism occurs with a moderate mantle heat flux (33 mW/m^2) and a measured crustal radiogenic heat production rate of 3.3 $\mu W/m^3$. The value of the mantle heat flux is consistent with present-day reduced heat flux measurements. The rate of radiogenic heat production was estimated from

the concentration of U, Th, and K in major lithologic units from the Black Hills. Estimated PTt paths are consistent with nearly isobaric heating, clockwise decompression, and with a thermal perturbation that lasts on the order of 10^7 years. The common occurrence of Early Proterozoic low-pressure, high temperature terrains may in part be a result of higher radiogenic heat-production values in the upper crust and perhaps the mantle.

REFERENCES CITED

Abramowitz, M., and Stegun, I. A., 1964, Handbook of Mathematical Functions with Formulas, Graphs, and Mathematical Tables: National Bureau of Standards Applied Mathematicas Series, v. 55., 1046 pp.

Albee, A.L., 1965, A petrogenetic grid for the Fe-Mg silicates of pelitic schists: American Journal of Science, v. 263, p. 512-536.

Brady, J. B., 1988, The Role of volatiles in the thermal history of metamorphic terranes: Journal of Petrology, v. 29, p. 1187-1213.

Barton, M. D., and Hanson, R. B., 1989, Magmatism and the development of low-pressure metamorphic belts: Implications from the western United States and thermal modeling: Geological Society of America Bulletin, v. 101, p. 1051-1065.

Berman, R. G., 1988, Internally-consistent thermodynamic data for minerals in the system Na_2O-K_2O-CaO-MgO-FeO-Fe_2O_3-Al_2O_3-SiO_2-TiO_2-H_2O-CO_2: Journal of Petrology, v. 29, p. 445-522.

Bowers, T.S., and Helgeson, H. C., 1983, Calculation of the thermodynamic and geochemical consequences of non-ideal mixing in the system H_2O-CO_2-NaCl on phase relations in geologic systems: Equations of state for H_2O-CO_2-NaCl fluids at high pressures and temperatures: Geochemica et Cosmochimica Acta, v. 47, p. 1247-1275.

Braile, L. W., Hinze, W. J., von Frese, R. R. B., Kelle, R. G., 1989, Seismic properties of the crust and uppermost mantle of the conterminous United States and adjacent Canada: Geological Society of America Memoir 172, p. 655-680.

Burnham, C. W., Holloway, J. R., and Davis, N. F., 1969, Thermodynamic properties of water to 1000 °C and 10,000 bars: Special Paper Geological Society of America 132.

Carpenter, M. A. and Ferry, J. M., 1984, Constraints on the thermodynamic mixing properties of plagioclase feldspars: Contributions to Mineralogy and Petrology, v 87, p. 138-148.

Carslaw, H. S. and Jaeger, J. C., 1959, Conduction of Heat in Solids, 2nd edition, Oxford: Clarendon Press, p. 510.

Chamberlain, C. P., 1986, Evidence for repeated folding of isotherms during regional metamorphism: Journal of Petrology, v. 17, p. 63-89.

Chatterjee, N. D., 1971, The upper stability limit of the assemblage paragonite + quartz and its natural occurrences: Contributions to Mineralogy and Petrology, v 34, p. 288-303.

Chatterjee, N. D., and Johannes, W., 1974, Thermal stability and standard thermodynamic properties of synthetic 2M1-muscovite, $KAl_2AlSi_3O_{10}(OH)_2$: Contributions to Mineralogy and Petrology, V. 48, p. 89-114.

Chatterjee, N. D., and Froese, E., 1975, A thermodynamic study of the psuedobinary join muscovite-paragonite in the system $KAlSi_3O_8$-$NaAlSi_3O_8$-Al_2O_3-SiO_2-H_2O: American Mineralogist, v. 60, p. 985-993.

Cygan, R. T., and Lasaga, A. C., 1985, Self-diffusion of magnesium in garnet: American Journal of Science, v. 285, p. 329-350.

Cressey, G., Schmid, R., and Wood, B. J., 1978, Thermodynamic properties of almandine-grossular garnet solid solutions: Contributions to Mineralogy and Petrology, v. 67, p. 397-404.

Davis, G. F., 1980, Thermal histories of convective earth models and constraints on radiogenic heat production in the Earth: Journal of Geophysical Researh, v. 85, p. 2517-2530.

Dewey, J. F., and Burke, K. C. A., 1973, Tibetan, Variscan, and Precambrian Basement Reactivation: Products of Continental Collision: Journal of Geology, v. 81, p. 683-692.

Dewitt, E., Redden, J. A., Wilson, A. B., and Buscher, D., 1986, Mineral Resource Potential and Geology of the Black Hills National Forest, South Dakota and Wyoming: U.S. Geological Survey Bulletin 1580. p.135.

Dewitt, E., Redden, J. A., Buscher, D., and Wilson, A. B, 1989, Geologic map of the Black Hills area, South Dakota and Wyoming: U.S. Geological Survey Miscellaneous Investigations Series, Map I-1910, scale 1:250,000.

DeYoreo, J.J., Lux, D. R., Guidotti, C.V. and Decker, E.R., 1986, The role of plutonism in the formation of low-pressure metamorphic belts: EOS Transactions of the American Geophysical Union, v. 67, p. 370.

Duke, E. F., Redden, J. A., and Papike, J. J., 1988, Calamity Peak layeredgranite-pegmatite complex, Black Hills, South Dakota: Part I. Structure and Emplacement. Geological Society of America Bulletin, v. 100, p. 825-840.

Duke, E. F., Shearer, C. K., Redden, J. A., and Papike, J. J. , 1991, Proterozoic Granite-Pegmatite Magmatism, Black Hills, South Dakota: Structure and Geochemical Zonation, in Lewry, J. F., and Stauffer, M. R., eds., The Trans-Hudson orogen: Geological Society of Canada Special Paper (in Press).

England, P. C., 1978, Some thermal considerations of Alpine metamorphism, past, present, and future: Tectonophysics, v. 46, p. 21-40.

England, P. C. and Thompson, A. B., 1984, Pressure-temperature-time paths of regional metamorphism I. Heat transfer during the evolution of regions of thickened continental crust: Journal of Petrology, v. 25, p. 894-928.

Ferry, J.M. and Spear, F.S., 1978, Experimental calibration of the partitioning of Fe and Mg between biotite and garnet: Contributions to Mineralogy and Petrology, v. 66, p. 113-117.

Fletcher, C. J. N. and Greenwood, H. J., 1979, Metamorphism and structure of the Penfold Creek area, near Quensel Lake, British Colombia: Journal of Petrology, v. 20, p. 743-794.

Ganguly, J. and Saxena, S. K., 1984, Mixing properties of aluminosilicate garnets: constraints from natural and experimental data, and application to geothermo-barometry: American Mineralogist, v. 69, p. 88-97.

Ganguly, J. and Saxena, S. K., 1985, Mixing properties of aluminosilicate garnets: constraints from natural and experimental data, and application to geothermo-barometry: clarifications: American Mineralogist, v. 709, p. 1320.

Gansser, A., 1983, The morphogenic phase of mountain building, Hsu, K. J. ed., Mountain Building Processes, Academic Press, New York, N. Y., p. 221-228.

Ghent, E. D. and Stout, M. Z., 1981, Geobarometry and geothermometry of the plagioclase-biotite-garnet-muscovite assemblage: Contributions to Mineralogy and Petrology, v. 76, p. 92-97.

Gosselin, D. C., Papike, J. J., Zartman, R. E., Peterman, Z. E., and Laul, J. C., 1988, Archean rocks of the Black Hills, South Dakota: Reworked basement from the souther extension of the Trans-Hudson orogen: Geological Society of America Bulletin, v. 100, p. 1244-1259.

Grambling, J. A., Williams, M. L., Smith, R. F., and Mawer, C. K., 1989, The role of crustal extension in the metamorphism of Proterozoic rocks in northern New Mexico: Geological Society of America Special Paper 235, p. 87-110.

Griffen, D. T., and Ribbe, P. H., 1973, The crystal chemistry of staurolite.American Journal of Science, v. 273A, p. 479-495.

Guidotti, C. V., 1984, Micas in metamorphic rocks, In Bailey, S. W., ed., Micas: Mineralogical Society of America, Reviews in Mineralogy, v. 13, p. 299-356.

Helms, T. S. and Labotka, T. C., 1990, Thermal evolution of a regional low-pressure, high-temperature terrain, Black Hills, S. D.: Geological Society of America Abstracts with Programs, v. 22, p. A31.

Helms, T. S., and Labotka, T. C., 1991, Petrogenesis of early Proterozoic pelitic schists of the southern Black Hills, South Dakota: constraints on regional low-pressure metamorphism: Geological Society of America Bulletin (in press).

Helms, T. S. and Labotka, T. C., 1991, Tectonothermal history of Early Proterozic pelitic schists of the Black Hills, S. D.: Journal of Metamorphic Geology (in review).

Hodges, K. V., and Spear, F. S., 1982, Geothermometry, geobarometry, and the Al_2SiO_5 triple point at Mt. Moosilauke, New Hampshire: American Mineralogist, v. 67, p. 1118-34.

Holdaway, M.J., 1971, Stability of andalusite and the aluminum silicatediagram: American Journal of Science, v. 271, p. 97-131.

Holdaway, M. J., Dutrow, B.L., and Hinton, R.W., 1988, Devonian and Carboniferous metamorphism in west-central Maine: The muscovite-almandine geobarometer and the staurolite problem revisited: American Mineralogist, v. 73, p. 20-47.

Hollister, L. S., 1966, Garnet zoning: an interpretation based on the Rayleigh fractionation model: Science, v. 154, p. 1647-1651.

Holland, T. J. B., and Powell, R., 1985, An internally consistent thermodynamic dataset with uncertainties and correlations: 2. Data and results: Journal of Metamorphic Geology, v. 3, p. 343-370.

Holland, T. J. B., and Powell, R., 1990, An enlarged and updated internally consistent thermodynamic dataset with uncertainties and correlations: the system MgO-MnO-FeO-Fe_2O_3-Al_2O_3-TiO_2-SiO_2-C-H_2-O_2: Journal of Metamorphic Geology, v. 8, p. 89-124.

Houseman, G. A., McKenzie, D. P., and Molnar, P., 1981, Covective instability of a thickened boundary layer and its relevance for thermal evolution of continental convergent belt: Journal of Geophysical Research, v. 86, p. 6115-6132.

Indares, A, and Martignole, J., 1985, Biotite-garnet geothermometry in the granulite facies: the influence of Ti and Al in biotite: American Mineralogist, v. 70, p. 272-278.

Kleinkopf, M. D., and Redden, J. A., 1975, Bouger gravity, areomagnetic, and generalized geologic maps of part of the Black Hills of South Dakota and Wyoming: U. S. Geologic Survey Geophysical Investigations Map GP-903, scale 1:250,000.

Koziol, A. M., 1990, Activity-composition relationships of binary Ca-Fe and Ca-Mn determined by reversed, displaced equilibrium experiments: American Mineralogist, v. 75, p. 319-327.

Koziol, A. M. and Newton, R. C., 1988, Redetermination of the anorthite breakdown reaction and improvement of the plagioclase-garnet-Al_2SiO_5-quartz geobarometer: American Mineralogist, v. 73, p. 216-223.

Labotka, T. C., 1981, Petrology of an andalusite-type regional metamorphic terrain, Panamint Mountains, California: Journal of Petrology, v. 22, p. 261-296.

Labotka, T. C., and Albee, A. L., 1988, Metamorphism and tectonics of the Death Valley, California, In Ernst, W. G., ed., Metamorphism and crustal evolution, western conterminous United States, Rubey Volume VII: Englewood Cliffs, New Jersey, Prentice Hall, p. 714-736.

Lachenbruch, A. H., 1970, Crustal temperature and heat production: implications for the linear heat flow relation: Journal of Geophysical Research, v. 75, p. 3291-3300.

Lang, H. M., and Rice, J.M., 1985, Regression modeling of metamorphic reaction in metapelites, Snow Peak, Northern Idaho: Journal of Petrology, v. 24, p. 857-887.

Lasaga, A. C., Richardson, S. M., and Holland, H. D., 1977, The mathematics of cation diffusion and exchange between silicate minerals during retrograde metamorphism, In: Saxena, S. K., and Bhattacharji, S., eds., Energetics in Geological Processes: New York, Springer-Verlag, p. 353-388.

Loosveld, R. J. H., 1989, The synchronism of crustal thickening and low-pressure facies metamorphism in the Mount Isa Inlier, Australia 2. Fast convective thinning of the mantle lithosphere during crustal thickening: Tectonophysics, v 165, p. 191-218,

Loosveld, R. J. H., and Etheridge, M. A., 1990, A model for low-pressure metamorphism during crustal thickening: Journal of Metamorphic Geology, v. 8, p. 257-267.

Lovering, T. S., 1935, Theory of heat conduction applied to geological problems: Geological Society of America Bulletin, v. 46, p. 69-94.Lux, D. R., DeYoreo, J. J., Guidotti, C. V., and Decker, E. R., 1986, Role of plutonism in low-pressure metamorphic belt formation: Nature, v. 232, p. 794-797.

Lux, D. R., DeYoreo, J. J., Guidotti, C. V., and Decker, E. R., 1986, Role of plutonism in low-pressure metamorphic belt formation: Nature, v. 232, p. 794-797.

McCamy, K., and Meyer, R. P., 1964, A correlation method of apparent velocity measurements: Journal of Geophysical Research, v. 69, p. 691-699.

Molnar, P., and Tapponnier, P., 1975, Tectonics of Asia: Cosequences and implications of a continental collision: Science, v. 189, p. 419-426.

Newton, R. C., and Haselton, H.T., 1981, Thermodynamics of the garnet-plagioclase-Al_2SiO5-quartz geobarometer, In Newton, R. C., Navrotsky, A., and Wood, B. J., eds, Thermodynamics of Minerals and Melts. New York: Springer-Verlag, p. 131-147.

Newton, R. C., 1987, Thermodynamic analysis of phase equilibria in simple mineral systems: in I. S. E. Carmichael and H. P. Eugster, eds. Thermodynamic modeling of geological materials: minerals, fluids, and melts, Mineralogical Society of America, Reviews in Mineralogy, v. 17, p. 1-28.

Orville, P. M., 1972, Plagioclase cation exchange equilibria with aqueous chloride solution: results at 700 °C and 2000 bar in the presence of quartz: American Journal of Science, v. 272, p. 234-272.

Oxburgh, E. R., and Turcotte, D. L., 1974, Thermal gradients and regional metamorphism in overthrust terrains with special reference to the Eastern Alps: Schweiz Miner Petrogr Mitt, v. 54, p. 641-662.

Pigage, L. C., 1976, Metamorphism of the Settler Schist, southwest of Yale, British Colombia: Canadian Journal of Earth Science, v. 3, p. 405-421.

Pigage, L. C., and Greenwood, H. J., 1982, Internally consistent estimates of pressure and temperature: The staurolite problem. American Journal of Science, v. 282, p. 943-969.

Ratte, J. C., 1986, Geologic map of the Medicine Mountain quadrangle, Pennington county South Dakota, U. S. Geologic Survey Miscellaneous Geologic Map I-1654, scale 1-24,000.

Ratte, J. C., and Wayland, R. G., 1969, Geology of the Hill City quadrangle, Pennington County, South Dakota- A prelimenary report: U. S. Geological Survey Bulletin 1271-B, 14 p.

Redden, J. A., 1963, Geology and Pegmatites of the Fourmile quadrangle, Black Hills, South Dakota: U. S. Geological Survey Professional Paper 297-D, p. 199-291.

Redden, J. A., 1968, Geology of the Berne quadrangle, Black Hills, South Dakota: U.S. Geologic Survey Professional Paper 297-F. p. 343-408.

Redden, J. A., and Norton, J. I., 1975, Precambrian geology of the Black Hills, in U.S. Congress, Senate Committee on Interior and Insular Affairs, Mineral and water resources of South Dakota: U.S. 94th Congress, 1st session, p. 21-28.

Redden, J.A., Norton, J.J., and McLaughlin, R.J., 1982, Geology of the Harney Peak Granite, Black Hills, South Dakota,: U. S. Geological Survey Open-File Report, 82-481, p. 18.

Redden, J. A., Peterman, Z. E., Zartman, R. E., and DeWitt, E., 1991, U-Th-Pb geochronology and prelimanary interpretation of Precambrian tectonic events in the Black Hills, South Dakota: in Lewry, J. F., and Stauffer, M. R., eds., The Trans-Hudson orogen: Geological Society of Canada Special Paper (in Press).

Reid, M. J., Gancarz, A. J., and Albee, A. L., 1973, Constrained least-squares analysis of petrologic problems with application to lunar sample 12040: Earth and Planetary Science Letters, v. 12, p. 443-445.

Richardson, S. W., and England, P. C., 1979; Metamorphic consequences of eclogite production in overthrust orogenic zones: Earth and Planetary Science Letters, v. 42, p. 183-190.

Riley, G. H., 1970, Isotopic discrepancies in zoned pegmatites, Black Hills, South Dakota. Geochemica et Cosmochemica Acta, v. 34, p. 713-725.

Roy, R. F., Blackwell, D. D., and Birch, F., 1968, Heat generation of plutonic rocks and continental heat flow provinces: Earth and Planetary Science Letters, v. 5., p. 1-12.

Rumble, D., III, 1976, The use of mineral solid solutions to measure chemical potential gradients in rocks: American Mineralogist, v. 61, p. 1167-1174.

Saxena, S. K., and Ribbe, P. H., 1972, Activity-composition relations in feldspars: Contributions to Mineralogy and Petrology, v. 37, p. 131-138.

Scalter, J. G., Jaupart, C., and Galson, D., 1980, The Heat flow through oceanic and continental crust and the heat loss of the Earth: Reviews of Geophysics and Space Physics, v. 18, p. 269-311.

Selverstone, J., Spear, F. S., Franz, G., and Morteani, G., 1984, High pressure metamorphism in the SW Tauern window, Austria: P-T paths from hornblende-kyanite-staurolite schists. Journal of Petrology, v. 25, p. 501-531.

Sleep, N. H., 1979, A thermal constraint on the duration of folding with reference to Acadian geology, New England. Journal of Geology, v. 87, p. 583-589.

Spear, F. S., 1988, Metamorphic fractional crystallization and internal metasomatism by diffusional homogenization of zoned garnets: Contributions to Mineralogy and Petrology, v. 99, p. 507-517.

Spear, F. S., Ferry, J. M., and Rumble, D., III, 1982, Analytical formulation of phase equilibria: the Gibbs' Method, in Ferry, J. M., ed., Characterization of Metamorphism through Mineral Equilibria: Mineralogical Society of America, Reviews in Mineralogy, v. 10, p. 105-152.

Spear, F. S., and Rumble, D, 1986, Pressure, temperature, and structural evolution of the Orfordville Belt, west-central New Hampshire: Journal of Petrology, v. 27, p. 1071-1093.

Spear, F. S., and Selverstone, J., 1983, Quantitative P-T paths from zoned minerals: Theory and applications: Contributions to mineralogy and Petrology, v. 83, p. 348-357.

Spear, F. S., and Menard, T., 1989, Program GIBBS: A generalized Gibbs method algorithm: American Mineralogist, v. 74, p. 942-943.

Spear, F. S. and Peacock, S. M., 1989, Metamorphic Pressure-Temperature-Time Paths; American Geophysical Union Short Course in Geology, v. 7, p. 102.

St-Onge, M. R., 1987, Zoned poikiloblastic garnets; P-T paths and syn-metamorphic uplift through 30 km of structural depth, Wopmay Orogen, Canada: Journal of Petrology, v. 28, p. 1-22.

Thompson, A. B., 1976, Mineral reactions in pelitic rocks: I. Prediction of P-T-X(Fe-Mg) phase relations: American Journal of Science, v. 276, p. 401-424.

Thompson, A. B., and, England, P. C., 1984, Pressure-temperature-time Paths of regional metamorphism II.Their inference and interpretation using mineral assemblages in Metamorphic Rocks: Journal of Petrology, v. 25, p. 929-954.

Thompson, J. B., 1957, The graphical analysis of mineral assemblages in pelitic schists: American Mineralogist, v. 42, p. 842-858.

Thompson, J. B., 1982, Composition space: an algebraic and geometric approach. In. Ferry, J. M., ed., Characterization of metamorphism through mineral equilibria: Mineralogical Society of America Reviews in Mineralogy, v. 10, p. 1-31.

Thompson, P. H., 1989, Moderate overthickening of thinned sialic crust and the origin of granitic magmatism and regional metamorphism in low-P-high-T terrains.

Tracy, R. J., 1982, Compositional zoning and inclusions in metamorphic minerals, In, Ferry, J. M., ed., Characterization of metamorphism through mineral equilibria: Mineralogical Society of America Reviews in Mineralogy, v. 10, p. 355-397.

Tracy, R. J., Robinson, P., and Thompson, A. B., 1976, Garnet composition and zoning in the determination of temperature and pressure of metamorphism, central Massachusetts. American Mineralogist, v. 61, p. 762-775.

Trumpy, R., 1983, Alpine paleogeography a reappraisal, Hsu, K. J. ed., Mountain Building Processes, Academic Press, New York, N. Y., p. 221-228.

Trzcienski, W. E., 1977, Garnet zoning - product of a continuous reaction: Canadian Mineralogist, v. 15, p. 250-256.

Turcotte, D. L., and Schubert, G., 1982. Geodynamics: Applications of Continuum Physics to Geologic Problems. Wiley, New York, N. Y., 450 pp.

Walker, R. J., Hanson, G. N., Papike, J. J., and O'Neil, 1986, Nd, O and Sr isotopic constraints on the origin of Precambrian rocks, southern Black Hills, South Dakota. Geochemica Cosmochemica Acta, v. 50, p 2833-2846.

Walther, J. V., and Orville, P. M., 1982, Volatile production and transport in regional metamorphism: Contributions to Mineralogy and Petrology, v. 79, p. 252-257.

Wickham, S. M., and Oxburgh, E. R., 1985, Continental rifts as a setting for regional metamorphism: Nature, v. 318, p. 330-333.

Windley, B. F., 1977, The Evolving Continents, Wiley, New York, N. Y., 385 pp.

APPENDICES

APPENDIX A1
THE FINITE DIFFERENCE SOLUTION

The time-dependent, heat-conduction equation

$$\frac{\partial T}{\partial t} = \kappa \left(\frac{\partial^2 T}{\partial z^2} + \frac{\partial^2 T}{\partial x^2}\right) + \frac{A_T}{K} - v\frac{\partial T}{\partial z} \qquad (A)$$

was solved numerically with the finite difference approximation

$$T^1_{(1,1)} = \frac{\kappa \Delta t}{\Delta h^2}\left(T^0_{(1,0)} + T^0_{(0,1)} + T^0_{(-1,0)} + T^0_{(0,-1)} - 4T^0_{(1,1)}\right) + \frac{\Delta t A_T}{K} + T^0_{(1,1)}. \qquad (B)$$

The superscripts refer to the time steps and the subscripts refer to the spacial coordinates. The source code of the FORTRAN programs used to solve equation (B) is presented in Appendix A2. The convection term in equation (A) accounts for the vertical motion of the crust towards the erosional surface. The motion of the crust was modeled simply by transforming the coordinates after the appropriate time interval. The choice of grid spacing Δx determines the magnitude of the time increment by the stability relationship

$$\Delta t = (0.15\Delta x^2)/\kappa. \qquad (C)$$

The accuracy of the heat flow program in Appendix A2 is evaluated by comparing numerical results at simple boundary conditions with analytical solutions to the time-dependent heat equation

$$\frac{1}{\kappa}\frac{\partial T}{\partial t} = \frac{\partial^2 T}{\partial x^2} + \frac{\partial^2 T}{\partial z^2}. \qquad (D)$$

The solution of equation (D) for a body (right cylinder) emplaced instantaneously into an infinite medium that is everywhere the same temperature T_o is

$$= \frac{1}{4} T_o \left\{ \operatorname{erf}\left(\frac{x-r}{\sqrt{\kappa t}}\right) + \operatorname{erf}\left(\frac{x+r}{\sqrt{\kappa t}}\right) \right\} \left\{ \operatorname{erf}\left(\frac{y-h}{\sqrt{\kappa t}}\right) + \operatorname{erf}\left(\frac{y+h}{\sqrt{\kappa t}}\right) \right\} \qquad (E)$$

(Carslaw and Jager, 1959). The variables x and y in equation (E) refer to the orthogonal dimensions of the body; r and h refer to the distance from the center of the body parallel to the x and y axes, respectively.

Figure A1.1 shows temperature-time curves estimated with equation

(E) and with the two-dimensional finite difference program in Appendix A2. Both the body and its surroundings have a thermal diffusivity of 9.0 x 10^{-7} m^2/s. The temperature-time curves (Figure A1.1) are for a point 1 km above an instantaneously emplaced body with a radius of 5 km and a height of 5 km. The body has an intial temperature of 850 °C and the surroundings have an initial temperature of 0° C. The numerical solution converges with the analytical solution as the grid spacing decreases; therefore, the finite difference solution is consistent with the solution of the partial differential equation (1) (e.g. Spear and Peacock, 1989).

The numerical solutions are least accurate during the first steps, however, the temperature-time curves for the analytical and numerical solutions converge as time increases. The large amount of error in the initial steps is due to the large initial flux at the contact between the body at and the surroundings. Figure A1.1 indicates that accurate approximations are attainable at a grid spacings of 250 m or less. Figure A1.2 is a temperature-time plot for the same body in Figure A1.1, intruded into a steady-state geotherm (A_r = 3.3 $\mu W/m^3$ and Q_r = 33 mW/m^2). Because the flux at the contact between the body and the surroundings is smaller in the model shown in Figure A2.2, there is less divergence in the initial time steps. There is almost complete convergence of the numerical solutions at grid spacing below 250 m. Even at a gird spacing of 1 km the numerical solution diverges only a few (~18 °C) degrees from the solution with a grid spacing of 200 m.

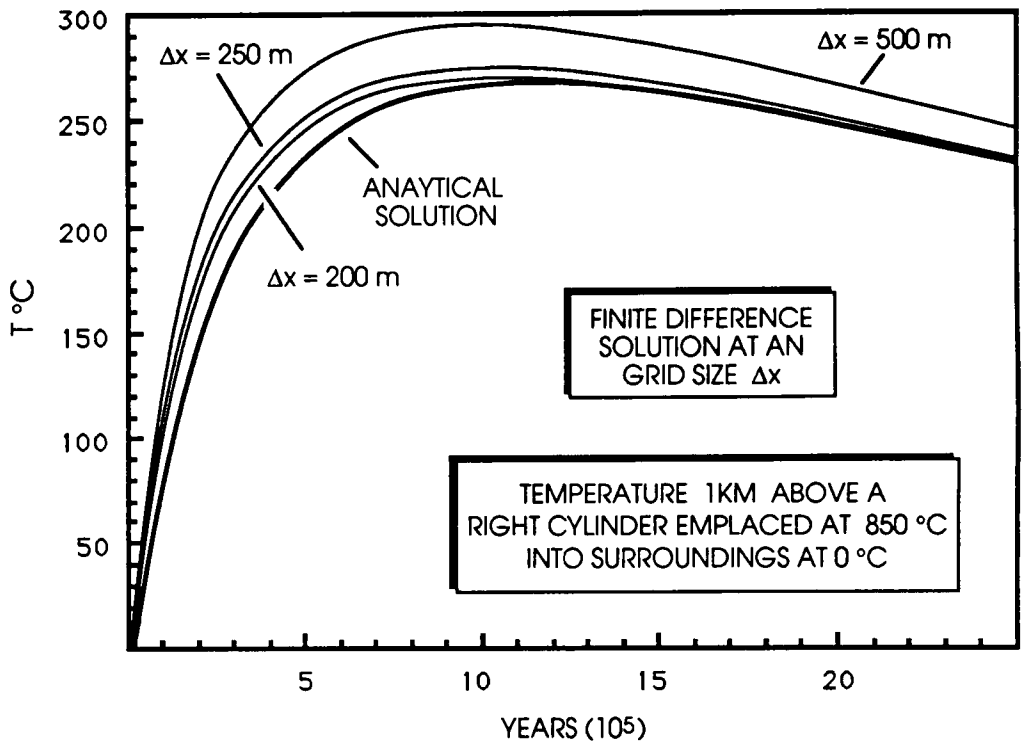


Figure A1.1. A graphical comparison of the analytical solution of the two-dimensional time-dependent heat equation with the numerical approximation calculated with the program in Appendix A3.

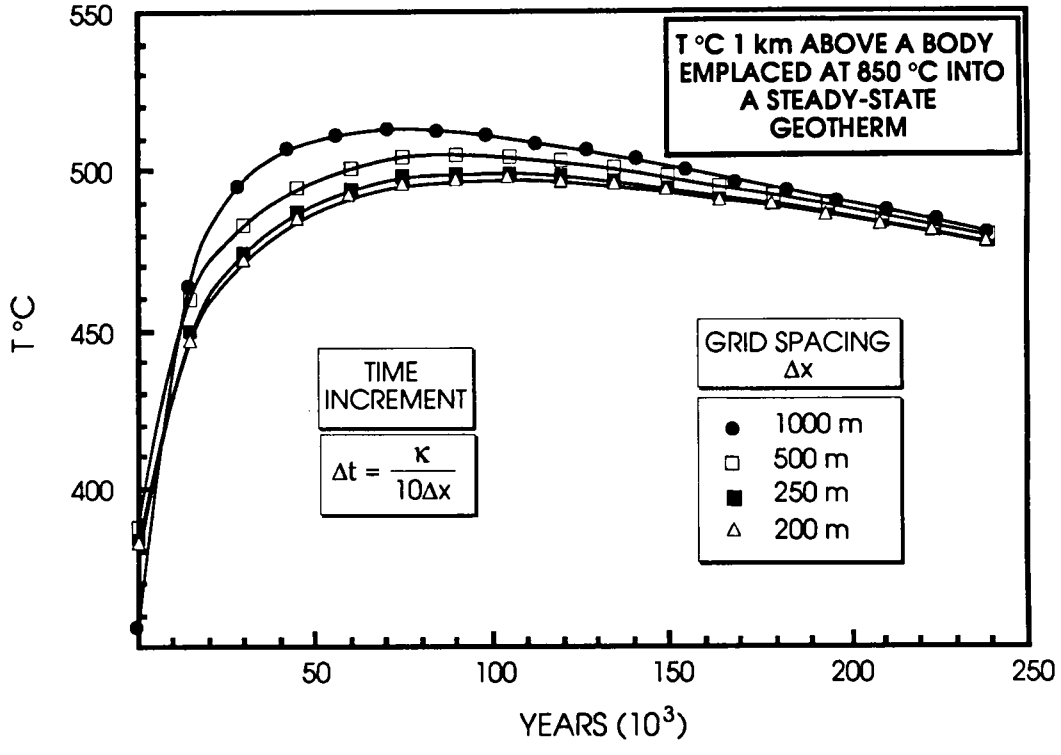


Figure A1.2. Test for convergence using smaller grid sizes with the finite difference program presented in Appendix A3.

APPENDIX A2
FORTRAN SOURCE CODE FOR A FINITE DIFFERENCE PROGRAM

FORTRAN source code for a finite difference program that approximates the solution of the two-dimensional time-dependent heat conduction equation with heat sources and heat sinks. The program estimates the thermal profile adjacent to a two-dimensional pluton that is intruded instantaneously. The intrusion may occur at any time along the uplift path of an instantaneously heterogeneously, or homogeneously thickened crust.

```
C*********************************************************************
C              PROGRAM 2D
C*********************************************************************
C THE FOLLOW PROGRAM APPROXIMATES THE THERMAL CONSEQUENCES OF
C INSTANTANEOUS HOMOGENEOUS AND HETEROGENEOUS CRUSTAL
THICKENING
C FOLLOWED BY UPLIFT AND EROSION. INTRUSION OF MAGMA IS ALLOWED
C AT ANY TIME DURING DECOMPRESSION. THE TIME DEPENDENT HEAT EQUATION,
C WITH TERMS FOR CONVECTIVE COOLING (E.G. UPLIFT) AND RADIOGENIC HEAT
C PRODUCTION, IS SOLVED WITH AN EXPLICIT FINITE DIFFERENCE METHOD.
C THE PROGRAM RUNS IN ONE DIMENSION PRIOR TO THE INTRUSION, 500000 YR
C PRIOR TO THE INTRUSION THE PROGRAM ADD A SECOND DIMENSION
C*********************************************************************
C              THE INPUT PARAMETERS
C*********************************************************************
C                                    2D 00150
C XKAPPA = THERMAL DIFFUSIVITY (m2/s)
C L = WIDTH OF THE GRID (m)
C LD = DEPTH OF GRID (m)
C IT = DEPTH TO BASE OF THE THRUST (m)
C WCON = RADIUS OF THE PLUTON (m)
C HCON = DEPTH TO TOP OF PLUTON (m)
C DCON = DEPTH TO BASE OF PLUTON (m)
C RATE: IF NOT 1 PRINT ALL OUTPUT PRIOR TO INTRUSION
C BLCMV = EXHUMATION RATE (mm/yr)
C H = THE GIRD INCREMENT SIZE (m) USED IN THE FINITE DIFFERENCE
C CALCULATION
C Q = THE HEAT FLUX BEFORE CRUSTAL THICKENING (W/m2)
C Q2 = NEW HEAT FLUX (IF DESIRED) AFTER THICKENING (W/m2)
```

```
C  AO = RADIOGENIC HEAT PRODUCTION IN THE UPPER CRUST (microW/m3)
C  A2 = RADIOGENIC HEAT PRODUCTION OF THE INTRUSION (microW/m3)
C  YO = TEMPERATURE OF MAGMA
C  TOTAL = TIME TO RUM MODEL (YR)
C  JPOINT, JP2, JP3: DEPTH COORDINATE TO TRACK
C  IPOINT, IP2, IP3: LATERAL COORDINATES TO TRACK (e.g.{JP2,IP2})
C  IEND = NUMBER OF MAGAMA PULSES
C  DELAY = NUMBER OF YEARS BEFORE INTRUSION
C  KSUPR:  IF = 1 PRINT ALL DATA INCLUDING THE GEOTHERMAL GRADIENT
C  HALT = NUMBER OF YEARS TO DELAY UPLIFT AFTER CRUSTAL THICKENING
C  XMELTC = WT% PARTIAL MELTING IN LOWER CRUST WHEN T > 650 DEG CEL
C  TMELTC = TIME (YR) THAT MELTING OCCURS
C  XMELTP = WT% MELT IN PLUTON
C  TMELTP = TIME (YR) SPAN HEAT OF FUSION IS RELEASED FROM PLUTON
C  HOMO: IF 1 HOMOGENEOUS THICKENING;IF NOT 1 HETEROGENEOUS THICK.
C  HTC: FACTOR OF HOMOGENEOUS THICKENING DESIRED
C  NNN: 1 = PTt PATH ONLY/ GREATER VALUES RESULT PRINTING OF SMALL TIME
C    STEPS
C
C    LIST OF HEAT SOURCES AND HEAT SINKS
C
C A1 = RADIOGENIC HEAT PRODUCTION OF THE UPPER CRUST
C A2 = RADIOGENIC HEAT PRODUCTION OF THE GRANITE
C A3 = HEAT OF FUSION RELEASED BY PLUTON
C A4 = HEAT ABSORBED BY ENDOTHERMIC DEHYDRATION REACTIONS
C A5 = HEAT ABSORBED BY PARTIAL  MELTING
C*********************************************************************
C*********************************************************************
      IMPLICIT  REAL*8(A-H,O-Z)
      DIMENSION  T(500,500),T2(500,500)
      CHARACTER*12 DUMP
      CHARACTER*1 ANS
      OPEN(1,FILE='DUMP',STATUS='NEW')
      OPEN(2,FILE='PLUT',STATUS='NEW')
      CALL  RDAT(XKAPPA,L,LD,IT,WCON,HCON,DCON,RATE,BLCMV,H,Q,
     *AO,A2,YO,TOTAL,JPOINT,JP2,JP3,IPOINT,IP2,IP3,IEND,IP,JP,Q2,
     *DELAY,KSUPR,HALT,XMELTC,TMELTC,XMELTP,TMELTP,HOMO,HTC,NNN)
  19  FORMAT(10(1X,F5.0))
 138  FORMAT(F16.0)
1020  FORMAT(7(F10.0))
```

```
 1021   FORMAT(3(I6))
 1022   FORMAT(10(1X,F6.2))
 1211   FORMAT(F16.1)
 9990   FORMAT(1X,F16.0)
C
C ESTIMATE THE TIME INCREMENT BASE ON THE STABILITY RELATIONSHIP ETC.
C
        TAU=(0.15*(H**2))/XKAPPA
        BTAU=TAU/(365.25*24*60*60)
        TOTAL=TOTAL*365.25*3600*24
        XM=(XKAPPA*TAU)/(H**2)
        COND=(XKAPPA*2500000)
        BTIME=TIME/(365.25*24*60*60)
        BLCMV=BLCMV/(1000*365.25*24*3600)
C
C       HEAT SOURCES AND SINKS
C
        A1=(AO*TAU*XKAPPA)/COND
        A2I=(A2*TAU*XKAPPA)/COND
        A3=(540000000*XMELTP)/(TMELTP*365.25*24*3600)
        A3=(A3*TAU*XKAPPA)/COND
        A4=-(0.000080*TAU*XKAPPA)/COND
        A5=-(540000000*XMELTC)/(TMELTC*365.25*24*3600)
        A5=(A5*TAU*XKAPPA)/COND
C
C NORMALIZED SPACIAL DIMENSIONS BY THE GRID INCREMENT H
C         AND INITIALIZE VARIABLES
C
        IDEP=15000/H
        IP4=IP3+1000
        IP5=IP4+1000
        IP6=IP5+1000
        IP7=IP6+1000
        IP8=IP7+1000
        IPOINT=IPOINT/H
        ZPOINT=IPOINT*H
        IPOINTI=IPOINT
        IP2=IP2/H
        IP3=IP3/H
```

```
      IP4=IP4/H
      IP5=IP5/H
      IP6=IP6/H
      IP7=IP7/H
      IP8=IP8/H
      P3I=IP3
      IP2I=IP2
      IPOINT=IPOINTI
      JPOINT=JPOINT/H
      JP1=JPOINT
      JP2=JP2/H
      JP3=JP3/H
      NWCON=WCON/H
      NHCON=HCON/H
      NDCON=DCON/H
      NINC=L/H
      NINCI=NINC
      KINC=LD/H
      IT=IT/H
      ITI=IT
      JSTEP=(TOTAL/TAU)
      MSTEP=JSTEP/NNN
      MSTEPI=MSTEP
      NSTEP=JSTEP/20
      NSTEPI=NSTEP
      ISTUMP=0
      IBAS=0
      ADUM=0
      ADUM2=0
      NULL=0
      TIME=0
      SKIP=0
      AHOC=0
      ADUM3=0
      HFUS=0
      LPAS1=0
      LPAS2=0
      LPAS3=0
C
C IF INTRUSION OF GRANITE DESIRED AT A DELAYED TIME RUN IN 1D
```

```
C            UNTIL INTRUSION OCCURS
C
      IF(DELAY.EQ.0)GOTO 1311
      NINC=1
      IPOINT=1
      IP2=1
      IP3=1
 1311 CONTINUE
C
C   SYNCHRONIZE BLOCK MOVEMENT WITH SPACE & TIME MESH SIZE
C
      KLOOP=(H/BLCMV)/TAU
      KLOOPI=KLOOP
C
C ENTER INITIAL TEMPERATURE APPROPRIATE FOR THE INTERNAL HEAT
C PRODUCTION AO AND MANTEL FLUX Q
C
      IF(HOMO.NE.1)GOTO 4323
C
C INSERT GEOTHERM FOR HOMOGENEOUSLY THICKENED CRUST
C
      IDEP=(HTC*15000)/H
      D=15000*HTC
      GAMMA=(((Q2*((KINC+1)*H))/COND)+((AO*((D**2)))/(2*COND)))/
      (((Q2*((KINC/HTC)*H))/COND)+((AO*(D**2))/(2*COND)))
      DO 1401 I=1,NINC+1
      DO 1501 J=1,IDEP
      T(I,J)=(((AO*(J-1)*H)/COND)*(D-(((J-1)*H)/2))+
     +(Q*((J-1)*H))/(COND))/GAMMA
1501  CONTINUE
1401  CONTINUE
      DO 6100 I=1,NINC+1
      DO 6101 J=(IDEP+1),KINC+1
      T(I,J)=(((Q*(J*H))/COND)+((AO*D**2)/(2*COND)))/GAMMA
6101  CONTINUE
6100  CONTINUE
      CBASE=(((Q2*((KINC+1)*H))/COND)+((AO*(D**2))/(2*COND)))
      TBASE=(((Q*((KINC+1)*H))/COND)+((AO*(D**2))/(2*COND)))/GAMMA
      TBASEI=TBASE
```

```
      IDEP=(D*HTC)/H
4323  CONTINUE
C
C  INSERT GEOTHERM FOR CRUST THICKENED BY A SINGLE THRUST
C
      IF(HOMO.EQ.1)GOTO 3234
      IF(IT.EQ.0)IBAS=1
      IF(IT.EQ.0.0)IT=KINC
      IDEP=15000/H
      DO 140 I=1,NINC+1
      DO 150 J=1,IDEP
      T(I,J)=((AO*(J-1)*H)/COND)*(15000-(((J-1)*H)/2))+
     +(Q*((J-1)*H))/COND
150   CONTINUE
140   CONTINUE
      DO 6000 I=1,NINC+1
      DO 6001 J=IDEP,IT+IBAS
      T(I,J)=((Q*(J*H))/COND)+((AO*15000**2)/(2*COND))
6001  CONTINUE
6000  CONTINUE
      NZIP=KINC-IT
      IF(NZIP.LE.0)GOTO 1078
      IF(NZIP.LT.IDEP)IDEP=KINC-IT
      NZIT=IT+IDEP
      DO 142 I=1,NINC+1
      DO 152 J=IT,NZIT
      T(I,J)=((AO*(J-IT)*H)/COND)*(15000-(((J-IT)*H)/2))+
     +(Q*((J-IT)*H))/COND
152   CONTINUE
142   CONTINUE
      IF(NZIP.LT.IDEP)GOTO 1078
      DO 6002 I=1,NINC+1
      DO 6003 J=NZIT,KINC+1
      T(I,J)=((Q*((J-IT)*H))/COND)+((AO*(15000**2))/(2*COND))
6003  CONTINUE
6002  CONTINUE
1078  CONTINUE
      IT=ITI
      TBASE=((Q*((KINC-IT+1)*H))/COND)+((AO*(15000**2))/(2*COND))
```

```
      CBASE=((Q2*((KINC+1)*H))/COND)+(AO*(15000**2))/(2*COND)
      TBASEI=TBASE
3234  CONTINUE
C
C INSERT TEMPERATURE OF MAGMA BODY
C
      IF(DELAY.GT.0)GOTO 111
      NOPE=1
      DO 10 I=1,NWCON
      DO 110 J=NHCON,NDCON
      T(I+1,J)=YO
110   CONTINUE
10    CONTINUE
111   CONTINUE
C
C   PRINT INITIAL THERMAL DISTRIBUTION
C
      XPOINT=JPOINT*H
      XP2=JP2*H
      XP3=JP3*H
      JPRN=1
      KPRN=1
      IPRN=KPRN
      KPRN=NINCI/IP
      JPRN=KINC/JP
      WRITE(1,138)ZPOINT
      DO 500 J=1,10
      WRITE(6,19)(T((I*KPRN),(1+(J*JPRN)-JPRN)),I=1,10)
      WRITE(1,19)(T((I*KPRN),(1+(J*JPRN)-JPRN)),I=1,10)
500   CONTINUE
      WRITE(1,19)(T((I*KPRN),(1+KINC)),I=1,10)
      WRITE(6,1020)IPOINT,IP2,IP3
      WRITE(6,1020)XPOINT,XP2,XP3,T(IPOINT,JPOINT),T(IP2,JP2),
     *T(IP3,JP3),BTIME
      WRITE(1,1020)XPOINT,XP2,XP3,T(IPOINT,JPOINT),T(IP2,JP2),
     *T(IP3,JP3),BTIME
      WRITE(2,1022)T(IPOINT,JPOINT),T(IP2,JP1),T(IP3,JP1),
     *T(IP4,JP1),T(IP5,JP1),T(IP6,JP1),T(IP7,JP1),T(IP8,JP1)
     *,(JP1*H)/1000
      WRITE(2,1022)T(IPOINT,JP2),T(IP2,JP2),T(IP3,JP2),
```

```
     *T(IP4,JP2),T(IP5,JP2),T(IP6,JP2),T(IP7,JP2),T(IP8,JP2)
     *,(JP2*H)/1000                                2D 02640
      WRITE(2,1022)T(IPOINT,JP3),T(IP2,JP3),T(IP3,JP3),
      *,(JP2*H)/1000
C
C FINITE DIFFERENCE LOOP
C
      JDEP=IT+IDEP
      DO 30 M=1,JSTEP
      TIME=TAU*M
      BTIME=TIME/(365.25*24*3600)
      IF(BTIME.LT.DELAY)A2=0
      IF(BTIME.GE.DELAY)A2=A2I
      IF(BTIME.GE.DELAY)AHOC=A3
      IF(BTIME.GE.(DELAY+500000))AHOC=0
      IF(BTIME.GE.DELAY)ADUM3=A4
      IF(BTIME.GE.(DELAY+500000))ADUM3=0
C
C   MOVE BLOCK AFTER APPROPRIATE TIME
C
      IF(BTIME.LT.HALT)GOTO 6521
      IF(M.NE.KLOOP)GOTO 56
      IF(IDEP.LE.1)GOTO 1140
      IDEP=IDEP-1
1140  CONTINUE
      IF(IT.LE.1)GOTO 1141
      IT=IT-1
1141  CONTINUE
      IF(JDEP.LE.1)GOTO 1142
      JDEP=JDEP-1 0
1142  CONTINUE
      DO 702 I=1,NINC
      DO 701 J=1,KINC
      T(I,J)=T(I,J+1)
701   CONTINUE
702   CONTINUE
      IF(HOMO.NE.1)GOTO 3301
      D=D-1
      CBASE=(((Q2*((KINC+1)*H))/COND)+((AO*(D**2))/(2*COND)))
```

```
      IF(CBASE.GT.1350)CBASE=1350
      IF(TBASE.LT.CBASE.AND.NULL.EQ.1)TBASE=CBASE
3301  CONTINUE
      DO 703 I=1,NINC+LPAS1
      T(I,1)=0
      T(I,KINC+1)=TBASE
703   CONTINUE0
479   KLOOP=KLOOP+KLOOPI
      JPOINT=JPOINT-1
      JP1=JP1-1
      JP2=JP2-1
      JP3=JP3-1
      XPOINT=JPOINT*H
      XP2=JP2*H
      XP3=JP3*H
      WRITE(6,1020)XPOINT,XP2,XP3,T(IPOINT,JPOINT),T(IP2,JP2),
     *T(IP3,JP3),(BTIME/1000000)
      WRITE(1,1020)XPOINT,XP2,XP3,T(IPOINT,JPOINT),T(IP2,JP2),
     *T(IP3,JP3),(BTIME/1000000)
      WRITE(2,1022)T(IPOINT,JPOINT),T(IP2,JP2),T(IP3,JP3),
     *T(IP4,JP3),T(IP5,JP3),T(IP6,JP3),T(IP7,JP3),T(IP8,JP3),
     *(BTIME/1000000),(JP3*H)/1000
 56   CONTINUE
 53   CONTINUE
      DO 7031 I=1,NINC+LPAS1
      T(I,1)=0
      T(I,KINC+1)=TBASE
7031  CONTINUE
C
      IF(BTIME.GE.HALT)GOTO 56110
6521  CONTINUE
      IF(M.NE.KLOOP)GOTO 5699
      KLOOP=KLOOPI+KLOOP+1
5699  CONTINUE
      IF(NSTEP.NE.M)GOTO 5611
      NSTEP=NSTEP+NSTEPI
      WRITE(6,1020)XPOINT,XP2,XP3,T(IPOINT,JPOINT),T(IP2,JP2),
     *T(IP3,JP3),(BTIME/1000000)
      WRITE(1,1020)XPOINT,XP2,XP3,T(IPOINT,JPOINT),T(IP2,JP2),
```

```
     *T(IP3,JP3),(BTIME/1000000)
5611  CONTINUE
      DO 709 I=1,NINC+1
      T(I,1)=0
      T(I,KINC+1)=TBASE
709   CONTINUE
C
C
C FINITE DIFFERENCE CALCULATION FOR DOUBLED CRUST
C
      IF(HOMO.EQ.1)GOTO 1999
      DO 48 I=1,(NINC-2)
      DO 58 J=1,IT
      IF(J.LE.IDEP)ADUM=A1
      IF(J.GE.IDEP)ADUM=0
      Z=(T(I+1,J+1))
      T2(I+1,J+1)=XM*(T(I+1,J)+T(I+1,J+2)+T(I+2,J+1)+T(I,J+1)-(4*Z))+Z
     *+ADUM
58    CONTINUE
48    CONTINUE
      DO 481 I=1,(NINC-LPAS2)
      DO 581 J=IT,KINC-1
      IF(J.LE.JDEP)ADUM=A1
      IF(J.GE.JDEP)ADUM=0
      Z=(T(I+1,J+1))
      T2(I+1,J+1)=XM*(T(I+1,J)+T(I+1,J+2)+T(I+2,J+1)+T(I,J+1)-(4*Z))+Z
     *+ADUM
581   CONTINUE
481   CONTINUE
1155  CONTINUE
      IF(HOMO.NE.1)GOTO 321
C
C FINITE DIFF. CALCULATION FOR A HOMOGENEOUSLY SHORTENED CRUST
C
1999  CONTINUE
      IF(DELAY.EQ.0)GOTO 9129
      IF(BTIME.GE.(DELAY-50000))GOTO 9129
      DO 3091 J=1,KINC
      IF(J.GE.IDEP)ADUM=0
      IF(J.LE.IDEP)ADUM=A1
```

```
      IF(T(1,J).GE.650)HFUS=A5
      T2(1,J)=XM*(T(1,J-1)-(2*T(1,J))+T(1,J+1))+T(1,J)+ADUM
3091  CONTINUE
      IF(BTIME.LT.(DELAY-50000))GOTO 321
9129  CONTINUE
      DO 4888 I=1,(NINC-2)
      DO 5888 J=1,KINC
      IF(J.GE.IDEP)ADUM=0
      IF(J.LE.IDEP)ADUM=A1
      IF(J.GT.NHCON.AND.I.LT.NWCON)ADUM2=A2+AHOC0
      IF(J.GT.NDCON.OR.J.LT.NHCON)ADUM2=0
      IF(ADUM2.GT.0)ADUM=0
      IF(J.GT.(NHCON-5).AND.I.LT.(NWCON+5))AVOL=ADUM3
      IF(J.GT.(NDCON+4))AVOL=0
      IF(ADUM2.GT.0)AVOL=0
      Z=(T(I+1,J+1))
      T2(I+1,J+1)=XM*(T(I+1,J)+T(I+1,J+2)+T(I+2,J+1)+T(I,J+1)-(Z*4))+Z
     *+ADUM
5888  CONTINUE
4888  CONTINUE
C
C  RESTORE MODEL TO 2 DIMENSIONS PRIOR TO GRANITE INTRUSION
C
321   CONTINUE
      IF(DELAY.EQ.0)GOTO 912
      IF(BTIME.LT.(DELAY-50000))GOTO 912
      IF(SKIP.EQ.1)GOTO 912
      DO 532 I=1,NINCI+1
      DO 654 J=1,KINC+1
      T2(I+1,J)=T2(I,J)
654   CONTINUE
532   CONTINUE
      LPAS2=2
      LPAS1=1
      SKIP=1
      IPOINT=IPOINTI
      IP2=IP2I
      IP3=IP3I
      NINC=NINCI
```

```
912     CONTINUE
C
C       ADD NEW PULSE OF MAGMA
C
        IF(DELAY.GT.BTIME.OR.NOPE.EQ.1)GOTO 5321
        MP=NHCON+2
        TAR=T2(2,MP)
        IF(ISTUMP.GE.IEND)GOTO 5321
        IF(TAR.GT.650)GOTO 5321
        ISTUMP=1+ISTUMP
        DO 5444,I=1,NWCON
        DO 5445,J=NHCON,NDCON
        T2(I+1,J)=YO
5445    CONTINUE
5444    CONTINUE
        WRITE(1,5446)
5446    FORMAT( ' NEW PULSE ' )
5321    CONTINUE
C
C HOLD TEMPERATURE AT BASE CONSTANT OR INCREASE FLUX
C
        IF(TBASE.GE.CBASE.OR.TBASE.GT.1350)NULL=1
        IF(TBASE.GE.CBASE.OR.TBASE.GT.1350)GOTO 3330
        TBASE=(((2*H*Q2)/COND)+(4*T2(1,KINC)-T2(1,KINC-1)))/3
3330    CONTINUE
        DO 60 I=1,NINC+1
        T2(I,KINC+1)=TBASE
        T2(I,1)=0
60      CONTINUE
C
C KEEP TEMPERATURE IN COLUME 1 = TEMPERATURE IN COLUME LEFT OF
C THE CONDUIT/ IF RIGHT BOUNDARY IS AFFECTED, APPROXIMATE THE
C LAST RIGHT COLUME VALUE BY THE CHANGE IN THE TWO ADJACENT COLUMES
C
        IF(BTIME.LT.(DELAY-50000))GOTO 9121
        DO 70 J=1,KINC+1
        T2(1,J)=T2(3,J)
70      CONTINUE
        DO 398 J=1,KINC+1
        DELTA=T2((NINC-1),J)-T2((NINC-2),J)
```

```
      IF(DELTA.LT.0.00000001.OR.DELTA.GT.-0.00000001)DELTA=0
      T2(NINC,J)=T((NINC-1),J)+DELTA
 398  CONTINUE
 9121 CONTINUE
C
C     WRITE T2(I,J) BACK INTO T(I,J)
C
      DO 80 I=1,NINC
      DO 90 J=1,KINC
      T(I,J)=T2(I,J)
 90   CONTINUE
 80   CONTINUE
C
C     END FINITE DIFFERENCE LOOP/PRINT RESULTS
C
      IF(M.NE.MSTEP)GOTO 31
      MSTEP=MSTEP+MSTEPI
      IF(RATE.NE.0.AND.BTIME.LT.(DELAY-50000))GOTO 31
      IF(KSUPR.NE.1)GOTO 1166
      DO 100 J=1,11
      WRITE(6,19)(T((I*KPRN),(1+(J*JPRN)-JPRN)),I=1,10)
      WRITE(1,19)(T((I*KPRN),(1+(J*JPRN)-JPRN)),I=1,10)
100   CONTINUE
      WRITE(6,138)BTIME
      WRITE(1,138)BTIME
1166  CONTINUE
      WRITE(6,1020)XPOINT,XP2,XP3,T(IPOINT,JPOINT),T(IP2,JP2),
     *T(IP3,JP3),BTIME
      WRITE(1,1020)XPOINT,XP2,XP3,T(IPOINT,JPOINT),T(IP2,JP2),
     *T(IP3,JP3),BTIME
C
      WRITE(2,1022)T(IPOINT,JPOINT),T(IP2,JP1),T(IP3,JP1),
     *T(IP4,JP1),T(IP5,JP1),T(IP6,JP1),T(IP7,JP1),
     *T(IP8,JP1),(BTIME/1000000),(JP1*H)/1000
      WRITE(2,1022)T(IPOINT,JP2),T(IP2,JP2),T(IP3,JP2),
     *T(IP4,JP2),T(IP5,JP2),T(IP6,JP2),T(IP7,JP2),T(IP8,JP2)
     *,(BTIME/1000000),(JP2*H)/1000
      WRITE(2,1022)T(IPOINT,JP3),T(IP2,JP3),T(IP3,JP3),
     *T(IP4,JP3),T(IP5,JP3),T(IP6,JP3),T(IP7,JP3),T(IP8,JP3)
```

```
     *,(BTIME/1000000),(JP3*H)/1000
      WRITE(2,9010)
9010  FORMAT('          ')
923   CONTINUE
 31   CONTINUE
 30   CONTINUE
      CLOSE(1,STATUS='KEEP')
      CLOSE(2,STATUS='KEEP')
      STOP
      END
C
C  GET DATA FROM FILE
C
      SUBROUTINE RDAT(XKAPPA,L,LD,IT,WCON,HCON,DCON,RATE,BLCMV,
     +H,Q,AO,A2,YO,TOTAL,JPOINT,JP2,JP3,IPOINT,IP2,IP3,IEND,IP,JP,Q2,
     +DELAY,KSUPR,HALT,XMELTC,TMELTC,XMELTP,TMELTP,HOMO,HTC,NNN)
       IMPLICIT REAL*8(A-H,O-Z)
      CHARACTER*1 ANS
      CHARACTER*12 DAT2D
      OPEN(5,FILE='DATI',STATUS='OLD')
40    FORMAT(1X,F16.0)
15    FORMAT(1X,A1)
20    FORMAT(1X,F12.10)
125   FORMAT(3(1X,I5))
25    FORMAT(1X,I5)
26    FORMAT(1X,I6)
30    FORMAT(1X,F16.4)
35    FORMAT(1X,F16.15)
      READ(5,20)XKAPPA
      READ(5,25)L
      READ(5,26)LD
      READ(5,25)IT
      READ(5,30)WCON
      READ(5,30)HCON
      READ(5,30)DCON
      READ(5,35)RATE
      READ(5,35)BLCMV
      READ(5,30)H
      READ(5,35)Q
```

```
      READ(5,36)AO
      READ(5,36)A2
36    FORMAT(1X,F10.9)
      READ(5,30)YO
      READ(5,40)TOTAL
      READ(5,25)JPOINT
      READ(5,25)JP2
      READ(5,25)JP3
      READ(5,25)IPOINT
      READ(5,25)IP2
      READ(5,25)IP3
      READ(5,25)IEND
      READ(5,25)IP
      READ(5,25)JP
      READ(5,35)Q2
      READ(5,40)DELAY
      READ(5,25)KSUPR
      READ(5,40)HALT
      READ(5,36)XMELTC
      READ(5,40)TMELTC
      READ(5,36)XMELTP
      READ(5,40)TMELTP
      READ(5,20)HOMO
      READ(5,20)HTC
      READ(5,26)NNN
      CLOSE(5,STATUS='KEEP')
      RETURN
      END
```

THE FOLLOWING IS AN EXAMPLE OF THE INPUT FILE NECESSARY TO RUN THE PROGRAM 2D

0.0000009	THERMAL DIFFUSIVITY (m2/s)
50000	LATERAL EXTENT (m)
70000	DEPTH (m)
0	BASE OF THRUST (m)
7000.	RADIUS OF PLUTON (m)
12000.	DEPTH TO TOP OF PUTON (m)
17000.	DEPTH TO BOTTOM OF PLUTON (m)
0.1	IF 0 PRINTS ALL DATA PRIOR TO INTRU
0.014	EXUMATION RATE (mm/yr)

500.	GRID INCREMENT (m)
.033	MANTLE FLUX (W/m2)
0.0000033	RADIOGENIC HEAT PROD (micW/m3)
0.0000085	HEAT PRODUC GRANITE (micW/m3)
850.00	TEMPERATURE OF PLUTON (DEG C OR K)
43000000.	RUN TIME (YRS)
15000	DEPTH TO TRACK (m)
16000	" " " "
17000	" " " "
15500	LATERAL POSITION TO TRACK (m)
16500	" " " " "
17500	" " " " "
1	NUMBER OF MAGMA PULSES
10	NUMBER OF COLUMNS PRINTED
10	NUMBER OF ROWS PRINTED
0.033	NEW FLUX AT BASE OF CRUST
36000000.	DELAY BEFORE INTRUSION (YRS)
2.	1 = PRINT TEMP GRID/ NOT 1 = PTt
00000000.	TIME TO HALT EXHUMATION (YRS)
0.5	FRACT. ROCK(m3) MELTS IF >650 DEG.
10.	TIME OVER WHICH CRUST MELTS
0.5	FRACTION OF PLUTON THAT IS MELT
500000.	TIME FOR PLUTON TO CRYSTALLIZE
1.	1 = HOMOGENEOUS THICKENING
2.	FACTOR OF THICKENING
2000	1 = PRINT ONLY PTt PATH

APPENDIX A3
ELECTRON MICROPROBE ANALYSES

This appendix lists mineral compositions as weight % oxides. Mineral analysis and estimated cation formulas are stored as ASCII files on a high density disk (Insert 1). Minerals were normalized on the basis of the appropriate number of oxgens. Ferric iron was calculated for stoichiometric phases if the weight % oxide totals were consistently low and the cation totals were consistently high; ilmentite and hematite were the only phases that fit this criterion. Biotite and muscovite have vacancies, therefore iron was assumed to be all ferrous.

Mineral analyses were collected on a four spectrometer Cameca SX50 electron microprobe at the University of Tennessee using synthetic and natural standards and operating at an accelerating volatage of 15 kV. Analyses were collected with a wave length dispersive technique, utilizing ZAF corrections. A beam current of 0.015 μA and a beam diameter of ~10 μm were used analyze micas, felspars, and cordierite. Garnet, chlorite, and staurolite were analyzed with a beam current of 0.03 μA and a beam diameter of ~5 μA. Analytical precision on major elements (< 2 weight % oxide) is approximately ± 2%, and precision on minor components is approximately ± 8.0%.

Table A3.1. Garnet Compositions

Sample:	87-121AA										
#	1	2	3	4	5	6	7	8	9	10	11
SiO2	36.87	36.81	36.76	36.71	36.86	36.99	36.45	36.30	36.53	36.44	36.44
Al2O3	20.92	20.63	20.87	20.99	20.92	20.63	20.84	20.80	20.67	20.77	20.65
TiO2	0.00	0.05	0.02	0.00	0.35	0.01	0.01	0.02	0.02	0.13	0.18
MgO	2.14	1.86	1.95	2.07	2.34	2.20	1.70	1.78	1.77	2.29	2.24
CaO	1.68	1.14	0.98	1.60	1.46	1.71	1.08	1.06	1.05	1.66	1.60
MnO	4.69	4.89	4.99	4.83	5.34	5.48	5.33	5.06	5.15	4.58	4.79
FeO	33.95	35.21	35.39	34.47	33.78	32.89	35.54	35.27	35.16	33.87	34.49
Total	100.26	100.58	100.98	100.67	101.05	99.93	100.97	100.30	100.37	99.75	100.43

Sample:	86-22(CAM)								86-22(MAC)	
#	1	2	3	4	5	7	8	9	10	1A	2A
SiO2	36.68	36.28	36.33	36.40	36.46	36.36	36.41	36.28	36.28	36.50	36.46
Al2O3	20.81	20.69	20.80	20.85	20.89	20.86	20.89	20.67	20.63	21.72	21.77
TiO2	0.00	0.17	0.29	0.17	0.17	0.36	0.36	0.38	0.07	0.02	0.02
MgO	2.13	2.17	2.22	2.30	2.31	2.25	2.29	2.25	2.36	2.41	2.54
CaO	0.56	0.56	0.56	0.58	0.59	0.56	0.53	0.59	0.55	0.59	0.52
MnO	4.51	4.53	4.52	4.55	4.25	4.19	4.17	5.20	3.71	3.96	4.42
FeO	35.59	35.44	35.68	35.13	35.24	36.11	36.01	35.19	36.26	35.11	35.11
Total	100.55	99.86	100.40	99.98	99.92	100.74	100.71	100.60	99.86	100.31	100.84

Sample:	86-22(MAC)										
#	2A	4A	5A	7A	8A	3A	9A	10A	11A	12A	13A
SiO2	36.46	36.84	36.32	36.48	36.51	37.01	36.52	36.08	36.12	36.39	36.45
Al2O3	21.77	21.39	21.39	21.36	21.32	21.57	21.45	21.26	21.20	21.20	21.33
TiO2	0.02	0.03	0.00	0.01	0.01	0.03	0.05	0.04	0.00	0.00	0.00
MgO	2.54	2.41	2.00	2.30	2.05	2.43	2.32	2.36	2.31	2.31	2.34
CaO	0.52	0.50	0.45	0.47	0.39	0.63	0.68	0.70	0.68	0.67	0.65
MnO	4.42	4.93	4.41	4.19	4.28	4.95	5.30	5.71	6.22	5.76	5.37
FeO	35.11	34.43	36.46	36.27	35.91	34.53	34.81	33.94	34.22	34.54	34.89
Total	100.84	100.53	101.03	101.08	100.47	101.15	101.13	100.09	100.75	100.87	101.03

Table A3.1. Garnet Compositions (Continued)

Sample:	86-22										
#	14A	6A	15A	16A	17A	18A	19A	1C	2C	3C	4C
SiO2	36.18	36.04	36.61	36.38	36.77	36.68	36.13	36.65	36.41	36.36	35.80
Al2O3	21.18	21.41	21.47	21.71	21.57	21.57	21.47	21.71	21.49	21.52	21.28
TiO2	0.00	0.02	0.00	0.00	0.00	0.00	0.00	0.00	0.00	0.00	0.00
MgO	2.36	2.17	2.30	2.25	2.11	2.29	2.19	2.27	1.86	2.33	2.05
CaO	0.56	0.41	0.61	0.66	0.61	0.61	0.63	0.40	0.36	0.38	0.38
MnO	4.54	4.39	5.13	5.57	5.61	4.82	5.78	3.98	4.62	4.30	4.57
FeO	36.12	36.41	34.59	34.98	34.57	35.49	34.01	35.95	36.24	36.03	36.57
Total	100.94	100.85	100.71	101.55	101.24	101.46	100.21	100.96	100.98	100.92	100.65

Sample:	86-47A										
#	1	2	3	4	5	6	7	8	9	10	11
SiO2	36.34	36.20	36.34	36.05	36.05	36.43	36.39	36.50	36.20	36.04	36.36
Al2O3	21.37	21.40	21.22	21.50	21.15	21.32	21.53	21.40	21.13	21.11	21.16
TiO2	0.00	0.04	0.35	0.00	0.02	0.16	0.13	0.02	0.02	0.01	0.02
MgO	2.37	1.87	2.11	1.96	1.72	2.25	2.23	1.87	1.70	1.74	1.92
CaO	1.05	0.97	1.05	1.09	0.74	1.16	1.10	1.15	0.98	0.69	0.85
MnO	3.87	4.62	4.13	4.29	4.57	4.09	4.02	4.62	4.98	4.88	4.52
FeO	34.29	34.45	34.36	34.41	34.61	34.09	34.20	34.33	35.06	34.67	34.29
Total	99.30	99.55	99.57	99.33	98.87	99.50	99.59	99.89	100.11	99.15	99.13

Sample:					87-74A						
#	12	14	15	16	1	2	3	4	5	7	8
SiO2	36.09	36.50	36.31	35.97	36.75	35.96	35.62	36.80	36.26	35.63	36.27
Al2O3	20.87	21.23	21.35	21.33	20.78	21.41	21.32	20.88	20.72	21.52	21.38
TiO2	0.01	0.19	0.34	0.27	0.04	0.04	0.05	0.05	0.53	0.03	0.03
MgO	1.61	2.37	2.41	2.37	0.99	0.96	0.98	1.05	0.67	0.98	1.02
CaO	1.07	1.13	1.11	1.19	1.83	1.72	2.12	2.26	5.34	1.73	1.91
MnO	5.16	3.98	3.95	4.04	11.54	11.59	11.56	11.75	17.72	11.69	11.27
FeO	34.46	34.18	34.13	33.93	28.32	28.08	27.66	27.99	18.67	28.40	28.24
Total	99.29	99.59	99.62	99.12	100.27	99.76	99.36	100.80	99.93	99.99	100.13

Table A3.1. Garnet Compositions (Continued)

Sample:	87-74A								87-1	
#	9	10	11	12	13	14	15	17	18	2	3
SiO2	36.48	36.39	36.67	36.05	36.00	36.38	35.90	36.28	36.43	37.23	37.31
Al2O3	21.14	21.01	21.37	20.82	20.81	20.92	21.41	20.49	20.77	21.09	20.80
TiO2	0.17	0.02	0.04	0.05	0.45	0.02	0.05	0.42	0.19	0.01	0.01
MgO	1.03	1.01	0.99	0.95	0.73	0.95	1.00	0.56	0.91	2.96	2.87
CaO	2.45	1.85	2.48	2.09	4.63	1.91	2.05	6.04	3.71	1.66	1.34
MnO	13.25	11.95	11.65	11.59	16.85	11.59	11.38	19.71	12.39	11.96	12.12
FeO	26.01	27.63	27.36	27.99	20.52	28.22	27.78	15.75	24.96	25.55	26.16
Total	100.52	99.87	100.56	99.56	100.01	100.02	99.58	99.27	99.35	100.46	100.61

Sample:	87-1						86-50				
#	4	5	6	7	8	10	1	2	3	4	5
SiO2	37.35	36.96	36.60	37.17	37.96	36.58	35.89	36.74	36.52	36.81	36.56
Al2O3	20.40	20.94	20.82	20.80	20.90	21.00	20.45	20.67	20.86	21.00	20.76
TiO2	0.08	0.02	0.00	0.00	0.00	0.03	0.00	0.04	0.03	0.02	0.01
MgO	3.31	3.28	2.80	2.85	2.99	3.00	1.53	1.35	1.89	1.92	1.79
CaO	1.42	1.62	1.43	1.60	1.78	1.30	0.93	1.08	0.94	0.84	0.76
MnO	12.11	11.88	12.07	12.21	11.68	12.13	6.47	6.92	6.56	6.28	5.88
FeO	25.88	25.99	26.28	26.39	25.98	26.60	34.51	33.07	33.83	34.53	34.42
Total	100.56	100.69	99.98	101.02	101.30	100.64	99.78	99.87	100.63	101.39	100.18

Sample:	86-50						87-44				
#	6	7	8	9	10	11	1	3	2	4	5
SiO2	36.81	36.81	37.19	36.63	36.66	36.71	36.75	36.70	36.12	36.76	36.81
Al2O3	20.61	20.89	21.15	20.48	20.59	21.11	20.90	20.70	21.26	20.74	20.90
TiO2	0.03	0.00	0.01	0.01	0.00	0.01	0.00	0.04	0.01	0.04	0.01
MgO	1.88	1.65	1.47	1.55	1.67	1.53	1.56	1.39	1.56	1.95	1.97
CaO	1.06	0.98	0.95	0.87	0.94	0.89	0.77	1.09	0.62	0.71	0.79
MnO	6.82	6.09	6.64	6.35	6.24	6.69	1.03	0.94	0.95	0.80	0.88
FeO	33.58	34.44	33.86	34.40	34.21	33.74	39.91	39.73	39.91	39.07	39.24
Total	100.79	100.85	101.27	100.30	100.31	100.69	100.92	100.58	100.43	100.07	100.60

Table A3.1. Garnet Compositions (Continued)

Sample:	87-44										
#	6	7	8	9	10	11	12	13	14	15	16
SiO2	36.59	36.57	36.65	36.65	36.06	36.36	36.58	36.56	36.50	36.50	36.19
Al2O3	20.84	20.73	20.80	20.73	20.73	20.79	20.75	20.50	20.90	21.32	21.55
TiO2	0.05	0.01	0.00	0.04	0.01	0.06	0.01	0.03	0.02	0.01	0.01
MgO	1.96	1.90	1.95	1.84	1.39	1.43	1.54	1.68	1.90	2.04	2.02
CaO	0.84	0.91	0.74	1.05	0.89	1.04	1.03	0.62	0.95	1.09	0.95
MnO	0.82	0.84	0.91	1.00	0.96	1.04	1.00	1.07	1.00	1.06	1.19
FeO	39.37	39.20	39.49	38.60	39.47	39.99	39.44	39.69	39.11	38.99	38.37
Total	100.46	100.17	100.54	99.93	99.51	100.72	100.36	100.13	100.39	101.02	100.27

Sample:	87-44								87-38		
#	17	18	19	20	21	22	23	24	1	2	3
SiO2	36.31	36.24	36.19	36.39	36.15	36.21	36.50	36.57	36.66	36.72	36.82
Al2O3	21.51	21.49	21.44	21.34	21.53	20.83	20.83	20.63	20.66	20.98	20.64
TiO2	0.02	0.01	0.00	0.01	0.05	0.02	0.00	0.02	0.04	0.03	0.02
MgO	1.99	2.05	2.00	1.96	1.67	1.51	1.56	1.61	2.17	2.93	2.09
CaO	1.23	1.14	1.13	1.05	0.91	0.61	0.62	0.62	0.67	0.72	0.68
MnO	1.24	1.17	1.21	1.04	0.97	0.98	1.02	1.00	6.24	6.01	6.33
FeO	38.18	38.23	38.74	39.01	39.63	40.14	39.48	39.81	33.53	33.00	33.40
Total	100.48	100.34	100.72	100.79	100.90	100.29	100.01	100.26	99.96	100.39	99.97

Sample:	87-38					87-74A Traverse					
#	4	5	6	7	8	A	B	C	D	E	F
SiO2	36.70	36.37	36.53	37.22	36.78	36.03	36.58	36.70	36.74	36.67	36.58
Al2O3	20.93	20.84	21.12	20.90	20.92	20.82	20.25	20.28	20.05	20.14	20.10
TiO2	0.01	0.01	0.01	0.00	0.01	0.03	0.17	0.24	0.24	0.32	0.30
MgO	2.58	2.21	2.88	2.83	1.95	0.64	0.64	0.41	0.42	0.43	0.45
CaO	0.71	0.63	0.73	0.72	0.63	1.69	5.26	5.45	4.90	4.89	5.23
MnO	5.86	6.15	5.88	5.45	6.19	12.02	16.18	21.21	23.44	23.21	21.27
FeO	33.40	33.63	32.77	33.41	33.69	27.84	20.49	15.19	14.00	14.35	15.36
Total	100.19	99.84	99.92	100.53	100.18	99.06	99.57	99.48	99.79	100.02	99.28

Table A1.6. GARNET COMPOSITIONS (CONT.)

Sample:		87-51								87-140	
#	G	1	2	3	4	5	6	7	8	1	2
SiO2	37.06	37.08	37.60	36.65	36.63	37.04	37.60	36.98	37.38	36.77	37.68
Al2O3	20.37	20.93	20.65	21.31	20.27	20.48	20.78	20.54	20.85	21.06	20.63
TiO2	0.05	0.02	0.00	0.01	0.14	0.14	0.01	0.17	0.00	0.03	0.03
MgO	0.99	3.27	3.12	2.91	1.30	1.32	2.94	2.09	2.59	2.11	2.18
CaO	2.16	1.34	1.46	1.46	4.33	4.50	1.88	3.67	1.44	0.67	0.68
MnO	12.24	12.74	13.22	13.27	17.54	16.79	13.31	14.86	14.48	2.74	2.76
FeO	27.25	24.71	24.39	24.11	18.73	19.68	24.05	21.47	23.96	37.70	37.09
Total	100.12	100.08	100.44	99.72	98.94	99.93	100.55	99.80	100.69	101.08	101.04

Sample:		87-140									
#	3	5	6	7	8	10	11	12	13	14	15
SiO2	37.06	37.50	36.93	36.85	36.90	37.06	36.81	36.96	35.70	36.76	36.80
Al2O3	20.69	20.42	20.70	20.66	20.75	20.82	20.73	20.82	21.14	20.80	20.68
TiO2	0.00	0.02	0.02	0.06	0.03	0.04	0.03	0.07	0.01	0.34	0.36
MgO	2.30	2.15	1.51	1.40	1.30	1.32	1.51	1.88	1.98	2.05	1.39
CaO	0.74	0.75	1.43	1.85	2.05	1.80	1.51	1.00	0.68	0.82	1.54
MnO	3.35	2.75	9.20	9.61	9.71	9.70	8.95	5.82	2.63	4.31	9.38
FeO	37.41	36.99	30.39	29.50	29.28	29.61	30.12	34.06	37.09	35.46	29.80
Total	101.55	100.60	100.18	99.92	100.02	100.36	99.65	100.62	99.22	100.53	99.96

Sample:		87-140				88-37					
#	16	18	19	20	21	1	2	3	4	5	6
SiO2	37.01	37.15	37.17	36.83	36.83	36.68	36.76	36.68	36.57	36.81	36.68
Al2O3	20.67	20.58	20.57	20.84	20.42	20.73	20.75	20.64	20.57	20.60	20.52
TiO2	0.14	0.15	0.38	0.01	0.02	0.03	0.03	0.05	0.04	0.07	0.06
MgO	1.31	2.01	2.01	1.82	1.97	1.56	1.62	1.40	1.33	1.22	1.22
CaO	1.77	0.68	0.72	1.30	0.72	0.64	0.89	1.65	1.30	1.60	1.79
MnO	9.68	2.93	2.78	6.92	2.95	3.95	4.54	7.33	8.92	9.28	10.11
FeO	29.23	37.24	37.14	32.25	37.09	36.50	36.43	32.11	30.96	30.51	29.44
Total	99.80	100.74	100.77	99.96	99.99	100.09	101.03	99.85	99.69	100.09	99.81

Table A3.1. Garnet Compositions (Continued)

Sample:	87-104A								87-21A		
#	7	8	9	10	11	12	C.G.	N.G.	1	2	3
SiO2	36.54	36.74	36.71	36.87	36.93	36.33	39.43	36.14	36.66	36.53	36.63
Al2O3	20.58	20.60	20.62	20.76	20.84	20.52	21.97	20.20	20.50	20.39	20.54
TiO2	0.02	0.03	0.10	0.00	0.04	0.03	0.13	0.03	0.00	0.21	0.01
MgO	1.25	1.25	1.45	1.57	1.30	1.37	10.54	0.25	0.84	1.54	0.86
CaO	1.60	1.54	1.11	0.89	0.73	0.64	2.60	0.38	2.15	1.72	2.01
MnO	9.31	9.10	6.81	5.34	4.29	4.25	1.50	22.16	18.33	16.89	18.20
FeO	30.62	31.12	33.08	34.80	36.05	37.24	23.85	20.46	21.70	21.19	22.42
Total	99.92	100.38	99.87	100.22	100.19	100.38	100.01	99.62	100.18	98.47	100.67

Sample:		87-21A		83-83							
#	4	5	1	2	3	4	5	6	7	8	9
SiO2	37.03	36.79	37.23	36.97	36.78	36.88	36.81	36.80	36.49	36.38	36.86
Al2O3	20.87	20.74	20.90	20.48	20.81	20.85	20.69	20.51	20.73	20.58	20.87
TiO2	0.01	0.03	0.03	0.20	0.00	0.02	0.03	0.17	0.05	0.02	0.03
MgO	0.98	0.93	1.86	1.45	1.66	1.81	1.52	1.14	1.79	1.75	1.66
CaO	2.09	2.09	0.97	3.00	1.05	1.03	2.41	3.11	1.04	1.05	2.21
MnO	16.84	17.93	7.45	11.08	7.63	7.47	9.77	13.90	7.26	7.88	9.36
FeO	22.90	22.32	32.12	27.05	32.10	31.92	28.72	24.96	32.30	31.76	29.17
Total	100.73	100.84	100.56	100.23	100.04	99.98	99.95	100.60	99.66	99.42	100.15

Sample:	87-111										
#	1	2	3	4	5	7	8	9	10	11	12
SiO2	36.83	37.41	37.24	37.17	37.14	36.77	36.98	36.94	36.86	37.10	36.99
Al2O3	20.67	20.27	20.43	20.37	20.33	20.55	20.47	20.60	20.65	20.67	20.45
TiO2	0.03	0.08	0.05	0.06	0.05	0.00	0.05	0.01	0.03	0.03	0.04
MgO	1.36	1.03	1.10	1.14	1.22	1.13	1.34	1.30	1.18	1.14	1.15
CaO	1.89	2.26	2.25	2.03	1.91	2.00	1.99	1.90	1.87	1.93	2.06
MnO	1.50	1.42	1.36	1.39	1.37	2.76	2.04	2.51	2.77	2.78	2.66
FeO	37.69	37.59	37.88	38.01	37.52	36.03	36.65	35.92	36.39	36.20	36.17
Total	99.96	100.07	100.32	100.17	99.55	99.22	99.52	99.18	99.76	99.84	99.52

Table A3.1. Garnet Compositions (Continued)

Sample:	87-111							87-131C			
#	13	14	15	16	17	C.G.	N.G.	2	1	3	4
SiO2	36.88	36.69	36.26	36.91	37.18	39.53	36.66	36.94	37.27	36.87	37.19
Al2O3	20.47	20.71	20.91	20.48	20.50	21.85	19.89	20.89	20.79	20.94	20.88
TiO2	0.06	0.00	0.03	0.03	0.02	0.14	0.05	0.02	0.02	0.01	0.01
MgO	1.38	1.38	1.23	1.15	1.18	10.52	0.24	2.21	1.99	1.93	2.01
CaO	1.96	1.44	1.77	1.59	1.71	2.78	0.42	0.91	0.86	0.82	1.16
MnO	1.62	1.59	1.49	1.42	1.45	1.53	21.89	7.39	6.72	6.79	7.00
FeO	37.26	37.70	37.89	38.00	37.51	24.35	21.66	32.68	33.96	33.30	33.10
Total	99.63	99.51	99.59	99.58	99.54	100.69	100.81	101.03	101.60	100.66	101.34

Sample:	87-131C										
#	4	5	6	7	8	9	10	11	12	13	14
SiO2	37.16	37.02	37.05	36.93	36.87	36.87	36.65	36.88	36.54	36.82	36.60
Al2O3	20.85	20.72	20.96	20.75	20.62	20.73	21.08	20.84	20.84	21.10	21.00
TiO2	0.01	0.01	0.01	0.01	0.00	0.00	0.02	0.00	0.00	0.00	0.01
MgO	2.02	2.04	1.78	1.71	1.59	1.88	2.10	2.00	2.02	1.80	2.11
CaO	1.15	0.84	1.04	1.05	1.22	1.00	0.86	0.88	0.77	0.93	0.95
MnO	7.09	7.05	6.45	6.45	6.46	6.95	7.37	6.59	6.81	7.25	7.77
FeO	32.95	33.13	33.91	33.95	33.96	33.51	33.35	33.40	33.18	32.81	32.16
Total	101.22	100.81	101.19	100.85	100.71	100.94	101.42	100.59	100.16	100.71	100.61

Sample:	88-N2										
#	15	1	2	3	4	5	6	7	8	9	10
SiO2	36.45	36.90	36.80	37.03	37.07	37.12	37.22	36.89	37.07	37.11	37.04
Al2O3	21.01	20.85	21.04	21.12	21.06	21.04	20.89	20.93	20.93	20.88	21.16
TiO2	0.00	0.00	0.02	0.01	0.03	0.01	0.00	0.01	0.03	0.03	0.01
MgO	2.20	1.79	2.30	2.42	2.41	2.37	2.36	2.05	1.82	2.05	2.27
CaO	0.87	0.74	0.84	1.02	1.06	1.05	0.92	0.70	0.72	0.81	0.89
MnO	7.81	4.85	4.21	4.18	4.16	4.08	4.25	4.52	5.01	4.58	4.34
FeO	32.49	35.90	35.62	35.39	35.35	35.54	35.59	35.99	35.57	35.74	35.58
Total	100.84	101.03	100.81	101.18	101.13	101.22	101.23	101.09	101.14	101.19	101.28

Table A3.2. Muscovite Compositions

SAMPLE:	88-37					87-21A					87-104A
	1	2	3	4	5	1	2	3	4	3	3
SiO2	46.60	46.21	46.08	46.41	46.90	46.43	45.80	46.34	46.47	45.18	45.20
AL2O3	37.37	36.36	37.03	37.41	35.56	33.27	32.19	33.72	33.65	36.77	36.59
TiO2	0.22	0.18	0.23	0.24	0.29	0.32	0.31	0.41	0.45	0.21	0.25
FeO	1.28	1.20	1.23	1.23	1.39	2.19	2.34	1.70	1.67	1.39	1.32
MgO	0.52	0.50	0.45	0.44	0.84	1.27	1.44	1.11	1.18	0.46	0.46
Na2O	1.10	1.19	1.09	1.05	0.96	0.19	0.20	0.32	0.27	0.90	1.02
K2O	9.30	9.44	9.50	9.14	9.33	11.36	11.02	11.15	11.06	10.14	10.05
Total	96.39	95.08	95.60	95.91	95.27	95.01	93.29	94.74	94.74	95.04	94.90

SAMPLE:	87-104A			87-111				87-131C			
	4	5	6	1	2	3	4	2	3	4	5
SiO2	45.70	46.73	45.74	45.22	45.27	45.22	45.10	45.39	45.13	45.35	45.39
AL2O3	36.34	34.88	36.17	35.96	35.86	36.11	35.92	36.10	35.98	36.24	36.10
TiO2	0.33	0.31	0.28	0.54	0.46	0.46	0.48	0.44	0.36	0.44	0.46
FeO	1.43	1.80	1.35	1.24	0.94	1.03	1.17	1.16	1.19	0.96	0.97
MgO	0.65	1.10	0.57	1.10	1.00	1.22	1.13	0.52	0.48	0.57	0.49
Na2O	0.80	0.45	0.83	0.42	0.41	0.38	0.40	1.01	1.01	0.82	1.05
K2O	10.07	10.06	9.94	9.87	9.46	9.82	9.68	10.03	9.77	9.84	10.04
Total	95.31	95.33	94.87	94.35	93.41	94.24	93.87	94.65	93.91	94.21	94.51

SAMPLE:	87-87							88-N2			
	6	1	2	3	4	5	6	1	2	3	4
SiO2	45.58	46.41	47.30	46.98	45.88	46.55	45.80	46.54	46.17	46.59	46.55
AL2O3	35.97	36.27	34.18	35.01	35.97	35.13	36.10	37.42	37.06	37.15	36.57
TiO2	0.36	0.30	0.34	0.42	0.53	0.50	0.35	0.38	0.41	0.47	0.52
FeO	1.05	0.98	1.12	1.03	0.93	1.10	1.03	0.76	0.80	0.84	0.89
MgO	0.54	0.52	1.02	0.79	0.50	0.73	0.56	0.35	0.36	0.37	0.48
Na2O	1.11	1.02	0.94	0.94	1.14	0.99	1.19	1.45	1.47	1.42	1.29
K2O	9.97	9.21	9.36	9.46	9.42	9.35	9.41	9.16	9.01	9.20	9.20
Total	94.57	94.71	94.25	94.62	94.37	94.34	94.45	96.07	95.28	96.05	95.50

Table A3.2. Muscovite Compositions (Continue)

SAMPLE:	86-42										87-15d
	1	2	3	4	5	6	7	7	8	9	1
SiO2	47.86	45.70	46.18	45.57	45.92	45.60	45.70	47.44	48.01	45.98	45.55
AL2O3	33.13	34.31	34.29	34.79	33.56	34.70	34.62	32.18	31.56	34.65	36.54
TiO2	0.32	0.31	0.32	0.30	0.34	0.34	0.33	0.34	0.41	0.32	0.28
FeO	2.29	2.57	2.36	2.12	2.61	2.34	2.45	2.48	2.57	2.26	1.40
MgO	0.56	0.66	0.74	0.59	0.81	0.63	0.63	1.37	1.55	0.62	0.36
Na2O	1.38	1.28	1.08	1.05	0.99	1.30	1.25	0.75	0.72	1.32	1.72
K2O	8.89	9.10	9.59	9.38	9.98	9.19	9.18	10.09	10.30	9.53	8.97
Total	94.44	93.93	94.57	93.79	94.20	94.09	94.15	94.65	95.11	94.68	94.82

SAMPLE:	87-15d						87-58				
	1	3	4	5	6	7	1	2	3	4	5
SiO2	44.99	45.77	46.23	45.96	46.10	45.11	45.74	45.53	45.60	45.39	45.51
AL2O3	36.02	35.85	34.94	36.00	35.99	35.48	35.74	36.63	36.58	35.12	35.71
TiO2	0.29	0.26	0.31	0.29	0.28	0.28	0.37	0.36	0.21	0.45	0.42
FeO	1.34	1.37	1.85	1.32	1.62	1.53	1.73	1.58	1.51	1.39	1.44
MgO	0.31	0.43	0.74	0.53	0.54	0.44	0.48	0.50	0.42	0.54	0.51
Na2O	1.82	1.64	1.24	1.69	1.47	1.56	1.57	1.94	2.10	1.94	1.89
K2O	8.86	9.03	9.33	9.10	9.16	9.11	9.06	8.55	8.39	8.66	8.78
Total	93.63	94.35	94.63	94.89	95.16	93.50	94.70	95.09	94.81	93.49	94.25

SAMPLE:	87-58			87-55B							
	6	8	7	1	2	3	4	5	6	7	8
SiO2	45.90	46.16	44.33	45.46	45.32	45.43	45.23	45.10	44.80	45.04	45.12
AL2O3	35.38	35.63	33.32	35.75	35.83	36.13	35.71	35.78	35.88	36.14	35.79
TiO2	0.49	0.44	0.62	0.68	0.61	0.63	0.64	0.66	0.61	0.61	0.48
FeO	1.45	1.63	3.74	0.81	1.05	0.76	0.82	0.79	0.75	0.81	0.75
MgO	0.61	0.57	2.12	0.49	0.47	0.43	0.47	0.49	0.47	0.42	0.41
Na2O	1.50	1.43	1.38	1.30	1.30	1.36	1.32	1.38	1.30	1.39	1.31
K2O	9.34	9.23	9.19	9.43	9.59	9.34	9.01	9.43	9.47	9.39	9.37
Total	94.67	95.08	94.70	93.92	94.16	94.08	93.20	93.63	93.28	93.80	93.23

Table A3.2. Muscovite Compositions (Continue)

SAMPLE:	87-121A					87-120A			87-1H		
	9	2	3	6	7	1	2	3	1	2	3
SiO2	45.62	45.69	44.64	45.48	45.63	45.53	45.33	45.01	45.22	45.46	45.20
AL2O3	36.12	36.03	35.17	36.00	35.80	36.21	36.41	36.37	35.31	35.04	34.76
TiO2	0.56	0.42	0.43	0.45	0.36	0.38	0.39	0.41	0.29	0.32	0.47
FeO	1.12	1.21	1.57	0.89	0.92	0.86	0.83	0.75	2.63	2.68	2.31
MgO	0.48	0.43	0.62	0.47	0.50	0.46	0.40	0.39	0.49	0.53	0.57
Na2O	1.32	1.32	1.31	1.40	1.36	1.41	1.40	1.45	1.82	1.68	1.80
K2O	9.58	8.83	8.54	9.20	9.38	9.23	8.83	9.29	8.86	8.81	8.72
Total	94.80	93.93	92.28	93.89	93.95	94.08	93.59	93.67	94.62	94.52	93.83

SAMPLE:	87-116						87-116A				
	4	1	2	3	4	5	6	1	2	3	4
SiO2	45.02	49.67	45.87	46.08	46.18	45.75	45.88	45.63	45.49	45.68	46.04
AL2O3	34.47	33.81	36.14	36.34	36.12	36.94	36.43	36.93	36.55	36.17	36.33
TiO2	0.37	0.40	0.45	0.48	0.43	0.45	0.44	0.21	0.39	0.48	0.44
FeO	2.38	0.71	0.74	0.87	0.81	0.99	0.90	0.78	0.93	0.93	1.01
MgO	0.44	0.39	0.49	0.46	0.46	0.40	0.41	0.33	0.44	0.44	0.43
Na2O	1.85	1.27	1.41	1.36	1.35	1.51	1.43	1.60	1.34	1.38	1.42
K2O	8.69	8.54	9.35	9.37	9.43	9.33	9.34	9.39	9.34	9.42	9.23
Total	93.22	94.78	94.45	94.97	94.78	95.37	94.84	94.86	94.48	94.50	94.90

SAMPLE:	87-120					87-1				86-50	
	5	1	2	3	6	1	2	3	4	1	9
SiO2	45.79	45.93	45.85	45.95	46.42	45.43	45.11	45.55	46.15	46.30	46.57
AL2O3	36.66	36.76	36.32	36.34	36.55	34.62	34.87	35.10	34.96	36.51	37.21
TiO2	0.36	0.50	0.49	0.35	0.46	0.51	0.44	0.34	0.38	0.25	0.30
FeO	1.02	1.07	0.91	1.00	0.77	2.62	2.36	2.54	2.46	0.87	0.78
MgO	0.44	0.44	0.44	0.50	0.48	0.71	0.62	0.66	0.66	0.41	0.34
Na2O	1.47	1.34	1.24	1.05	1.27	1.56	1.49	1.60	1.64	1.68	1.63
K2O	9.05	9.51	9.27	8.37	9.38	9.17	9.14	8.93	9.23	8.94	8.94
Total	94.79	95.55	94.53	93.56	95.33	94.61	94.02	94.70	95.48	94.96	95.77

Table A3.2. Muscovite Compositions (Continue)

SAMPLE:	87-44					87-38	87-108A				
	1	2	3	4	5	1	1	2	3	4	5
SiO2	45.81	45.76	45.92	45.67	45.75	46.64	46.01	46.14	46.20	46.47	46.30
AL2O3	36.40	36.18	36.49	36.74	36.19	35.36	35.82	35.59	35.80	35.75	36.13
TiO2	0.41	0.45	0.43	0.47	0.62	0.46	0.32	0.33	0.32	0.29	0.22
FeO	1.11	1.23	1.12	1.09	1.08	1.04	1.89	2.03	2.03	1.91	2.04
MgO	0.34	0.35	0.37	0.29	0.40	0.79	0.43	0.44	0.46	0.44	0.42
Na2O	1.25	1.23	1.15	1.19	1.16	0.41	2.07	1.76	1.93	1.95	2.12
K2O	9.70	9.58	9.72	9.58	9.44	11.02	8.44	9.04	8.58	8.57	8.55
Total	95.02	94.77	95.20	95.02	94.64	95.72	94.97	95.34	95.33	95.37	95.78

SAMPLE:	87-108A				87-51						87-140
	6	7	8	9	5	6	1	2	3	4	1
SiO2	45.72	45.75	45.86	45.95	47.15	47.03	45.80	43.95	46.29	45.61	46.85
AL2O3	35.84	36.27	35.97	35.41	33.38	33.17	33.90	31.59	34.63	35.27	35.70
TiO2	0.24	0.23	0.34	0.33	0.40	0.39	0.30	0.56	0.35	0.35	0.37
FeO	1.89	1.88	2.02	1.83	2.36	2.49	2.90	4.39	2.39	2.35	1.30
MgO	0.38	0.35	0.38	0.44	1.03	1.11	0.60	3.62	0.59	0.46	0.66
Na2O	2.16	2.18	1.93	1.89	1.24	1.32	1.50	1.08	1.85	1.72	1.49
K2O	8.53	8.24	8.85	8.63	9.33	9.22	8.60	9.16	8.71	8.80	9.42
Total	94.76	94.89	95.35	94.47	94.88	94.74	93.60	94.34	94.79	94.55	95.78

SAMPLE:	87-140				87-74A						
	2	3	4	5	1	3	4	5	6	7	9
SiO2	46.30	46.91	46.37	47.86	49.55	45.23	45.29	46.03	46.61	47.08	48.56
AL2O3	37.26	36.19	36.31	34.81	31.39	33.29	33.91	34.37	33.56	33.08	31.66
TiO2	0.24	0.27	0.24	0.28	0.25	0.29	0.26	0.26	0.33	0.36	0.31
FeO	0.86	1.14	1.06	1.43	2.21	2.58	2.36	2.48	2.50	2.47	2.42
MgO	0.34	0.47	0.49	0.91	0.48	0.82	0.56	0.57	0.89	1.00	1.01
Na2O	1.88	1.41	1.47	1.19	2.52	0.58	0.70	0.62	0.61	0.63	0.59
K2O	8.70	9.39	9.25	9.61	8.19	10.27	10.05	10.34	10.18	10.22	9.96
Total	95.56	95.77	95.21	96.09	94.58	93.07	93.13	94.66	94.68	94.84	94.50

Table A3.3. Plagioclase Compositions

SAMPLE:	87-55B							87-121A				
	1	2	3	4	5	6	7	1	2	3	4	5
SiO2	63.47	63.79	64.10	64.20	63.88	65.30	63.60	62.34	60.95	62.22	62.32	62.23
Al203	22.65	22.56	22.60	22.52	22.67	22.08	22.49	23.35	24.50	23.43	23.35	23.68
Fe2O3	0.03	0.01	0.02	0.04	0.01	0.02	0.03	0.10	0.13	0.09	0.04	0.12
CaO	3.33	3.40	3.45	3.46	3.42	3.38	3.43	4.16	5.73	4.48	4.21	4.73
Na2O	9.87	9.57	9.71	9.69	9.76	9.43	9.65	9.28	8.41	9.12	9.15	8.93
K2O	0.07	0.06	0.04	0.06	0.05	0.03	0.04	0.06	0.05	0.06	0.05	0.04
TOTAL	99.41	99.38	99.92	99.97	99.79	100.24	99.24	99.30	99.77	99.41	99.13	99.72

SAMPLE:	87-121A		87-120A								87-120	
	6	7	1	2	3	4	5	6	7	8	1	2
SiO2	62.95	62.93	64.21	64.23	64.55	64.15	64.10	64.82	64.82	63.76	64.32	64.67
Al203	23.25	23.30	22.10	22.07	22.03	22.06	22.24	21.91	22.10	22.06	22.54	22.72
Fe2O3	0.12	0.08	0.04	0.02	0.09	0.09	0.05	0.09	0.08	0.09	0.06	0.10
CaO	4.12	4.20	2.82	2.82	2.62	2.61	2.69	2.66	2.74	2.61	3.35	3.09
Na2O	9.20	9.27	10.14	10.28	10.22	10.33	10.08	9.92	10.00	10.10	9.83	9.89
K2O	0.06	0.08	0.08	0.05	0.05	0.05	0.07	0.07	0.06	0.08	0.05	0.06
TOTAL	99.70	99.85	99.39	99.47	99.56	99.29	99.22	99.46	99.81	98.70	100.14	100.53

SAMPLE:	87-120								87-116			
	3	5	6	7	8	9	10	11	1	2	3	4
SiO2	64.08	64.37	64.19	64.34	64.28	64.29	64.82	64.50	63.27	63.76	63.45	63.35
Al203	22.51	22.55	22.41	22.36	22.20	22.32	22.39	22.23	22.67	22.78	22.67	22.72
Fe2O3	0.07	0.08	0.07	0.07	0.08	0.06	0.11	0.07	0.25	0.31	0.27	0.42
CaO	3.49	3.19	3.19	3.08	3.15	3.49	3.13	3.13	3.61	3.59	3.54	3.60
Na2O	9.46	10.00	9.70	9.78	9.79	9.71	9.87	9.87	9.69	9.76	9.81	9.71
K2O	0.08	0.07	0.05	0.03	0.03	0.07	0.05	0.05	0.05	0.04	0.05	0.05
TOTAL	99.69	100.26	99.60	99.66	99.51	99.93	100.36	99.85	99.54	100.24	99.80	99.86

Table A3.3. Plagioclase Compositions (Continued)

SAMPLE:	87-116A				87-42							
	1	2	3	4	1	2	3	4	5	6	7	8
SiO2	63.15	62.66	62.92	63.18	63.10	62.70	63.40	63.71	62.51	62.36	63.31	62.27
Al203	23.32	23.32	23.25	23.35	23.21	23.43	23.08	23.22	23.79	23.37	23.38	23.82
Fe2O3	0.48	0.51	0.32	0.38	0.20	0.10	0.15	0.15	0.13	0.17	0.09	0.17
CaO	4.18	4.12	4.13	4.09	4.24	4.35	4.19	4.04	5.05	4.76	4.21	4.52
Na2O	9.08	9.67	9.24	9.21	9.13	8.61	9.01	9.44	8.87	8.67	9.37	9.22
K2O	0.04	0.06	0.04	0.07	0.15	0.36	0.16	0.16	0.14	0.11	0.13	0.13
TOTAL	100.24	100.34	99.90	100.28	100.03	99.54	100.00	100.74	100.49	99.44	100.49	100.12

SAMPLE:	87-44								86-50			86-1
	1	2	3	4	5	6	7	8	1	2	3	7
SiO2	63.79	64.69	64.30	64.63	64.46	64.06	64.31	64.21	64.36	62.83	64.36	62.45
Al203	22.46	22.09	22.38	22.51	22.42	22.20	22.49	22.70	22.63	23.31	22.29	23.91
Fe2O3	0.37	0.31	0.10	0.17	0.13	0.45	0.07	0.19	0.00	0.04	0.04	0.06
CaO	3.24	3.31	3.34	3.28	3.47	3.30	3.28	3.35	3.29	4.24	3.15	4.87
Na2O	9.95	9.53	9.75	9.66	9.62	9.57	9.94	9.88	9.93	9.42	10.09	9.20
K2O	0.03	0.05	0.05	0.05	0.08	0.06	0.07	0.06	0.05	0.04	0.07	0.03
TOTAL	99.83	99.98	99.91	100.31	100.18	99.64	100.16	100.40	100.26	99.89	100.00	100.52

SAMPLE:	86-1								87-108a			87-51
	8	9	10	11	12	13	14	15	2	3	4	1
SiO2	62.31	62.31	62.20	61.79	61.70	61.84	61.75	62.04	63.88	63.68	64.08	61.94
Al203	23.99	24.19	23.62	23.85	23.79	23.83	23.63	23.85	22.15	22.50	22.02	23.19
Fe2O3	0.18	0.23	0.13	0.11	0.12	0.14	0.32	0.16	0.02	0.00	0.03	0.09
CaO	5.03	5.02	4.56	4.80	4.57	4.62	4.52	4.75	3.22	3.62	3.41	4.75
Na2O	9.10	9.32	9.43	9.38	9.41	9.21	9.31	9.30	10.00	9.76	9.79	8.68
K2O	0.04	0.04	0.03	0.03	0.05	0.04	0.03	0.04	0.04	0.05	0.03	0.04
TOTAL	100.66	101.11	99.98	99.96	99.64	99.68	99.55	100.14	99.30	99.62	99.36	98.69

Table A3.3. Plagioclase Compositions (Continued)

SAMPLE:	87-51					87-74A						
	2	3	4	5	6	2	3	4	5	6	7	8
SiO2	62.02	61.68	61.37	62.08	61.61	63.84	63.11	61.21	64.49	61.88	61.22	60.73
Al203	23.89	24.17	24.29	24.08	23.95	22.82	23.23	24.19	22.73	23.85	24.72	24.43
Fe2O3	0.07	0.14	0.13	0.04	0.00	0.17	0.26	0.13	0.30	0.25	0.07	0.49
CaO	4.91	5.14	5.18	4.99	5.04	3.41	4.26	5.31	3.47	4.82	5.82	4.87
Na2O	8.77	8.89	8.73	8.94	8.69	9.72	9.31	8.59	9.76	8.95	8.34	8.30
K2O	0.08	0.04	0.04	0.10	0.06	0.08	0.04	0.06	0.05	0.05	0.03	0.68
TOTAL	99.74	100.04	99.74	100.23	99.35	100.04	100.20	99.49	100.79	99.80	100.21	99.49

SAMPLE:	87-74A		88-37		87-140							
	9	10	1	5	1	2	3	4	5	1	2	3
SiO2	61.33	61.77	68.71	67.40	66.79	66.28	65.09	65.63	65.57	62.78	62.56	62.05
Al203	24.46	23.89	19.41	19.89	21.15	21.48	22.19	21.93	21.62	24.20	23.84	23.92
Fe2O3	0.05	0.08	0.19	0.43	0.24	0.22	0.16	0.16	0.34	0.02	0.23	0.15
CaO	5.58	5.04	0.12	0.49	2.05	2.32	3.31	2.98	2.67	4.72	4.68	4.78
Na2O	8.58	8.72	11.66	11.41	10.49	10.63	9.90	10.26	10.24	8.78	9.00	9.08
K2O	0.00	0.04	0.04	0.14	0.04	0.04	0.03	0.05	0.05	0.06	0.08	0.05
TOTAL	100.07	99.54	100.13	99.76	100.75	100.96	100.69	101.01	100.48	100.56	100.39	100.02

SAMPLE:	87-111			87-131C								88-N2
	4	5	6	1	2	3	4	5	6	7	8	1
SiO2	62.77	62.11	61.67	64.15	63.80	62.48	62.42	63.31	62.33	63.88	63.50	65.86
Al203	24.37	24.34	24.06	23.51	23.56	23.98	24.42	23.26	23.80	23.39	23.62	22.36
Fe2O3	0.00	0.09	0.29	0.03	0.00	0.15	0.10	0.15	0.17	0.21	0.09	0.31
CaO	4.76	5.03	4.96	3.83	3.95	4.50	4.66	3.83	4.30	3.78	3.95	3.21
Na2O	8.87	8.76	8.91	9.41	9.57	9.14	8.72	9.46	9.01	9.25	9.43	9.99
K2O	0.05	0.08	0.07	0.05	0.03	0.04	0.05	0.05	0.05	0.07	0.07	0.04
TOTAL	100.81	100.41	99.97	100.96	100.91	100.29	100.37	100.05	99.66	100.58	100.67	101.77

Table A3.3. Plagioclase Compositions (Continued)

SAMPLE:	88-N2					87-87					86-42	
	2	3	4	5	6	1	2	3	4	5	7	1
SiO2	64.55	64.93	65.11	65.48	65.23	62.22	61.36	62.05	62.33	61.05	62.04	64.24
Al203	22.45	22.19	22.14	22.20	22.21	24.41	23.97	24.46	24.44	24.32	23.97	22.36
Fe2O3	0.37	0.19	0.23	0.24	0.41	0.21	0.20	0.24	0.16	0.20	0.12	0.16
CaO	3.26	3.20	3.05	3.07	2.98	5.75	5.58	5.60	5.66	5.87	5.72	3.89
Na2O	9.88	10.04	9.85	10.20	9.92	8.51	8.31	8.39	8.09	8.29	8.59	9.25
K2O	0.06	0.02	0.03	0.03	0.06	0.06	0.03	0.06	0.06	0.07	0.05	0.04
TOTAL	100.57	100.57	100.41	101.22	100.82	101.15	99.44	100.80	100.74	99.80	100.48	99.94

SAMPLE:	86-42						87-58					
	2	3	4	5	6	7	1	2	3	4	5	6
SiO2	63.75	63.16	64.12	64.14	62.37	62.91	63.49	63.57	64.26	64.15	63.69	63.76
Al203	23.07	22.81	22.89	22.38	22.91	22.40	21.93	23.47	22.40	22.59	23.03	23.24
Fe2O3	0.09	0.19	0.25	0.10	0.05	0.04	1.53	0.17	0.30	0.61	0.31	0.19
CaO	4.56	4.48	4.25	4.07	4.67	4.25	2.94	4.25	3.34	3.84	3.92	4.21
Na2O	8.81	9.12	9.07	9.27	8.92	9.31	9.61	9.44	9.90	9.56	9.58	9.35
K2O	0.04	0.07	0.06	0.03	0.04	0.04	0.09	0.04	0.13	0.10	0.06	0.05
TOTAL	100.31	99.82	100.63	99.99	98.96	98.95	99.60	100.93	100.32	100.85	100.59	100.79

SAMPLE:	87-58			87-15d							
	7	8	9	1	2	3	4	5	6	7	8
SiO2	64.17	64.25	63.08	63.93	61.69	63.28	63.93	64.40	63.93	63.96	64.60
Al203	22.87	23.49	23.09	23.00	23.16	22.51	22.21	22.30	23.10	22.52	22.53
Fe2O3	0.18	0.16	0.08	0.27	0.25	0.08	0.18	0.17	0.23	0.06	0.13
CaO	4.04	4.17	4.30	3.78	4.86	3.79	3.64	3.37	4.22	3.77	3.44
Na2O	9.72	9.38	9.22	9.54	9.13	9.85	10.01	9.85	9.35	9.64	9.72
K2O	0.08	0.05	0.05	0.04	0.04	0.06	0.03	0.04	0.03	0.01	0.02
TOTAL	101.06	101.50	99.81	100.55	99.14	99.57	100.00	100.13	100.86	99.95	100.43

Table A3.4. Staurolite Compositions

SAMPLE:	86-50						87-112A				
	1	2	5	3	4	6	1	2	3	4	5
SiO2	26.28	27.51	27.23	27.36	27.00	27.66	27.03	27.23	27.08	27.21	26.88
Al203	55.02	54.08	53.82	53.42	54.03	53.81	52.93	53.45	53.44	53.25	53.41
Cr2O3	0.10	0.04	0.03	0.07	0.03	0.00	0.07	0.07	0.03	0.03	0.03
TiO2	0.44	0.42	0.42	0.45	0.39	0.46	0.53	0.47	0.55	0.56	0.54
MgO	1.03	1.13	1.23	1.02	1.13	1.21	1.34	1.27	1.44	1.42	1.50
FeO	13.90	13.58	13.78	13.75	13.99	13.58	14.05	14.00	13.98	13.89	13.81
MnO	0.35	0.23	0.38	0.34	0.31	0.39	0.26	0.23	0.21	0.21	0.21
ZnO	0.80	0.87	0.84	0.78	0.87	0.78	1.18	1.17	1.12	1.07	1.15
TOTAL	97.92	97.86	97.73	96.73	97.36	97.42	97.38	97.89	97.85	97.64	97.53

SAMPLE:	87-121A						86-22				
	1	2	3	4	5	6	3	4	5	6	7
SiO2	27.44	27.72	27.17	27.34	27.00	27.20	27.36	27.25	27.43	27.03	27.28
Al203	53.04	53.50	53.19	53.43	53.77	53.50	53.18	52.48	53.40	53.52	52.60
Cr2O3	0.05	0.08	0.03	0.02	0.04	0.04	0.00	0.09	0.04	0.03	0.02
TiO2	0.59	0.55	0.56	0.57	0.53	0.59	0.41	0.39	0.36	0.45	0.55
MgO	1.32	1.36	1.42	1.51	1.51	1.51	1.43	1.45	1.52	1.56	1.59
FeO	14.32	14.39	14.17	14.44	14.23	14.25	14.88	14.76	14.96	14.72	15.22
MnO	0.28	0.27	0.22	0.25	0.24	0.28	0.33	0.42	0.43	0.31	0.37
ZnO	0.64	0.51	0.62	0.53	0.56	0.65	0.48	0.68	0.48	0.45	0.46
TOTAL	97.68	98.37	97.39	98.09	97.87	98.01	98.07	97.52	98.62	98.07	98.09

SAMPLE:	86-22						86-30A				
	8	9	10	11	12	4	5	6	7	9	10
SiO2	27.43	27.14	27.23	27.38	26.97	27.27	27.04	26.90	27.06	27.08	26.28
Al203	53.13	53.41	53.15	52.96	52.56	53.77	53.69	53.27	53.80	54.50	54.37
Cr2O3	0.09	0.07	0.05	0.07	0.06	0.01	0.00	0.02	0.02	0.01	0.01
TiO2	0.51	0.45	0.53	0.54	0.41	0.48	0.48	0.52	0.53	0.54	0.54
MgO	1.54	1.54	1.50	1.47	1.58	1.25	1.39	1.26	1.33	1.54	1.50
FeO	15.01	14.83	15.13	15.21	14.75	14.44	14.44	15.04	14.66	14.88	14.57
MnO	0.38	0.43	0.42	0.38	0.45	0.32	0.29	0.33	0.30	0.28	0.27
ZnO	0.33	0.55	0.49	0.50	0.49	0.75	0.70	0.87	0.74	0.58	0.53
TOTAL	98.42	98.42	98.50	98.51	97.27	98.29	98.03	98.21	98.44	99.41	98.07

Table A3.4. Staurolite Compositions (Continued)

SAMPLE:	87-108A				87-51						
	1	3	2	4	1	2	3	4	5	6	7
SiO2	27.45	27.47	26.97	26.82	28.05	27.73	27.78	27.78	27.48	28.27	28.25
Al203	52.76	52.26	53.44	53.96	54.09	54.74	54.29	54.44	55.40	54.40	54.45
Cr2O3	0.02	0.06	0.02	0.02	0.08	0.11	0.04	0.01	0.08	0.08	0.07
TiO2	0.25	0.47	0.55	0.49	0.72	0.48	0.48	0.48	0.64	0.79	0.51
MgO	1.73	1.51	1.54	1.46	1.70	1.71	1.97	1.90	1.61	1.72	1.65
FeO	14.84	14.72	15.04	14.96	10.36	10.31	10.60	10.56	9.66	10.30	9.96
MnO	0.25	0.25	0.24	0.26	0.85	0.87	0.91	0.90	0.88	0.87	0.84
ZnO	0.25	0.18	0.30	0.22	1.57	1.76	1.74	1.53	1.89	1.77	1.81
TOTAL	97.55	96.92	98.10	98.19	97.42	97.71	97.80	97.59	97.63	98.19	97.53

SAMPLE:	87-51		87-140					87-87			
	8	8	1	2	3	4	5	1	2	3	4
SiO2	27.92	27.80	27.60	27.54	27.37	27.29	28.13	27.62	27.33	27.78	27.87
Al203	54.38	55.00	52.61	52.74	53.25	53.67	52.83	53.34	53.14	53.98	53.40
Cr2O3	0.12	0.00	0.02	0.06	0.07	0.04	0.00	0.00	0.00	0.00	0.00
TiO2	0.82	0.40	0.50	0.43	0.52	0.57	0.46	0.60	0.55	0.62	0.61
MgO	1.65	1.70	1.32	1.30	1.26	1.51	1.50	1.62	1.60	1.39	1.62
FeO	10.03	10.10	14.38	14.40	14.25	14.20	14.49	14.01	14.39	14.35	14.69
MnO	0.91	0.80	0.13	0.14	0.14	0.12	0.11	0.15	0.18	0.14	0.16
ZnO	1.88	2.00	0.77	0.83	0.91	0.78	0.79	0.28	0.31	0.28	0.42
TOTAL	97.70	97.80	97.32	97.42	97.78	98.17	98.32	97.61	97.51	98.54	98.77

SAMPLE:	87-87		88-N2								
	5	6	1	2	3	4	5	6	7	8	9
SiO2	27.90	27.22	27.09	26.75	26.93	27.20	27.72	26.99	26.56	27.33	26.93
Al203	53.41	52.67	54.16	54.29	54.08	54.04	54.38	54.10	53.93	54.38	54.24
Cr2O3	0.00	0.00	0.00	0.00	0.00	0.00	0.00	0.00	0.00	0.00	0.00
TiO2	0.69	0.66	0.55	0.53	0.57	0.57	0.51	0.53	0.53	0.56	0.55
MgO	1.41	1.52	1.39	1.37	1.37	1.30	1.32	1.39	1.37	1.16	1.38
FeO	14.35	14.61	13.89	14.26	13.95	13.90	14.04	13.88	14.05	13.54	14.00
MnO	0.14	0.20	0.25	0.24	0.26	0.23	0.25	0.24	0.25	0.27	0.24
ZnO	0.37	0.26	1.39	1.49	1.48	1.36	1.43	1.32	1.50	1.35	1.52
TOTAL	98.26	97.14	98.72	98.92	98.63	98.60	99.64	98.44	98.19	98.58	98.85

Table A3.4. Staurolite Compositions (Continued)

SAMPLE:	87-15D							87-58			
	10	1	2	3	4	5	6	1	2	3	4
SiO2	27.17	26.69	26.68	27.09	27.29	27.16	26.98	26.83	27.17	26.85	26.87
Al203	53.41	54.54	53.98	54.82	54.97	54.44	54.55	54.79	53.74	54.31	54.47
Cr2O3	0.00	0.04	0.03	0.05	0.03	0.03	0.04	0.03	0.08	0.05	0.01
TiO2	0.56	0.45	0.48	0.47	0.46	0.42	0.45	0.53	0.62	0.55	0.42
MgO	1.50	1.42	1.58	1.32	1.46	1.44	1.44	1.51	1.58	1.50	1.53
FeO	14.11	14.56	14.43	14.28	14.56	14.50	14.46	13.32	13.31	13.29	13.24
MnO	0.25	0.15	0.18	0.18	0.25	0.18	0.19	0.46	0.46	0.43	0.48
ZnO	1.30	0.69	0.71	0.73	0.70	0.77	0.72	1.02	0.89	0.96	1.16
TOTAL	98.30	98.54	98.07	98.94	99.72	98.93	98.84	98.47	97.84	97.93	98.19

SAMPLE:	87-58	
	5	6
SiO2	27.05	26.95
Al203	53.57	54.17
Cr2O3	0.02	0.04
TiO2	0.52	0.53
MgO	1.54	1.53
FeO	13.15	13.26
MnO	0.45	0.46
ZnO	1.04	1.01
TOTAL	97.34	97.95

Table A3.5. Chlorite Compositions

SAMPLE:	87-1		86-50			87-108A				87-74A	
	1	6	2	3	4	1	2	3	4	1	2
SiO2	25.18	25.33	23.06	23.29	23.63	23.44	23.76	23.81	23.73	23.42	24.59
Al203	23.31	22.85	23.09	22.75	22.51	23.01	22.71	22.67	22.83	21.91	21.89
TiO2	0.00	0.07	0.13	0.11	0.08	0.06	0.10	0.10	0.07	0.08	0.08
MgO	19.15	19.09	11.60	11.87	11.93	14.24	14.35	14.51	14.48	11.80	11.22
FeO	19.46	18.94	28.57	28.71	28.17	26.00	25.95	25.80	25.25	29.44	28.47
MnO	0.23	0.26	0.18	0.27	0.19	0.12	0.14	0.14	0.18	0.40	0.35
CaO	0.00	0.03	0.01	0.00	0.00	0.01	0.00	0.01	0.01	0.00	0.02
TOTAL	87.32	86.56	86.64	86.99	86.51	86.89	87.01	87.04	86.55	87.04	86.62

SAMPLE:	87-74A				87-51A						
	3	4	5	AVG	1	2	3	4	5	6	AVG
SiO2	23.25	23.63	23.30	23.64	25.13	25.65	24.97	25.21	25.30	25.08	25.22
Al203	22.04	21.94	21.71	21.90	23.80	23.38	23.74	23.03	23.08	23.03	23.34
TiO2	0.08	0.08	0.07	0.08	0.08	0.04	0.05	0.06	0.09	0.08	0.07
MgO	11.77	11.51	11.62	11.58	20.31	20.76	20.08	20.38	20.23	20.16	20.32
FeO	29.04	29.38	29.65	29.20	17.15	16.61	17.22	17.56	17.39	17.56	17.25
MnO	0.31	0.38	0.39	0.37	0.42	0.37	0.40	0.48	0.43	0.43	0.42
CaO	0.03	0.01	0.01	0.01	0.02	0.01	0.01	0.00	0.03	0.02	0.01
TOTAL	86.52	86.92	86.76	86.77	86.90	86.81	86.47	86.72	86.55	86.36	86.63

SAMPLE:	87-104A						86-42				
	1	2	3	4	5	AVG	1	2	3	4	5
SiO2	23.97	23.77	23.91	24.34	23.73	23.94	24.75	27.22	24.91	24.52	24.92
Al203	22.50	22.31	22.10	22.06	22.72	22.34	22.86	22.12	22.35	22.46	22.28
TiO2	0.06	0.07	0.14	0.07	0.07	0.08	0.09	0.06	0.05	0.06	0.09
MgO	13.78	13.72	13.76	13.98	13.44	13.74	16.58	16.38	16.75	16.51	16.71
FeO	26.38	26.54	26.44	26.39	26.51	26.45	23.04	21.94	22.82	23.36	22.83
MnO	0.22	0.22	0.20	0.16	0.18	0.20	0.29	0.23	0.30	0.30	0.33
CaO	0.00	0.00	0.00	0.00	0.00	0.00	0.01	0.01	0.01	0.02	0.01
TOTAL	86.90	86.63	86.55	87.01	86.66	86.75	87.62	87.96	87.18	87.22	87.16

Table A3.5. Chlorite Compositions (Continued)

SAMPLE:	86-42		87-15d					87-58			
	6	AVG	1	2	3	4	avg	1	2	3	4
SiO2	24.88	25.20	23.72	23.80	23.87	23.34	23.68	36.24	35.60	24.12	25.21
Al203	22.56	22.44	23.20	23.22	22.92	23.06	23.10	32.24	30.39	22.62	23.44
TiO2	0.08	0.07	0.09	0.09	0.10	0.07	0.09	0.64	1.59	0.08	0.07
MgO	16.35	16.55	14.11	14.24	14.56	14.03	14.24	7.19	6.07	15.85	14.83
FeO	23.28	22.88	25.94	26.08	25.77	25.75	25.88	7.26	9.54	23.31	23.72
MnO	0.29	0.29	0.12	0.10	0.12	0.12	0.12	0.25	0.40	0.25	0.29
CaO	0.02	0.01	0.00	0.01	0.00	0.00	0.00	0.87	0.15	0.02	0.02
TOTAL	87.45	87.43	87.18	87.53	87.34	86.38	87.11	84.69	83.75	86.25	87.58

SAMPLE:	87-58					
	5	6	7	8	9	avg
SiO2	24.67	24.25	24.57	24.21	24.30	27.02
Al203	23.20	22.81	22.57	22.60	22.73	24.73
TiO2	0.11	0.11	0.12	0.08	0.10	0.32
MgO	15.82	15.77	15.93	15.87	15.74	13.67
FeO	23.42	23.37	23.43	23.05	23.63	20.08
MnO	0.28	0.22	0.23	0.23	0.24	0.27
CaO	0.00	0.00	0.02	0.02	0.00	0.12
TOTAL	87.50	86.54	86.86	86.05	86.75	86.22

Table A3.6 Biotite Compositions

SAMPLE:	87-121AA										
	1	2	3	4	5	6	7	8	9	10	11
SiO2	35.45	35.37	35.35	35.42	35.25	34.91	34.76	35.29	34.94	35.20	35.16
AL2O3	18.96	18.93	18.90	19.08	18.97	18.80	18.87	19.32	18.97	19.55	19.08
TiO2	2.03	2.06	2.00	1.98	2.11	2.15	2.26	2.17	2.13	2.12	1.98
FeO	20.80	20.79	20.45	21.10	21.35	21.14	21.49	20.65	21.53	20.67	21.22
MnO	0.05	0.11	0.07	0.02	0.19	0.13	0.09	0.02	0.09	0.13	0.10
MgO	8.99	8.92	9.24	8.75	8.50	8.59	8.89	8.73	9.02	8.56	8.60
Na2O	0.25	0.29	0.24	0.28	0.26	0.24	0.23	0.26	0.25	0.29	0.21
K2O	9.07	9.13	9.28	8.91	9.00	9.07	8.98	8.99	8.91	8.81	8.84
Total	95.60	95.60	95.55	95.53	95.63	95.03	95.57	95.43	95.83	95.32	95.17

SAMPLE:	87-121AA				86-22			87-14A			
	12	13	14	15	1	4	5	1	2	3	4
SiO2	34.94	34.75	35.25	35.27	34.90	34.73	34.91	34.63	35.34	34.67	34.74
AL2O3	19.40	19.83	19.70	19.83	19.01	19.37	19.81	19.25	19.80	19.23	18.90
TiO2	1.55	1.39	1.35	1.47	1.73	1.80	1.58	1.49	1.49	1.44	1.61
FeO	21.27	20.19	21.24	19.83	21.89	20.56	20.99	20.71	20.64	21.35	20.82
MnO	0.07	0.10	0.10	0.05	0.09	0.06	0.11	0.03	0.10	0.10	0.06
MgO	8.74	9.10	9.10	8.96	8.23	8.54	8.33	8.85	8.67	8.88	8.90
Na2O	0.28	0.28	0.31	0.29	0.25	0.25	0.25	0.27	0.29	0.26	0.24
K2O	8.95	8.64	9.04	9.11	9.04	9.14	9.03	8.94	9.03	8.88	8.96
Total	95.20	94.28	96.09	94.81	95.12	94.44	95.00	94.15	95.34	94.81	94.23

SAMPLE:	87-14A					87-120A			86-47A		
	5	6	8	9	10	1	2	3	1	2	3
SiO2	34.99	34.70	34.73	34.96	34.81	34.29	34.29	34.61	34.00	34.10	33.97
AL2O3	19.34	19.01	18.87	19.51	19.57	19.23	19.27	19.45	19.29	19.11	19.11
TiO2	1.41	1.65	1.63	1.46	1.58	2.05	2.04	1.93	1.92	1.97	1.91
FeO	21.20	21.78	21.29	20.12	21.21	20.76	20.70	20.70	21.48	21.38	21.40
MnO	0.10	0.09	0.14	0.12	0.13	0.08	0.09	0.10	0.03	0.08	0.10
MgO	8.63	8.98	8.75	8.41	8.49	8.21	8.18	8.14	8.16	8.07	8.15
Na2O	0.27	0.30	0.32	0.25	0.26	0.26	0.27	0.26	0.30	0.26	0.33
K2O	8.63	8.98	8.75	8.85	8.99	9.24	9.05	9.14	8.71	8.83	8.78
Total	94.56	95.49	94.48	93.67	95.04	94.11	93.89	94.31	93.89	93.79	93.74

Table A3.6 Biotite Compositions (Continued)

SAMPLE:	86-47A		87-74A								
	4	6	1	2	3	4	6	7	8	9	10
SiO2	34.40	34.08	34.65	34.38	34.86	34.37	35.58	34.92	34.62	34.99	34.64
AL2O3	19.10	19.00	17.64	18.27	17.72	17.88	17.77	18.06	17.90	17.64	17.74
TiO2	1.95	1.93	1.66	1.58	1.70	1.67	1.78	1.63	1.76	1.76	1.74
FeO	21.44	21.68	21.73	21.46	21.87	22.41	20.83	21.88	21.43	21.50	21.85
MnO	0.08	0.06	0.22	0.20	0.19	0.27	0.17	0.25	0.20	0.18	0.10
MgO	8.79	8.04	8.34	8.57	8.43	8.47	8.22	8.27	8.32	8.56	8.39
Na2O	0.26	0.26	0.14	0.24	0.14	0.11	0.11	0.06	0.14	0.10	0.10
K2O	8.79	8.74	9.41	8.96	9.73	9.35	9.52	9.37	9.48	9.77	9.68
Total	94.80	93.80	93.81	93.67	94.65	94.52	94.00	94.43	93.85	94.50	94.24

SAMPLE:	87-74A		87-1					87-44			
	11	12	1	2	3	4	6	1	2	4	5
SiO2	34.49	34.93	37.04	37.53	37.32	36.88	38.08	34.17	33.38	34.12	33.97
AL2O3	17.75	17.90	18.53	18.59	18.75	18.66	18.62	19.88	19.56	19.25	19.44
TiO2	1.69	1.65	1.41	1.37	1.36	1.48	1.30	1.53	1.76	2.28	2.26
FeO	22.19	21.29	15.77	14.91	14.72	15.48	15.27	24.71	25.02	25.46	24.78
MnO	0.18	0.17	0.14	0.18	0.09	0.15	0.15	0.00	0.02	0.05	0.02
MgO	8.47	8.60	13.35	13.38	13.42	13.43	13.59	6.39	6.06	6.10	5.93
Na2O	0.14	0.14	0.24	0.31	0.34	0.31	0.31	0.22	0.21	0.24	0.24
K2O	9.36	9.45	9.30	9.33	9.37	9.30	9.33	9.05	8.68	9.03	9.04
Total	94.28	94.12	95.77	95.59	95.38	95.69	96.64	95.95	94.70	96.52	95.69

SAMPLE:	87-44				87-42					86-50	
	6	7	8	9	1	2	3	4	5	3	5
SiO2	34.12	34.23	33.99	33.95	35.42	35.56	34.74	35.07	35.09	34.98	35.39
AL2O3	18.91	19.79	19.88	19.60	18.37	18.50	19.59	19.27	19.16	19.22	19.13
TiO2	2.26	1.91	1.63	1.63	2.99	3.18	2.30	2.50	2.55	1.42	1.51
FeO	24.87	24.82	24.40	24.71	20.29	20.14	19.78	19.27	19.16	22.47	22.28
MnO	0.04	0.03	0.00	0.06	0.15	0.12	0.18	0.11	0.22	0.08	0.09
MgO	6.18	6.44	6.60	6.42	8.53	8.50	8.55	8.51	8.40	8.64	8.37
Na2O	0.25	0.19	0.21	0.24	0.05	0.08	0.11	0.09	0.06	0.22	0.17
K2O	9.09	9.05	8.84	8.96	9.68	9.83	9.82	9.94	9.81	8.94	8.99
Total	95.71	96.45	95.54	95.58	95.48	95.92	95.07	94.75	94.46	95.97	95.93

Table A3.6 Biotite Compositions (Continued)

SAMPLE:	87-50			87-108A						
	6	7	8	1	2	3	4	5	6	7	8
SiO2	35.06	35.16	34.65	35.62	35.64	35.52	35.69	35.57	35.84	35.87	35.52
AL2O3	19.28	19.33	19.36	18.84	18.89	18.57	18.83	18.83	18.95	19.05	18.80
TiO2	1.44	1.54	1.48	1.62	1.64	1.63	1.63	1.60	1.53	1.58	1.78
FeO	21.98	21.72	22.21	20.13	20.18	19.72	20.35	20.32	20.38	19.41	20.04
MnO	0.06	0.12	0.13	0.00	0.15	0.12	0.00	0.01	0.08	0.07	0.12
MgO	8.41	8.30	8.39	9.95	9.94	10.01	9.72	9.79	9.75	9.81	10.00
Na2O	0.18	0.17	0.17	0.30	0.32	0.26	0.29	0.32	0.32	0.30	0.27
K2O	9.20	9.22	8.99	9.21	9.37	9.25	9.32	9.22	9.22	9.38	9.26
Total	95.60	95.56	95.38	95.67	96.13	95.08	95.83	95.66	96.07	95.47	95.81

SAMPLE:	87-108A		87-51					87-140		
	9	10	1	2	3	4	5	6	1	2	3
SiO2	35.45	35.84	36.99	37.26	36.97	37.15	36.20	37.05	35.69	34.27	35.68
AL2O3	18.66	18.47	18.24	18.36	18.52	18.42	18.20	18.22	19.45	19.44	19.02
TiO2	1.62	1.82	1.27	1.21	1.24	1.24	1.30	1.30	1.42	1.32	1.42
FeO	20.05	20.39	14.12	13.59	14.11	13.98	14.10	14.17	20.42	20.70	20.73
MnO	0.09	0.12	0.26	0.14	0.18	0.21	0.20	0.21	0.05	0.06	0.08
MgO	10.32	9.92	14.75	14.36	14.46	14.51	14.60	14.42	9.32	9.77	9.46
Na2O	0.24	0.26	0.19	0.25	0.30	0.21	0.10	0.24	0.29	0.26	0.24
K2O	9.21	9.29	9.58	9.37	9.27	9.49	9.00	9.22	9.01	8.24	9.16
Total	95.65	96.12	95.39	94.53	95.04	95.21	93.70	94.83	95.65	94.07	95.78

SAMPLE:	87-140						88-37				
	4	5	6	7	8	9	1	2	3	4	5
SiO2	34.89	35.71	35.46	35.61	35.32	35.46	35.14	35.06	34.09	35.30	34.59
AL2O3	19.28	19.25	19.23	19.62	19.30	19.52	18.69	19.41	19.49	18.84	19.44
TiO2	1.47	1.46	1.46	1.44	1.43	1.36	1.45	1.47	1.46	1.45	1.47
FeO	20.24	20.39	20.25	19.87	20.34	20.18	22.03	22.54	22.56	22.28	22.22
MnO	0.24	0.07	0.00	0.05	0.01	0.04	0.08	0.07	0.05	0.04	0.12
MgO	9.29	9.36	9.32	9.36	9.29	9.27	8.22	7.89	7.61	8.08	7.96
Na2O	0.22	0.28	0.28	0.30	0.29	0.25	0.19	0.19	0.23	0.25	0.23
K2O	8.81	9.03	9.01	8.91	9.05	8.96	8.95	9.06	8.86	8.90	9.13
Total	94.45	95.54	95.01	95.17	95.03	95.02	94.74	95.69	94.34	95.13	95.15

Table A3.6 Biotite Compositions (Continued)

SAMPLE:	87-21A				87-104A						
	6	1	2	3	1	2	3	4	5	6	8
SiO2	34.13	34.99	34.72	34.69	35.23	34.82	34.97	34.79	35.18	35.04	34.83
AL2O3	19.35	17.98	19.09	17.92	18.55	18.66	18.80	18.87	18.53	18.93	18.62
TiO2	1.46	1.83	1.40	1.54	1.61	1.58	1.53	1.49	1.57	1.54	1.62
FeO	22.59	21.91	20.93	21.83	20.43	20.56	19.97	20.64	20.22	20.47	20.44
MnO	0.05	0.49	0.41	0.40	0.18	0.15	0.13	0.11	0.10	0.14	0.06
MgO	7.96	8.33	8.25	8.37	9.76	9.83	9.98	9.78	9.87	9.87	9.84
Na2O	0.22	0.06	0.04	0.05	0.14	0.11	0.13	0.15	0.12	0.12	0.16
K2O	9.18	9.67	9.19	9.68	9.68	9.39	9.46	9.37	9.49	9.46	9.48
Total	94.93	95.27	94.02	94.48	95.57	95.08	94.97	95.20	95.08	95.57	95.06

SAMPLE:	87-111						87-131C				
	9	1	2	3	4	6	1	2	3	4	5
SiO2	35.18	33.95	33.83	33.88	33.67	33.62	34.33	34.25	34.41	34.21	34.31
AL2O3	18.45	19.75	19.67	19.68	19.78	19.19	19.38	19.44	19.49	19.45	19.32
TiO2	1.55	1.67	1.90	1.71	1.63	1.51	2.13	2.15	2.05	2.14	2.19
FeO	20.36	24.30	23.48	23.71	24.65	25.61	21.10	21.07	21.51	20.85	21.25
MnO	0.10	0.02	0.01	0.03	0.00	0.03	0.12	0.16	0.14	0.12	0.18
MgO	9.89	5.63	5.39	5.44	5.58	5.28	8.27	8.08	8.19	8.03	7.99
Na2O	0.11	0.19	0.17	0.22	0.18	0.14	0.21	0.21	0.24	0.25	0.27
K2O	9.27	8.85	8.89	8.77	8.70	8.57	9.35	9.32	9.41	9.43	9.47
Total	94.89	94.35	93.35	93.44	94.19	93.96	94.88	94.68	95.45	94.48	94.96

SAMPLE:	87-131C				87-87						
	6	7	9	10	1	2	3	4	5	6	7
SiO2	34.33	34.44	34.90	34.66	34.79	35.18	34.49	37.27	35.37	35.42	34.90
AL2O3	19.43	18.49	19.82	19.50	18.86	18.93	18.83	22.33	19.05	18.86	18.82
TiO2	2.06	2.68	2.19	2.03	1.49	1.51	1.41	1.54	1.67	1.66	1.57
FeO	20.85	18.88	20.24	20.55	20.46	20.54	20.14	16.61	19.84	19.77	19.66
MnO	0.11	0.08	0.11	0.08	0.08	0.05	0.01	0.10	0.06	0.01	0.00
MgO	8.12	9.68	8.41	8.49	9.94	9.87	9.82	7.69	9.69	9.81	9.89
Na2O	0.26	0.27	0.24	0.27	0.24	0.26	0.27	0.45	0.24	0.24	0.23
K2O	9.39	9.28	9.34	9.24	9.04	8.92	8.95	8.94	8.91	9.13	9.13
Total	94.55	93.81	95.26	94.82	94.91	95.26	93.91	94.94	94.82	94.90	94.20

Table A3.6 Biotite Compositions (Continued)

SAMPLE:	88-N2								86-42		
	8	1	2	5	3	4	5	6	1	2	3
SiO2	35.35	35.82	35.45	35.50	34.56	35.32	35.70	35.01	36.25	36.22	35.75
AL2O3	19.00	19.39	19.57	19.46	19.05	19.45	19.43	19.14	17.91	17.80	17.35
TiO2	1.62	2.07	1.85	1.98	1.59	1.95	1.84	2.23	1.33	1.42	1.41
FeO	19.88	21.76	21.82	21.76	21.15	21.54	22.11	21.91	17.59	17.95	18.03
MnO	0.02	0.04	0.07	0.07	0.10	0.09	0.12	0.10	0.16	0.10	0.16
MgO	9.86	8.57	8.33	8.65	8.93	8.69	8.58	8.22	11.93	11.57	11.63
Na2O	0.27	0.30	0.30	0.26	0.27	0.25	0.28	0.21	0.18	0.20	0.17
K2O	9.07	8.87	8.71	8.95	8.76	9.00	8.80	9.10	9.87	9.81	9.41
Total	95.04	96.81	96.11	96.62	94.41	96.31	96.86	95.92	95.22	95.06	93.90

SAMPLE:	86-42						87-58				87-15D
	4	5	6	7	8	9	1	2	3	4	1
SiO2	36.13	36.29	36.07	35.73	36.33	35.74	35.50	34.90	36.05	36.18	35.72
AL2O3	17.75	17.78	17.72	17.72	17.87	17.41	18.53	17.88	18.79	18.92	19.41
TiO2	1.35	1.41	1.42	1.38	1.43	1.40	1.47	1.28	1.43	1.45	1.33
FeO	17.91	17.97	17.96	18.05	17.82	17.99	18.54	19.46	17.98	18.08	19.16
MnO	0.09	0.14	0.16	0.16	0.09	0.18	0.13	0.18	0.15	0.12	0.05
MgO	11.65	11.53	11.66	11.74	11.63	11.71	11.15	11.56	11.28	11.41	9.91
Na2O	0.19	0.19	0.20	0.21	0.21	0.18	0.13	0.08	0.19	0.15	0.41
K2O	9.63	9.80	9.67	9.61	9.76	9.64	9.64	8.80	9.55	9.87	8.98
Total	94.69	95.11	94.85	94.61	95.13	94.25	95.08	94.12	95.42	96.19	94.96

SAMPLE:	87-15D						87-73				
	2	3	4	5	6	1	1	2	3	4	1
SiO2	35.46	35.43	35.47	35.12	35.00	34.95	34.35	33.31	34.13	34.54	36.31
AL2O3	18.94	18.54	18.60	18.49	18.54	18.54	18.14	17.94	18.12	18.13	17.72
TiO2	1.29	1.33	1.35	1.49	1.50	1.44	1.56	1.36	1.51	1.47	1.59
FeO	19.75	19.92	19.76	19.47	20.05	19.93	23.82	24.52	23.49	23.19	19.29
MnO	0.00	0.09	0.01	0.07	0.04	0.02	0.04	0.00	0.05	0.00	0.21
MgO	10.46	10.41	10.09	10.22	10.38	10.05	7.53	7.91	7.27	7.53	9.93
Na2O	0.23	0.27	0.26	0.26	0.28	0.25	0.17	0.15	0.20	0.18	0.14
K2O	9.08	9.30	9.31	9.30	8.92	9.20	9.08	8.14	8.98	9.03	9.64
Total	95.21	95.30	94.85	94.41	94.71	94.37	94.68	93.33	93.74	94.07	94.84

Table A3.6 Biotite Compositions (Continued)

SAMPLE:	87-103							86-30			
	2	3	4	5	5	7	8	1	2	3	4
SiO2	36.35	36.65	36.54	36.42	36.55	35.40	38.22	33.99	34.90	33.93	34.60
AL2O3	17.51	18.40	18.24	18.05	18.25	19.19	18.90	20.02	20.64	19.62	19.55
TiO2	1.66	1.64	1.62	1.68	1.68	1.42	1.45	1.50	1.45	1.40	1.45
FeO	19.82	19.28	19.42	19.15	19.15	19.94	18.12	21.34	20.20	21.69	22.01
MnO	0.19	0.14	0.13	0.23	0.22	0.21	0.23	0.00	0.00	0.00	0.00
MgO	9.96	9.65	9.77	10.16	10.15	10.17	9.23	9.04	8.37	8.56	8.40
Na2O	0.10	0.09	0.08	0.07	0.07	0.06	0.54	0.32	0.40	0.27	0.29
K2O	9.76	9.49	9.45	9.58	9.71	8.20	9.02	8.87	8.47	9.07	8.87
Total	95.34	95.34	95.26	95.33	95.77	94.59	95.70	95.08	94.43	94.54	95.17

SAMPLE:	86-30		87-55B								
	5	6	1	2	3	4	5	6	7	10	12
SiO2	33.93	34.41	33.47	34.51	34.64	34.12	34.35	34.38	34.41	34.23	34.04
AL2O3	19.52	19.42	18.45	19.14	19.19	18.51	19.29	19.06	19.19	19.2	19.28
TiO2	1.37	1.37	1.91	2	2.11	1.94	1.79	2.01	1.93	1.58	2.04
FeO	21.65	21.55	22.23	21.11	20.62	22.25	20.96	21.72	21.73	21.18	21.42
MnO	0.00	0.00	0.08	0.05	0.12	0.09	0.03	0.07	0.08	0.11	0.04
MgO	8.44	8.37	8.25	8.09	8.02	8.03	8.3	8.18	8.22	8.52	8.4
Na2O	0.32	0.17	0.22	0.22	0.23	0.17	0.25	0.25	0.24	0.21	0.19
K2O	8.87	8.93	8.56	9.13	9.04	8.7	8.97	9.11	9.02	8.81	8.83
Total	94.10	94.22	93.17	94.24	93.97	93.81	93.94	94.78	94.82	93.83	94.24

SAMPLE:	87-121A							87-120			
	1	2	3	7	9	10	11	1	2	3	4
SiO2	35.01	34.46	33.91	34.59	34.75	34.69	34.52	34.27	34.47	34.74	34.82
AL2O3	18.91	18.19	18.59	18.46	18.98	18.92	18.84	18.87	19.2	19.14	19.26
TiO2	1.96	2.53	1.8	2.18	1.85	1.92	1.89	1.97	2	2.24	2.03
FeO	21.26	21.31	21.24	21.34	21.08	20.83	21.33	21.33	22.18	21.61	21.14
MnO	0.11	0.11	0.13	0.14	0.08	0.08	0.09	0.09	0.13	0.12	0.11
MgO	8.73	8.57	8.93	8.97	8.82	8.67	8.89	8.24	8.42	7.98	8.48
Na2O	0.24	0.29	0.31	0.28	0.32	0.28	0.26	0.22	0.24	0.23	0.3
K2O	9.01	8.85	8.89	8.97	8.98	8.87	8.85	8.58	8.42	8.77	8.99
Total	95.23	94.31	93.8	94.92	94.86	94.26	94.67	93.58	95.06	94.84	95.12

Table A3.6 Biotite Compositions (Continued)

SAMPLE:	87-120		87-1H								
	5	7	1	2	3	4	5	6	7	8	9
SiO2	34.69	34.3	36.7	36.27	36.07	36.5	36.52	36.77	36.35	36.61	35.8
AL2O3	18.79	18.91	18.64	18.73	18.87	18.53	18.83	18.36	18.45	18.82	18.35
TiO2	2.24	2.1	1.42	1.39	1.3	1.44	1.3	1.4	1.37	1.37	1.37
FeO	21.78	21.95	15.06	14.87	15.27	14.68	15.26	14.81	14.51	14.7	15.27
MnO	0.17	0.14	0.2	0.2	0.21	0.15	0.2	0.12	0.15	0.23	0.19
MgO	8.03	8.34	13.27	13.18	13.49	13.19	13.11	13.27	13.24	13.39	13.71
Na2O	0.24	0.23	0.42	0.4	0.32	0.32	0.35	0.31	0.28	0.4	0.33
K2O	9.02	8.72	9.25	9.14	8.72	9.4	9.14	9.21	9.5	9.04	8.75
Total	94.97	94.7	94.95	94.19	94.26	94.22	94.71	94.24	93.84	94.57	93.78

SAMPLE:	87-1H				87-116						
	10	11	12	13	1	2	3	5	6	7	8
SiO2	36.64	36.39	36.19	36.2	33.62	34.49	34.62	34.5	34.95	34.68	34.94
AL2O3	18.73	18.3	18.87	18.7	19.35	19.29	19.05	19.57	19.27	19.27	19.46
TiO2	1.44	1.46	1.57	1.4	1.96	2.06	1.93	2.05	2.21	2.21	2.14
FeO	14.72	15.17	15.06	14.95	22.68	20.52	21.56	21.23	20.79	20.79	21.21
MnO	0.25	0.24	0.15	0.18	0.02	0.05	0.08	0.09	0.1	0.1	0.08
MgO	14.72	12.89	13.07	13.18	8.09	8.18	8.21	8.38	8.04	8.04	8.37
Na2O	0.29	0.33	0.32	0.38	0.18	0.18	0.31	0.26	0.24	0.24	0.22
K2O	9.39	9.23	9.08	9.26	8.27	8.85	9.02	8.96	9.07	9.07	9.17
Total	96.19	94.03	94.32	94.25	94.17	93.63	94.78	95.05	94.67	94.4	95.59

SAMPLE:		87-116A							87-112A	
	9	1	2	3	4	5	6	7	8	1	2
SiO2	34.34	34.62	35.22	34.91	34.4	35.1	34.7	34.77	34.81	35.2	34.99
AL2O3	19.32	19.32	19.27	19.31	18.5	18.96	19.13	19.28	19.13	19.39	19.64
TiO2	2.17	1.76	1.83	1.97	1.92	2.14	1.71	2.17	2	1.79	1.54
FeO	20.58	20.26	20.67	20.71	20.36	21.01	20.76	20.3	20.5	21	21.02
MnO	0.09	0.08	0.08	0.08	0.14	0.08	0.05	0.06	0.04	0.09	0.03
MgO	8.35	8.83	8.84	8.51	8.78	8.63	8.77	8.77	8.82	8.6	8.64
Na2O	0.27	0.26	0.27	0.31	0.26	0.26	0.32	0.27	0.23	0.27	0.24
K2O	8.88	9.19	9.15	8.94	8.87	9.07	9.17	9.04	9.07	8.97	8.75
Total	94	94.32	95.33	94.75	93.23	95.25	94.6	94.67	94.6	95.31	94.86

Table A3.6 Biotite Compositions (Continued)

SAMPLE:	87-112A					
	3	4	5	6	7	8
SiO2	35.24	34.65	35.02	34.62	34.97	34.81
AL2O3	19.52	19.27	19.32	18.9	19.04	18.87
TiO2	1.49	1.6	1.54	1.43	1.45	1.58
FeO	21.23	21.58	21.16	21.53	21.96	21.66
MnO	0.08	0.07	0.05	0.06	0.04	0
MgO	8.83	8.7	8.66	8.82	8.92	8.87
Na2O	0.28	0.26	0.23	0.26	0.24	0.26
K2O	8.85	8.82	8.87	8.78	8.88	8.89
Total	95.51	94.94	94.85	94.4	95.49	94.94

VITA

Thomas Seaman Helms was born December 7, 1959 in Winston-Salem, North Carolina, the son of Crampton Harris Helms and Ruth Seaman Helms. He received a Bachelor of Science degree from Emory University with a major in geology in 1982 and the Master's of Science degree, with a major in geology from the University of Tennessee, Knoxville in 1985. Thomas is currently unemployed in the post-Reagan nineties.